MODELING AND EXPERIMENTAL MEASUREMENTS OF THERMODYNAMIC PROPERTIES OF NATURAL GAS MIXTURES AND THEIR COMPONENTS

A Dissertation

by

MARTIN ALONSO GOMEZ OSORIO

Submitted to the Office of Graduate and Professional Studies of
Texas A&M University
in partial fulfillment of the requirements for the degree of

DOCTOR OF PHILOSOPHY

Chair of Committee,	James Holste
Co-Chair of Committee,	Kenneth Hall
Committee Members,	Perla Balbuena
	Maria Barrufet
Head of Department,	Nazmul Karim

August 2016

Major Subject: Chemical Engineering

ABSTRACT

Chemical process design requires mathematical models for predicting thermophysical properties. Those models, called equations of state (EoS), need experimental data for parameter estimation and validation. This work presents a detailed description of a vibrating tube densimeter, which is an alternative technique for measurement of p-ρ-T data in gases at critical conditions. This apparatus can measure fluids in a temperature range of 300 K to 470 K and pressures up to 140 MPa. This work calibrates the vibrating tube using a physical-based methodology with nitrogen, methane and argon measurements. Carbon dioxide and ethane p-ρ-T data validate calibration procedures covering a wide range in density and pressure. The vibrating tube densimeter performs density measurements for nitrogen + methane mixtures for pressures up to 140 MPa.

This work also presents a new equation of state (EoS) having a rational form that can describe properties with accuracy comparable to the best multi-parametric equations with less mathematical complexity. This EoS presents the Helmholtz residual energy as a ratio of two polynomial functions in density (no exponential terms in density are included), which can describe the behavior of pure components. The EoS can be transformed to describe other thermophysical properties as pressure, compressibility factor, heat capacity and speed of sound. Also this equation can calculate saturated liquid-vapor properties with 20 times less computational time. This work presents

rational EoS for nitrogen, argon and methane applicable in wide ranges of pressure and temperature.

Finally this work proposes a new mixing rule for binary mixtures of gases based upon a quadratic combination of residual Helmholtz energy. This approach divides the energy contribution between interactions of same species and interaction of different species molecules. A rational form is proposed for description of energy interaction between molecules of different species. The mixing rule is applied to nitrogen + methane data.

DEDICATION

To my family

“There is nothing impossible to him who will try”

Alexander the Great

ACKNOWLEDGEMENTS

I would like to thank my graduate advisors, Dr. James Holste and Dr. Kenneth Hall for their guidance throughout the course of this research and the wonderful opportunity to be part of this group and research area. Thanks to Dr. Diego Cristancho from Dow Chemical for his advice and collaboration during this research process. Also I thank my committee members, Dr. Perla Balbuena and Dr. Maria Barrufet, for their advice and comments.

I want to extend my gratitude to Dr. Mark McLinden and Stephanie Outcalt from NIST for their recommendations in the development of experimental methodologies and techniques. Also I want to thank Dr. Eric Lemmon and Dr. Ian Bell from NIST for their support and collaboration on the development of a new equation of state. Thanks to Randy Marek and Jason Caswell for their collaboration in this project.

Thanks also go to my teammates and colleagues Robert Browne, Diego Ortiz, Hugo Acosta, Andrea Tibaduiza and Ivan Mantilla for all the lessons, experiences and guidance during my time in graduate school. Also thanks to Mauricio Carvajal, Catherine Sampson, Pilar Suarez, William Prieto, Monica Longoria and Shashank Kamdar for their support and contribution in this work. Thanks to the Chemical Engineering Department faculty, students and staff for making my time at Texas A&M University a great experience.

Finally, thanks to my family for their love and to Tatiana Flechas for her patience and support.

TABLE OF CONTENTS

Page

LIST OF FIGURES

Page

LIST OF TABLES

Page

1. INTRODUCTION

Natural gas is one of the most important energy sources in the world. It is a fossil fuel formed deep below the surface of the earth, but production and consumption have increased rapidly because of global demand. Natural gas is an attractive alternative to coal and oil because it burns cleaner.

Total energy demand in the United States in 2013 was 5.6 quadrillion BTU with natural gas composing 27 %. Production in the United States increased by 35 % from 2005 to 2013. In total, the USA produces approximately 25 trillion cubic feet of dry natural gas each year [1]. It is necessary to know natural gas physical properties to produce and process it, and small errors in properties could result in losses of millions of dollars per year.

Process design and modeling require correlations for thermodynamic properties for fluids. The correlations, notably equations of state (EoS), depend upon measurements of physical properties. Development of EoS requires accurate p-ρ-T data.

1.1 Experimental methods for density measurements

Many methods exist to measure fluid densities. One of the most important is the buoyancy or hydrostatic method based upon the Archimedes principle [2]. It states that the difference between the true and the apparent weight of a body immersed in a fluid is related to volume displaced and density by

$$\rho = \frac{m_T - m_A}{V_S} \qquad [1]$$

In equation 1, m_T is the true weight, m_A is the apparent weight, V_S is the volume of the body and ρ is density of the fluid.

Different types of apparatus exist for density measurements based upon Archimedes principle; some are: hydrostatic densimeter balances, magnetic float and magnetic suspension densimeters. In a hydrostatic balance densimeter, a cylinder of metal or glass is suspended in a fluid by a thin platinum wire. The wire is attached to an analytical balance, which records the weight of the total system. Then, the cylinder is immersed in the liquid whose density is desired. Using the apparent weight and the Archimedes principle, the density of the fluid results from equation 1. This method provides liquid densities at ambient pressure over moderate temperature ranges [2].

Natural gas process and production properties may involve extreme pressure and temperature values. For deep water gas production pressures can reach 200 MPa (~30,000 psi) and temperatures can exceed 150 $^{\circ}$C [3]. A magnetic suspension densimeter can operate at these conditions with good accuracy.

1.1.1 Magnetic suspension densimeter

The magnetic suspension densimeter (MSD) uses the Archimedes principle but introduces a magnetic suspension coupling mechanism. This arrangement physically separates the balance from the sample fluid. The MSD lends itself to highly accurate measurements of fluids at extreme conditions. The components of the magnetic suspension coupling are: an electromagnet, a permanent magnet, a sinker, a position senor and a control system [2].

The electromagnet hangs from an analytical balance, which is at ambient pressure. The permanent magnet resides in a high-pressure coupling housing situated under the electromagnet that creates a physical barrier between the two magnets. The permanent magnet contacts the measured fluid at the experimental pressure and temperature. A small current through the electromagnet generates a magnetic field that couples with the permanent magnet.

A sinker attached to the permanent magnet is a reference volume for the density calculation. A position sensor and control systems fix the position of the permanent magnet and sinker. Figure 1 presents a representation of a single–sinker magnetic suspension densimeter showing the permanent magnet, the electromagnet, the balance and the sensor position.

To avoid errors caused by non-linearity of balance measurements, the device contains two compensation weights (tare and calibration). Those weights are located on mechanical arms, which can place them on or remove them from the balance. Accurate density measurements using a magnetic suspension densimeter include at least 2 mass readings with different configurations. Figure 2 shows the positions required in a single-sinker operation: off position, zero point (ZP) and measurement point (MP).

At the Off position the permanent magnet (PM) is not coupled to the electromagnet and the compensation weights do not contact the balance. For ZP measurements, the suspension coupling is activated creating interactions between the two magnets but the PM does not lift the sinker at this position. Also, one of the compensation weights (calibration mass) is placed on the balance. ZP measurement

includes PM mass (p-mag), PM buoyancy effect (ρV), EM mass, calibration mass (CM) and their buoyancy effects. Equation 2 includes all components for a ZP mass measurement. Because the PM contacts the measured fluid, the buoyancy effect uses density of the fluid.

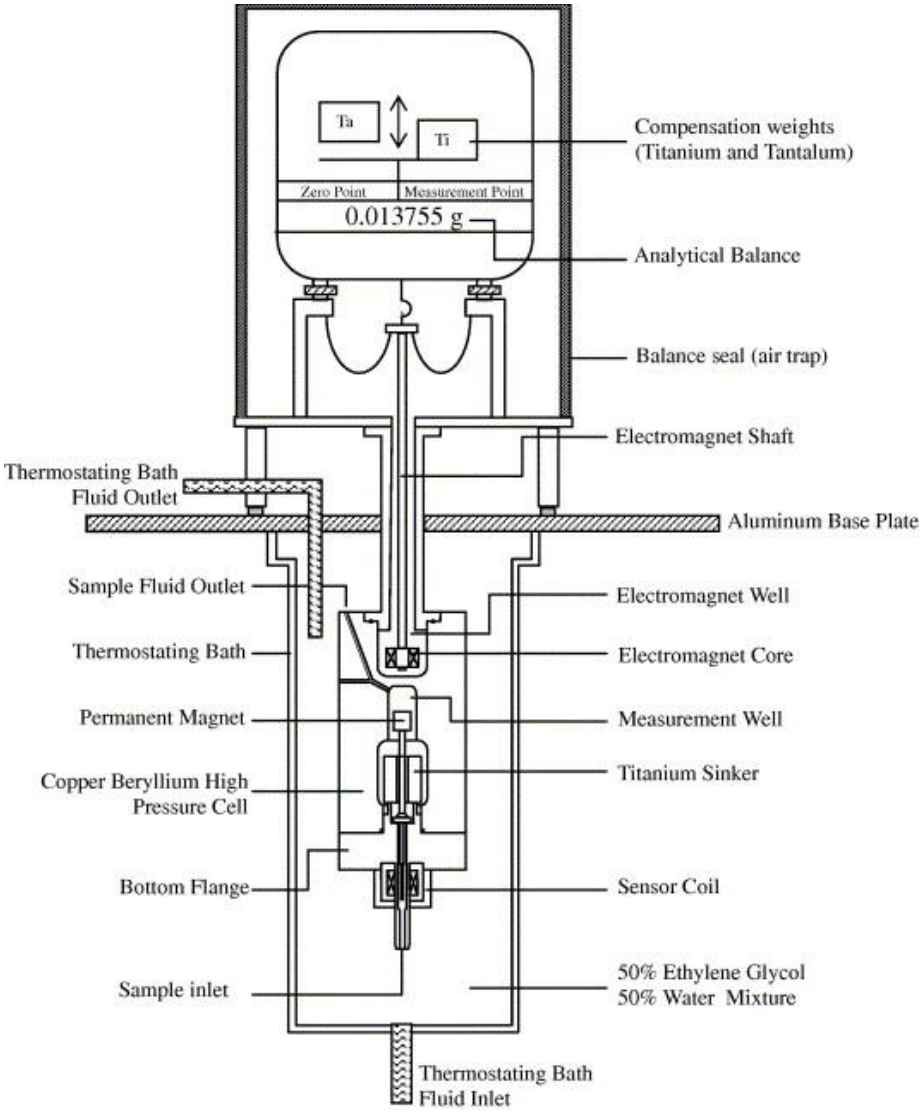

Figure 1. Magnetic suspension assembly of a single – sinker densimeter.
Acknowledgment: [4], [5].

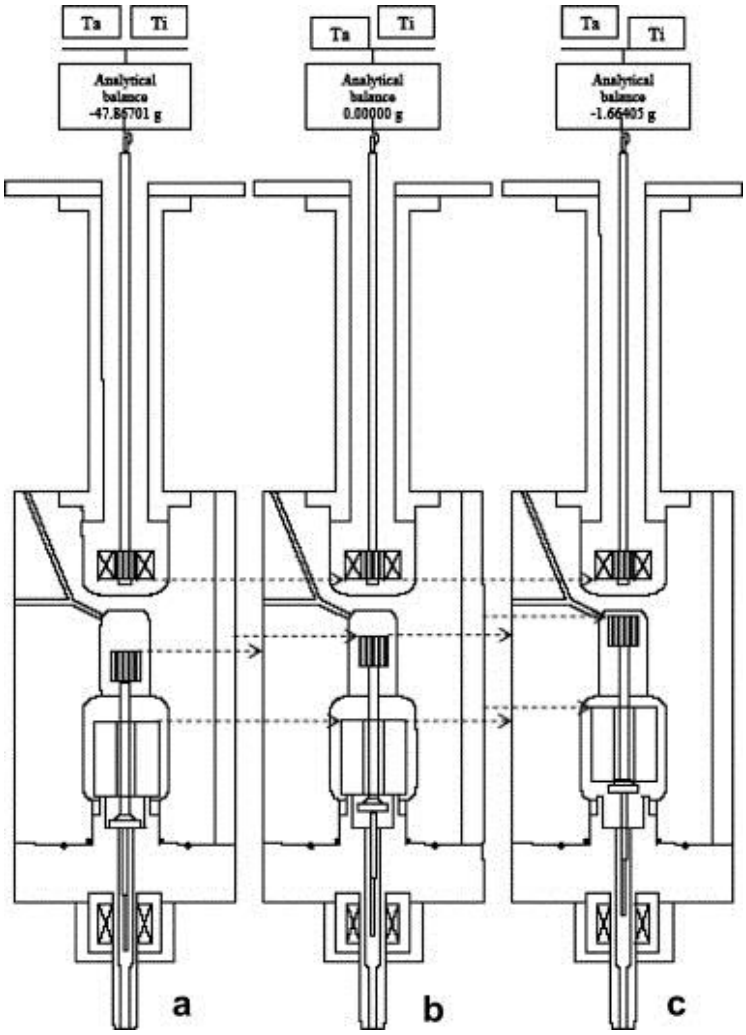

Figure 2. Operation of the MSD using weight changing device (a) suspension control off, Ti and Ta both raised (b) zero point (ZP) position, Ta lowered, Ti raised (c) measurement point (MP) position, Ta raised, Ti lowered. *Acknowledgment:* [4], [5].

At the MP, the PM lifts the sinker and the calibration mass is replaced with the tare mass on the balance. The MP contains some of the ZP factors, but it adds the mass of the sinker (m_s), buoyancy of the sinker, tare mass and its buoyancy. Equation 3 shows factors in a mass MP measurement. Equations 2 and 3 include the balance calibration factor (α) and a coupling factor (φ) known as the force transmission error [6].

$$M_{ZP} = \alpha\left[\phi\left\{m_{p-mag} - \rho_{fluid}V_{p-mag}\right\} + m_{e-mag} + m_{cal} - \rho_{air}\left(V_{e-mag} + V_{cal}\right)\right] \quad [2]$$

$$M_{MP} = \alpha\left[\phi\left\{m_s + m_{p-mag} - \rho_{fluid}\left(V_s + V_{p-mag}\right)\right\} + m_{e-mag} + m_{tar} - \rho_{air}\left(V_{e-mag} + V_{tare}\right)\right] \quad [3]$$

Calibration fluids are not necessary in this technique, but sinker mass and volume are essential. An independent procedure must provide accurate values for sinker dimensions. This technique is not appropriate for fluids that can react with the sinker. Normally, the compensation weights have similar volumes, thus minimizing air buoyancy effects. In addition, this technique requires accurate values the for calibration and tare masses.

Subtracting equation 2 from equation 3 and solving for the fluid density gives equation 4, which is an expression for density as function of ZP, MP measurements and reference masses

$$\rho_{fluid} = \frac{\phi m_s + \left(m_{tare} - m_{cal}\right) - \left(M_{MP} - M_{ZP}\right)/\alpha - \rho_{air}(V_{tare} - V_{cal})}{\phi V_s} \quad [4]$$

The only unknowns in equation 4 are the balance calibration factor (α) and the force transmission error (φ). McLinden [6] estimates the calibration factor (α) to be approximately 0.0015 for this configuration.

Patil et al. [4] used a single-sinker MSD to measure a simulated natural gas mixture containing nine components including 91 % methane. The measurements ranged from 270 K to 340 K at pressures up 35 MPa. The authors claimed an uncertainty of ±0.12 % with 95 % confidence level.

Later, Atilhan et al. [7] performed measurements for three synthetic gas mixtures up to 150 MPa. They used tantalum (Ta) and titanium (Ti) compensation weights and a Ti sinker. These authors kept balance reading values close to zero using a calibration mass value (Ta) equal to the tare mass (Ti) plus the sinker mass (combined). The mixtures had up to 9 nine components with concentrations of methane close to 90 %.

The core of this technique is the measurement of the apparent mass of a sinker using an accurate balance. Factors such as the magnetic behavior of the cell, the suspension coupling and measured fluid can affect the balance readings. This effect is the force transmission error (FTE) [8]. The factor (φ) corrects FTE, but it depends upon apparatus configuration. The apparatus used by Atilhan et al. [7] had a titanium sinker inside a beryllium-copper cell that operated up to 200 MPa (29,000 psia) within a temperature range from 190 K to 520 K. Cristancho et al. [8] estimated the FTE for this MSD over the entire range of pressures. They found that temperature is the main factor in the FTE analysis, and that pressure values do not have appreciable effects for natural gas components. They proposed a methodology for estimating FTE values for each temperature using MSD measurements at vacuum conditions. Equation 5 shows the simplified method to calculate the FTE.

$$\phi = \frac{\left(\left(m_{tare} - m_{cal}\right) - \left(M_{MP} - M_{ZP}\right)/\alpha - \rho_{air}\left(V_{tare} - V_{cal}\right)\right)}{m_s} \qquad [5]$$

This FTE is part of a complete uncertainty analysis presented by Ortiz-Vega et al. [9]. This analysis included pressure, temperature and composition effects. The FTE is

the main contribution in total uncertainty for an MSD. Corrections for the apparatus effect are around 186 ppm for pressures up to 200 MPa.

Kleinrahm and Wagner [10] designed a two–sinker magnetic suspension densimeter. The two-sinker version includes a second sinker measurement as a reference. This additional value allows calculation of FTE directly for every pressure point. McLinden et al. [6] proposed an empirical methodology to estimate values of FTE for two-sinker densimeters. They found an FTE of approximately 16 ppm. Additionally, they found that the density of the fluid can affect the values of FTE when the fluid has magnetic susceptibility. Some of main factors in FTE corrections are the pressure cell dimensions, materials of construction and maximum allowable working pressure (MAWP). The McLinden densimeter has a lower FTE, but its MAWP is 40 MPa.

The MSD technique also can perform measurements in saturated vapor-liquid systems, and it has good accuracy for extreme conditions in temperature and density. However, the sample fluid needs a residence time of 4 to 8 hours per pressure reading for a complete characterization, which becomes an issue for samples that decompose with time.

Some fluids have particular characteristics that make them difficult to measure, such as hydrogen sulfide (very toxic, reactive and corrosive), which is present in natural gas. Corrosive fluids can attack the MSD materials and affect their properties. As equation 4 shows, the sinker mass and volume must be known accurately. Changes in those values affect measurement results and increase errors.

1.1.2 Isochoric apparatus

Other authors have used isochoric techniques for density measurements. Classically, they determine the volume and mass of a sample cell under vacuum. Then, they place a sample in the cell and weigh it again to establish the mass and density of the fluid in the cell at the loading conditions. An experimental run commences after changing the temperature of the cell to a predetermined value. When the system reaches equilibrium, temperature and pressure are measured and recorded. Temperature variation results in a new pressure. A run consists of changing the temperature over a selected range and recording the pressures at each temperature. This technique produces p-ρ-T data sets along pseudo-isochores (constant density), because the mass remains constant during the experiments and measure hazardous fluids. However, it is a time consuming technique, because the system equilibration times are long. Also, the density calculations require complex corrections, because truly isochoric experiments require a constant cell volume. Thermal expansion and mechanical deformation of the cell dimensions change the volume during the experiment. Using the volume of the cell at a reference temperature and pressure, the volume of the cell at each experimental condition results from a calculation using the volumetric thermal expansion and mechanical deformation properties of the material of construction.

The mass inside the cell remains constant during the experiment, but the mass measurement occurs after filling the cell. This requires removing the cell from the apparatus to measure the mass. Holste et al. [11] suggested using experimental density measurements from another apparatus, such as a Burnett apparatus or a pycnometer for

estimating isochoric densities. The Burnett apparatus or pycnometer provides isothermal densities that intersect the pseudo-isochores, thus supplying accurate densities at selected points along the pseudo-isochores. Zhou et al. [12] performed isochoric measurements for natural gas-like samples using densities obtained using a magnetic suspension densimeter (MSD).

A MSD provides accurate density measurements, but in combination with isochoric experiments more information becomes available from p-ρ-T data. Atilhan et al. [13] used isochoric data for experimental determination of phase equilibrium for synthetic natural gas samples. They used a method developed by Acosta-Perez [14] for measuring experimental phase boundaries and determining uncertainties. This method uses the change in slope of an isochore when it crosses into the two-phase region.

Isochoric data also provides important information about other thermodynamic properties. For example, residual entropy is a function of the derivative of pressure with temperature at constant density $(\partial p/\partial T)_\rho$. Tibaduiza et al. [15] use pressure and temperature values at constant density for experimental estimation of energies and entropies in a ternary mixture.

1.1.3 Vibrating tube densimeter

A vibrating tube densimeter (VTD) is a hollow metallic or glass tube bent in a "U" or "V" shape that is attached to a large mass. The resonant frequency of vibration of the tube varies with the mass of the tube and any fluid contained therein. The dimensions of the tube can vary with the pressure range of the system. Usually, the length of the tube

is 5 to 10 cm with an outer diameter of about 1.5 mm. For high-pressure VTDs, the diameter can be 3 mm [2]. The sample of interest enters the tube, which vibrates perpendicular to its plane.

An accurate measurement with a VTD relies upon determination of the resonant frequency. To obtain the resonance values, the system controls a magnetic field and quantifies the tube oscillation. In commercially available instruments, two methods exist for driving and measuring the tube frequency. Figure 3 illustrates one of the commercial methods available. In this configuration, two permanent magnets are mounted on the free end of the tube. A current source, connected to a driving coil, is located perpendicular to one of the magnets. It induces a variable magnetic field producing vibration of the tube. Oscillation of a second magnet induces a current on a perpendicular pick-up coil. A frequency counter, attached to the pick-up coil, analyzes and measures the signal. A feedback loop optimizes frequency to obtain values at resonance [16]. This work uses a measurement cell provided by Anton-Paar that uses the configuration shown in figure 3.

The second commercial method involves two wires attached across the tube, with a permanent magnet focused on the wires [17]. For this method, a low level current is supplied to one wire (pick–up wire) creating a perpendicular motion of the wire. Later this current is amplified and sent to the second wire (drive). The tube is driven into vibration by alternating current in the magnet field. Using a control loop, the system obtains the resonance frequency.

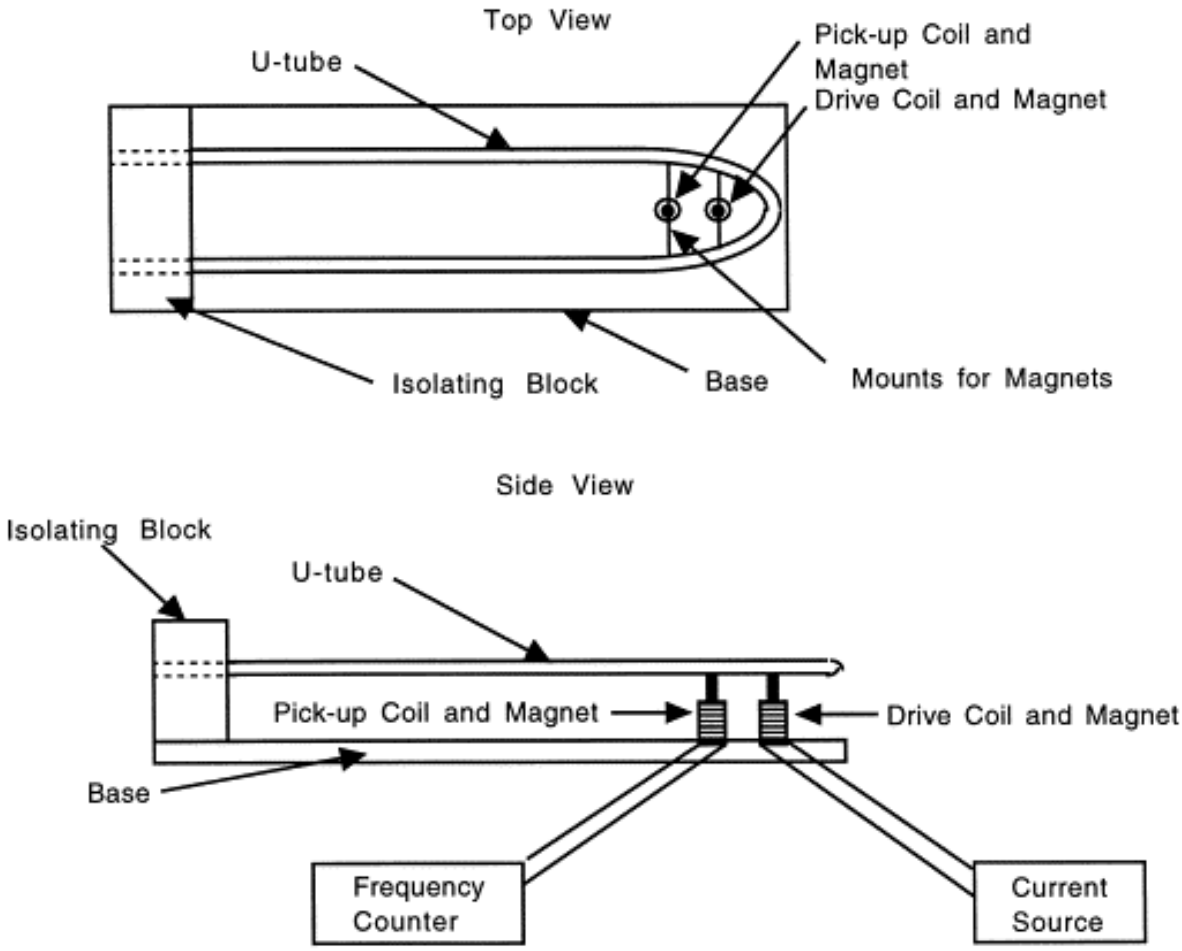

Figure 3. Diagram of the vibrating tube densimeter using drive coil and pick-up coil. *Acknowledgment:* [16]

1.1.3.1 Principal of operation

The motion of a mass coupled to a spring provides an appropriate model for a vibrating tube. A U-shape tube, attached to a magnet, oscillates at the mechanical resonant frequency that is related to the mass of the system (tube + fluid in tube). A simple harmonic oscillator describes the VTD oscillation using some assumptions.

Simple harmonic oscillator

A vibrating tube can be assumed to be a simple harmonic oscillator composed of a spring and mass system with a driving force and viscous damping. Figure 4 is a representation of the vibrating tube densimeter as a spring and mass system.

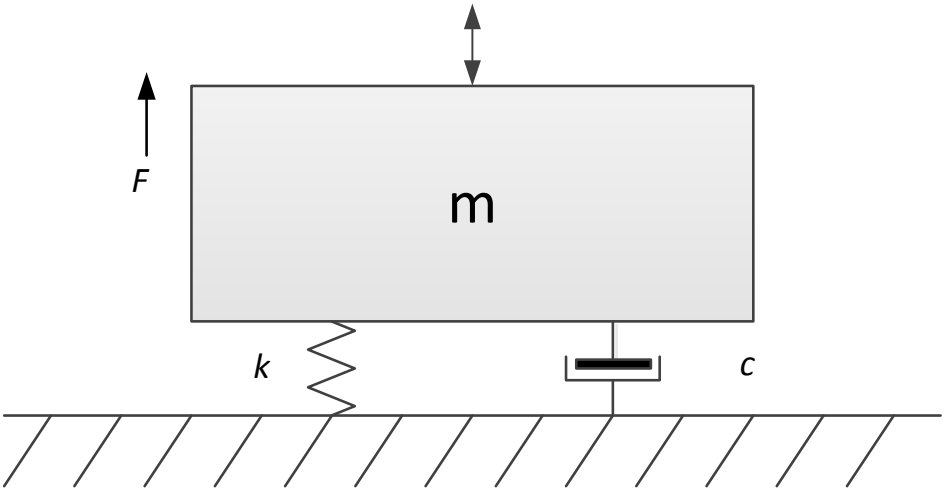

Figure 4. Oscillation of a spring and mass system

Assuming a single viscous damper and Hooke's law for spring forces, the force balance for the system is:

$$\sum f = ma = F_{Hooke} + F_{damper} = -kx - cv \qquad [6]$$

In this case, m is mass, k represents spring constant, x is tube displacement from reference position, c is the damping constant, v is velocity and a is acceleration.

Velocity and acceleration are the first and second derivatives of displacement with respect to time, respectively. The equation of motion for a spring-mass system as a function of displacement, mass, damping and spring constant is:

$$m\frac{d^2x}{dt^2}+c\frac{dx}{dt}+kx=0 \qquad [7]$$

The assumptions used for modeling the vibrating tube as a spring-mass system are:

- Mass of the vibrating tube base is infinite
- The vibrating tube distorts elastically
- The elastic constant is independent of the fluid in the tube
- System damping is a single, lumped viscous damper

Using a solution for homogenous second order differential equations, McGregor [17] shows that the resonance frequency is a function of mass, spring constant and damping constant.

$$\omega_r^2=\frac{k}{m}-\frac{1}{2}\left(\frac{c}{m}\right)^2 \qquad [8]$$

Simplification of the relationship between fluid density and the resonance frequency requires an undamped system. In this case *c* equals zero, and the resonance frequency is a function of mass and spring constant. Because the mass of the system is the combined mass of the tube and the fluid inside the tube, the relationship between mass of the fluid (m_f), the mass of the tube (m_T), and the undamped resonant frequency is:

$$m_T+m_f=\frac{k}{\omega_u^2} \qquad [9]$$

This equation provides the basis for calibrating vibrating tube densimeters. The resonant phenomenon occurs when the system oscillates at the maximum amplitude caused by the interaction of an external force or vibrating system. This occurs at a

specific value of frequency called the undamped resonance frequency or the natural frequency. Currently, commercial vibrating tube densimeters contain automatic control systems that maintain the frequency at resonance.

1.1.3.2 Classical calibration methods

The classic calibration method requires two fluids (a calibration fluid and a reference fluid) for solving an equation with two unknowns. In following equations, subscripts *o* and *c* denotes the reference and calibration fluids respectively. Measuring two different fluids at the same conditions of temperature and pressure and subtracting equation 9 provides:

$$m_{fc} - m_{fo} = k\left(\frac{1}{w_{uc}^2} - \frac{1}{w_{uo}^2}\right) \qquad [10]$$

The mass of the tube cancels because it is independent of the fluid, but the volume of the tube is necessary to calculate the mass of the fluid from its density. The volume of the tube (v_t), is the same for the reference and calibration fluids because the temperature and pressure conditions are similar, so that Equation 10 becomes:

$$\rho_f - \rho_{fo} = K\left(\tau_u^2 - \tau_{uo}^2\right) \qquad [11]$$

where ρ_f is the density of the calibration fluid, ρ_{fo} is the density of the reference fluid, τ is the period of oscillation($t = 2\pi / w$) and K ($= k / 4\pi^2 v_t$) is a modified spring constant.

This simple model relates linearly the square of the resonant period and the density of the fluid. However, temperature and pressure affect the spring constant and the internal volume of the tube. Thus, the model must estimate temperature and internal pressure effects *via* calibration measurements at different conditions. Measuring the resonant period of oscillation for reference fluids with well-known values of density, allows calculation of the modified spring constant at specific temperatures and pressures using:

$$K(T_o, P_o) = \frac{\rho_f - \rho_{fo}}{\tau_u^2 - \tau_{uo}^2} \qquad [12]$$

Rearranging equation 11 using alternate variables provides the working form

$$\rho(\tau) = A(T_o, p_o)\left(\tau^2 - \tau_{uo}^2\right) - B(T_o, p_o) \qquad [13]$$

where the parameters $A(T_o,p_o)$ and $B(T_o,p_o)$ come from the calibration measurements.

Galicia-Luna et al. [18] used nitrogen and water as reference fluids to measure binary and ternary mixtures of carbon dioxide, methanol and propane. They covered pressures up to 39 MPa and claimed an uncertainty of ±0.18%.

Accurate measurements over wide ranges of pressure and temperature exist for only a few pure fluids. Inaccuracies in reference values are sources of errors with the vibrating tube technique. Also, calibration fluids must be stable, not hazardous, and with density values close to the desired samples. In 1992, Sousa et al. [19] used resonant

period at vacuum conditions as reference, reducing errors caused by calibration fluids. Using Sousa's approach, equation 14 eliminates one of the parameters in equation 13.

$$\rho(\tau) = \left(\frac{\rho_f - \rho_{fo}}{\tau_u^2 - \tau_{uo}^2} \right) \left(\tau^2 - \tau_{uo}^2 \right) = A(T_o, p_o) \left(\tau^2 - \tau_{uo}^2 \right) \quad [14]$$

Sousa et al. [19] collected density measurements for liquid and vapor phases for R-142b and R-22 + R -142 b binary mixture.

1.1.3.3 Previous work

In 1969 Kratky et al. [20] used a VTD to measure gas and liquid densities with a sample of only 6 cm^3. This VTD had a configuration with magnets attached to the tube, which is the base for the modern commercial model produced by Anton Paar. In 1974, Picker et al. [21] used a VTD as a flow densimeter for liquids. In 1989, McGregor [17] designed a semi-automated vibrating tube densimeter for operation between 100 K and 700 K at pressures up to 70 MPa. His design used a design based on two wires attached across the tube to achieve high temperature operation. McGregor performed density measurements for toluene, ethylbenzene and 2,2,4 - trimethylpentane using a classical calibration equation as in equation 11.

Early VTD calibrations used classical methods, but given additional understanding of the system empirical, semi-empirical and physically-based equations have resulted for calibration. Many of the modern calibration models use the work of Holcomb and Outcalt [16]. They assumed the vibrating tube to be a vibrating rod with

both ends clamped. Assuming negligible damping effects, Newton's equation of motion for a vibrating rod is:

$$E(T)I(T,p)\frac{\partial^4 Y(Z,t)}{\partial Z^4}+\rho_R(T,p)A(T,p)\frac{\partial^2 Y(Z,t)}{\partial Z^2}=0 \qquad [15]$$

where *A* is cross-sectional area, *E* is Young's modulus, *I* is the second moment of inertia, r_R is the rod density, *Y* is the vertical displacement at position *Z* and time *t*.

To establish boundary conditions for equation 15, Holcomb and Outcalt took vertical displacements equal to zero at both ends of the rod, because the ends are clamped. They found a generalized solution applying separation of variables. The first nonzero solution constant for the vibrating system is:

$$\beta_1=\left(\omega_n(T,p)\left(\frac{\rho_R(T,p)A(T,p)}{E(T)I(T,p)}\right)^{\frac{1}{2}}\right)^{\frac{1}{2}} \qquad [16]$$

This equation is a function of the same parameters as equation 15, but it adds a new variable, the resonant frequency ($\omega_n(T,p)$).

Equation 17 presents an expression for density of the fluid as function of physical parameters (Young's modulus and moment of inertia), a constant (β_1) and tube dimensions (mass, volume and length).

$$\rho_F(T,P)=\frac{\beta_1^4 E(T)I(T,p)}{L^3(T,p)\omega_n^2(T,p)V_i(T,p)}-\frac{m_T}{V_i(T,p)} \qquad [17]$$

To simplify calculation and find a solution for constant β_1, it is convenient to evaluate equation 17 at vacuum at a reference temperature. The resonant frequency at vacuum is:

$$\omega_n^2(T_o,0) = \frac{\beta_1^4 E(T_o) I(T_o,0)}{L^3(T_o) m_T} \quad [18]$$

Combining equations 17 and 18 yields a relationship for density of the fluid.

$$\rho_F(T,P) = \frac{m_T}{V_i(T,p)}\left(\frac{L^3(T_o,0)E(T)I(T,p)\omega_n^2(T_o,0)}{L^3(T,p)E(T_o)I(T_o,0)\omega_n^2(T,p)} - 1\right) \quad [19]$$

Semi-empirical and empirical calibration

Equation 19 is a physical representation for VTDs that is a starting point for many calibration models. Various authors have used different assumptions for describing physical parameters, such as moment of inertia, Young's modulus and tube volume. Holcomb and Outcalt [16] worked in a moderate temperature (290 K to 395 K) and pressure range (up to 14 MPa). Their final calibration model is a semi-empirical approach based upon equation 19, using a first order approximation for thermal expansion and deformation effects that leads to a simplified calibration model

$$\rho_F(T,p) \simeq \left(\frac{\omega_n^2(T_o,0)\left(A_1 + A_2 T + A_3 T^2\right)}{\omega_n^2(T,p)}\right) + A_4 + A_5 p + A_6 T \quad [20]$$

They performed calibration measurements with nitrogen, water, ethane, propane, *n*-Butane and HFC-152a, finding an average uncertainty of ±0.3 kg·m^{-3} for liquid densities and ±1.0 kg·m^{-3} for vapor densities.

In 2007, Outcalt and McLinden [22] proposed an empirical approach for calibration measurements that is similar to the Holcomb model, but which includes second-order pressure-temperature interactions and third-order for temperature contributions

$$\rho_F(T,p) = \left(A_1 + A_2 T + A_3 T^2 + A_4 T^3 + A_5 p + A_6 p^2 + A_7 T p\right)\frac{\tau^2(T,p)}{\tau_o^2(T,0)} - \left(B_1 + B_2 T^2 + B_3 T^3 + B_4 p + B_5 p^2 + B_6 T p\right) \quad [21]$$

Their model (equation 21) has 13 constants divided in two groups: interactive with (*A*) or independent (*B*) of tube vibration. Also, their model uses the resonant period of oscillation $\left(\tau = 2\pi/\omega\right)$ instead of resonant frequency.

Outcalt and McLinden use an empirical quadratic function in temperature to describe the resonance period of oscillation at vacuum (τ_o)

$$\tau_o = c_o + c_1 T + c_2 T^2 \quad [22]$$

where the parameters in equation 22 come from resonance measurements at vacuum for various temperatures.

Outcalt and Mclinden performed calibration measurements with propane and toluene over a range of 270 K to 470 K at pressures up to 50 MPa. Also, they presented a detailed uncertainty analysis, including effects from equation of state errors, resonant period of oscillation at vacuum, and pressure and temperature sensors. Their analysis showed that major error contributions stem from the equations of state for the calibration fluids and the repeatability of vacuum measurements. The overall uncertainty for this

methodology was ±(0.64 – 0.81) kg·m^{-3}. Errors due to repeatability of vacuum measurements are equivalent to ±0.6 kg·m^{-3}. This VTD can characterize industrial fluids rapidly and make measurements with this accuracy over wide pressure ranges.

Forced path mechanical calibration (FPMC)

In 2001, Bouchot and Richon [23] developed a calibration methodology based entirely upon physical properties behavior, thereby reducing calibration fluid dependences. They used equation 19 as the starting point of the model, but replaced the internal volume of the tube with the internal transversal area and length. The variation of length with temperature and pressure is:

$$L(T,p) = L(T_o,0)\left(1+\alpha(T)(T-T_o)+\gamma_T p\right) = L_{00}\delta L \qquad [23]$$

where $\alpha\ (T)$ is the linear expansion coefficient and γ_T is the linear pressure distortion coefficient. The variation of the internal and external radii with temperature at zero pressure then is:

$$r_{ko} = r_{koo}(T_o,0)\left(1+\alpha(T)(T-T_o)\right) \qquad [24]$$

where, r_{koo} represents radius values at reference conditions, r_{ko} radius at a selected temperature, and k is internal (i) or external (e) radius.

The Lamé equations, which contain the Poisson coefficient and Young's modulus, correct the radii values for pressure effects. Because the vibrating tube is a

hollow cylinder, the external and internal radii depend upon each other. The relationship for a given radii (internal or external) is:

$$r_k(T,p)=\frac{r_{ko}+\sqrt{r_{ko}^2+4\left\{1-\left(\frac{1-\nu}{E}\right)\left(\frac{r_{io}^2 p}{r_{eo}^2-r_{io}^2}\right)\right\}\left(\frac{1+\nu}{E}\right)\left(\frac{r_{eo}^2 r_{io}^2 p}{r_{eo}^2-r_{io}^2}\right)}}{2\left\{1-\left(\frac{1-\nu}{E}\right)\left(\frac{r_{io}^2 p}{r_{eo}^2-r_{io}^2}\right)\right\}} \quad [25]$$

where v is the Poisson coefficient and E is Young's modulus.

Replacing the internal volume of the tube with the inner radius and length of the tube in the density yields.

$$\rho_F=\frac{m_f}{V_i(T,p)}=\frac{m_f}{\pi r_i^2 L}=\frac{m_f}{L_{oo}}\left(\frac{1}{\pi r_i^2 dL}\right) \quad [26]$$

According to Bouchot and Richon [22], for a U-shaped thick-walled tube with its two branches in the same vertical plane, the ratio of internal and external radii is a good substitute for the second moment of inertia, so that:

$$\frac{I}{I_o}=\frac{\Delta r^4}{\Delta r_o^4}=\frac{r_e^4-r_i^4}{r_{eo}^4-r_{io}^4} \quad [27]$$

Similarly they replaced the relative inverse cube length with an expression containing the linear pressure expansion coefficient (γ_T), yielding:

$$\left(\frac{L_o}{L}\right)^3=\exp(-3\gamma_T p) \quad [28]$$

For same reference temperatures the ratio E/E_o in equation 19 equals unity because an only thermal change affects the Young's modulus. Finally, substituting equations 26, 27 and 28 into equation 19, produces the FPMC working equation.

$$\rho_F(T,p) = \frac{m_T}{L_{oo}}\left(\frac{1}{\pi r_i^2(T,p)\delta L(T,p)}\right)\left\{\left(\frac{\Delta r^4(T,p)}{\Delta r_o^4(T)}\right)\exp(-3\gamma_T P)\left(\frac{\tau^2(T,p)}{\tau_o^2(T)}\right)-1\right\} \quad [29]$$

As in Outcalt and Mclinden, Bouchot and Richon [23] use a quadratic empirical correlation in temperature (equation 22) for the resonance period at vacuum.

The FPMC model requires a calibration fluid for fitting two parameters: m_T/L_{oo} and γ_T. They test the model with an Anton Paar DMA 512 cell for temperatures between 253 K and 333 K, using dichlorodifluoromethane (R-12) as the calibration fluid. They claim an uncertainty of ±0.15 kg·m^{-3} for pressures up to 40 MPa.

In 2015, Iglesias-Silva et al. [24] performed a calibration using the FPMC model with water and *n*-heptane as calibration fluids. The apparatus was a vibrating tube DMA 512P provided by Anton Paar, and the operating limits were temperatures between 283.15 K and 363.15 K at pressures up to 65 MPa. They proposed a modification in the FPMC, including a reference pressure in equation 25. Also, they corrected the resonant period of oscillation at vacuum by making vacuum measurements before every isotherm. They claimed an uncertainty equivalent to ±(0.2 – 0.4 kg·m^{-3}), where the main contributions result from apparatus resolution and pressure uncertainty. In conclusion, the FPMC reduces errors associated with calibration fluids, however it requires accurate reference values for internal and external radii.

Physical based calibration model for high pressure VTDs

The force path calibration method provided a good representation of vibrating tube behavior for pressures up to 65 MPa. In 2014, May et al. [25] developed a physical calibration model for high pressure vibrating tubes. This model is an extended version of Holcomb and Outcalt [16] with some similarities to the FPMC model. Equation 19 describes the relationship of the fluid density and period of resonant oscillation, but description of physical properties and assumptions vary.

May et al. proposed a relationship in temperature and pressure for the second moment of inertia (I),

$$\frac{I}{I_o} = 1 + 4\alpha_1 T + \left(6\alpha_1^2 + 4\alpha_2\right)T^2 + \beta_I p \qquad [30]$$

For Young's modulus (E) they used a quadratic temperature dependence,

$$\frac{E}{E_o} = 1 + \epsilon_1 T + \epsilon_2 T^2 \qquad [31]$$

The length and volume corrections are

$$L = L_{00}\left(1 + \alpha_1 T + \alpha_2 T^2 + \beta_L p\right) \qquad [32]$$

and

$$V_i = V_{00}\left(1 + 3\alpha_1 T + 3\left(\alpha_1^2 + \alpha_2\right)T^2 + \beta_v p\right) \qquad [33]$$

where α_1 and α_2 are the first and second order linear temperature coefficients, and β_L and β_v are the linear and volumetric mechanical deformations respectively. The measuring tube in the high pressure Anton Paar VTD is constructed of Hastelloy C-276. From the physical properties of Hastelloy, May et al. [25], conclude that second order

variations with temperature are negligible in equations 30 – 33 for this temperature range, but the pressure dependence of the elastic properties of the tube is significant for high-pressure measurements. They also conclude that explicit linear thermal corrections in Young's modulus are not necessary because such effects are incorporated into the temperature dependence of the vacuum resonant period (τ_0). The resulting working equation for high pressure VTD's is:

$$\rho_F = \frac{\rho_{00}}{\left(1+\alpha_v T+\beta_v p\right)}\left[\left(\frac{\tau}{\tau_0}\right)^2\left(1+\beta_\tau p\right)-1\right] \qquad [34]$$

Following Outcalt and McLinden [22], May et al. used a quadratic function to describe the temperature dependence of the period of resonant oscillation at vacuum, resulting in an alternate working equation

$$\rho_F = \frac{\rho_{00}}{\left(1+\alpha_v T+\beta_v p\right)}\left[\left(\frac{\tau}{\tau_{00}(1+\epsilon_{\tau 1}T+\epsilon_{\tau 2}T^2)}\right)^2\left(1+\beta_\tau p\right)-1\right] \qquad [35]$$

Three coefficients (τ_{00}, $\epsilon_{\tau 1}$ and $\epsilon_{\tau 2}$) in equation 35 come from a separate fit of τ_0 to vacuum resonant period data, and the remaining four parameters (α_v, β_v, β_τ and ρ_{00}) come from fits to measurements on one or more calibration fluids.

May et al. [25] performed calibration measurements with water and toluene to fit the parameters in equation 35. They validated their calibration model by comparing physical values for Hastelloy from the literature to the fit parameters α_v, β_v and β_τ. This physically-based model reduces influence of calibration fluids and reproduces data within ±(0.4 – 0.8 kg·m^{-3}).

1.2 Nitrogen + methane data sets

Many authors have performed accurate density measurements for pure fluids using different techniques. Mantilla et al. [8] measured nitrogen over a wide range of temperatures using a MSD, and Cristancho et al. [26] did same for methane with pressures up to 180 MPa. However, development of equations of state requires accurate mixture data as well. Density data for binary mixtures allow calculation of parameters that describe molecular interactions. Some authors have studied the mixture methane + nitrogen, but the high-pressure region lacks accurate data.

In 2006, Chamorro et al. [27] used a single-sinker MSD to measure some methane + nitrogen mixtures at temperatures between 240 K and 400 K at pressures up to 20 MPa. They claimed an uncertainty of ±0.02 % for densities covering compositions of approximately 0.1 and 0.2 nitrogen mole fractions. These are accurate p-ρ-T data for the single phase, but they are at low pressure. In 1980, Straty and Diller [28] measured liquefied and compressed nitrogen + methane samples at 0.3, 0.5 and 0.7 methane mole fractions. They covered temperatures from 75 K to 300 K at pressures up to 30 MPa, using a gas expansion technique with uncertainties between 0.1 % and 0.3 % in density.

In 1996, Seitz et al. [29] used a VTD to measure densities for nitrogen + methane mixtures with 0.1 to 0.9 methane mole fractions. They covered a temperature range from 240 K to 500 K at pressures up to 100 MPa. Because of apparatus limitations and calibration methodology, authors claimed an uncertainty no lower than ±1 $kg \cdot m^{-3}$. These data offered an idea of the behavior of the binary interactions, but errors in prediction might occur because high uncertainty in the high-pressure region. Additionally, no data

are available for pressures higher than 100 MPa. To improve predictions in the supercritical region, it is necessary to conduct experiments with lower uncertainties and at higher pressures.

1.3 Modern functional for equations of state

Density measurements are essential for development of thermodynamic correlations. However, accurate equations of state also must predict accurately other thermophysical properties such as energies and entropies. While no direct methods exist for measuring energies or entropy directly, a combination of p-ρ-T data, speed of sound data, calorimetric data and other experimental measurements describe the behavior of pure fluids and mixtures.

Many equations of state have appeared over the years. Process modeling uses modified versions of cubic equations of state because they offer a good representation of fluid behavior with a simple mathematical form. However, some applications require more accurate representation of the fluid properties. Currently, some multi-parametric equations of state are an alternative for accurate predictions of thermophysical properties.

The multi-parametric equations of state are highly accurate thermodynamic correlations covering wide ranges of pressure and temperature. These equations have empirical forms and fitted parameters. Developing these correlations requires accurate p-ρ-T data, speed of sound data and isochoric heat capacities.

Historically, equations of state described pressure as a function of temperature and density. However, equations of state based upon fundamental properties such as internal energy, $u(s,\rho)$, enthalpy, $h(s,p)$, Helmholtz energy, $a(T,\rho)$ and Gibbs energy, $g(T,p)$, contain all thermodynamic information required using their derivatives. This approach makes energy calculations easier and produces stable predictions. Moore, et al. [30] used Helmholtz energy for developing a multi-parametric equation of state in 1969.

The Helmholtz energy can be described as a combination of an ideal and a residual contribution. The ideal term in Helmholtz energy has a theoretical form based upon the ideal gas, but the residual part requires an accurate description of the real substance. In 1985, Schmidt and Wagner [31] proposed an empirical form for the residual Helmholtz energy as a function of the reduced density (δ) and temperature ($1/\tau$).

$$a^r(t,\delta) = \sum_k N_k \delta^{i_k} t^{j_k} + \sum_k N_k \delta^{i_k} t^{j_k} \exp\left(-\delta^{l_k}\right) + \sum_k N_k \delta^{i_k} t^{j_k} \exp\left(-f_k\left(\delta - 1\right)^2 - b\left(t - 1\right)^2\right) \qquad [36]$$

Different authors have developed equations of state for pure fluid components using this functional with remarkable results. Some examples are the nitrogen EoS from Span et al. [32], carbon dioxide EoS from Span et al. [33], argon EoS from Tegeler et al. [34], propane EoS from Lemmon et al. [35] and methane EoS from Setzmann and Wagner [36]. This modern functional can describe thermophysical properties for saturated and homogeneous phases.

The modern equation has three kinds of mathematical functions: polynomial functions in density and temperature, polynomials and exponentials terms combined and

Gaussian bell shaped terms. This mathematical function can predict the behavior of fluids in liquid + vapor, single-phase and critical regions with high accuracy. The Gaussian bell-shaped terms improve the predictions near critical point by adding empirical parameters φ_k and β. However, a different number of terms exist for each summation, which also varies for each component. According to Span et al. [31] the bank of possible terms in the optimization procedure contains a total of 838 terms.

In 2012, Kunz and Wagner [37] presented the GERG-2008 equation of state. This equation uses modern equations of state developed for pure fluids, and proposes a mixing rule methodology for 21 components. Some of the components are: methane, ethane, propane, butane, carbon dioxide, nitrogen and hydrogen sulfide. GERG-2008 makes remarkable predictions for natural gas samples. Atilhan et al. [7] and Patil et al. [4] showed that for synthetic natural gas samples rich in methane, GERG-2008 predicts density values within ±0.25 %. In general, the modern form makes outstanding predictions. However, this mathematical form requires significant computational time because of its complexity. GERG-2008 is a remarkable tool for reference but is not recommended in process design, because the computational time required for complex is excessive. A different mathematical form for the residual Helmholtz energy can offer similar predictions with lower computational requirements.

1.4 Objective

This work seeks to contribute new experimental data and new thermodynamic correlations. The contributions fall into four specific topics:

1. Design of a vibrating tube apparatus for accurate measurement of gases at elevated pressures.
2. Perform density measurements for pure components and nitrogen + methane mixtures for pressures up to 140 MPa.
3. Development of a new equation of state based upon a rational functional form for the residual Helmholtz energy.
4. Development of a mixing rule based upon Helmholtz energy and a rational equation of state.

Section 2 offers a brief description of a new vibrating tube apparatus that includes uncertainties of sensors and operational limits. This section also presents the calibration methodology. Finally, it contains a brief explanation of a mixture preparation procedure.

Section 3 presents calibration results for the VTD using methane, argon and nitrogen including an uncertainty analysis for the measurements. In addition, this section contains accurate VTD measurements of fluid densities. The data include carbon dioxide and ethane density measurements for temperatures from 300 to 470 K at pressures up to 140 MPa. Section 3 also presents density measurements for three nitrogen + methane mixtures containing nominal methane mole fractions of 0.25, 0.50 and 0.75.

Section 4 presents a new functional for the residual Helmholtz energy using a rational polynomial form in density and temperature. This new equation of state can predict various properties with accuracies similar to existing reference equations of state, while requiring much less computational time. The section presents equations of state based upon the new form for nitrogen, argon and methane to demonstrate accuracy of the results.

Section 5 proposes a new mixing rule for gas mixtures. This mixing rule uses a rational form for Helmholtz energy interactions similar to the equation in Section 4. This new strategy is applied to nitrogen + methane density data.

2. VIBRATING TUBE DENSIMETER APPARATUS

A fast and accurate method to measure densities in gas mixtures and corrosive fluids over wide ranges of pressure and temperature is desirable. One available method is the VTD, which can perform density measurements with reasonable accuracy. Previous works have developed apparatus and methodologies for measuring densities of liquid and gases at low pressure. Few previous works measure gases at supercritical conditions.

This section focuses upon experimental procedures and design for the VTD apparatus to make accurate measurements of gas densities up to 140 MPa. The apparatus includes a compression system, vacuum system, manifold, pressure measurement, data acquisition system and temperature control. This section also contains a brief description of the apparatus used to prepare mixtures of accurately known composition. Finally, this section reveals a calibration methodology based upon the work of May et al. [25].

2.1 Apparatus description

The principal components of the VTD are the measuring cell (Anton Paar® DMA HPM), an interface module, and an evaluation unit (mPDS). The auxiliary instruments include: a gas booster for charging the test sample, pressure measurement systems, a hand pump, a vacuum system, a temperature control system and a computer for data acquisition and control. The operating limits for this apparatus are 263 K to 473 K (15 °F to 400 °F) up to 137 MPa (20,000 psia).

The vibrating tube apparatus provides density measurements in a relative short time using small amounts of sample. As a result this technology reduces operating risks, becoming an alternative for corrosive and dangerous fluids characterization. The apparatus resides inside a walk-in fume hood, avoiding direct exposure to the sample in a case of an unplanned release. Figure 5 shows a schematic diagram of the apparatus.

2.1.1 Apparatus design

2.1.1.1 Feed manifolds and cylinder storage

Figure 5 includes feed manifolds for the vibrating tube apparatus. Samples and auxiliary gas cylinders are stored in a service hall outside of the laboratory room. The cylinders are connected to the apparatus using stainless steel 1/8" Swagelok tubes. Auxiliary gas cylinders are: low purity nitrogen for operation of the gas booster, low purity argon and low purity methane for piston sampler operation.

To avoid phase separation in gas mixtures, a cylinder warmer keeps samples above 45 °C. Briskheat® has supplied the cylinder warmer (8" diameter x 48" tall) that uses 120 VAC with a total of 150 watts. It has self-regulation temperature system and the maximum allow working temperature is 66 °C. The feed manifold includes: eight 1/8" high-pressure valves provided by HiP® (High Pressure Equipment Company) with rated working pressures of 30,000 psi, two rupture disks rated at 35,000 psi, two relief valves rated at 2,200 (RV2) or 3,000 psi (RV1) and a mechanical pressure gauge rated up to 30,000 psi. All connecting lines are 1/8" diameter Type 316 stainless steel provided by HiP® with rated working pressures of 30,000 psi.

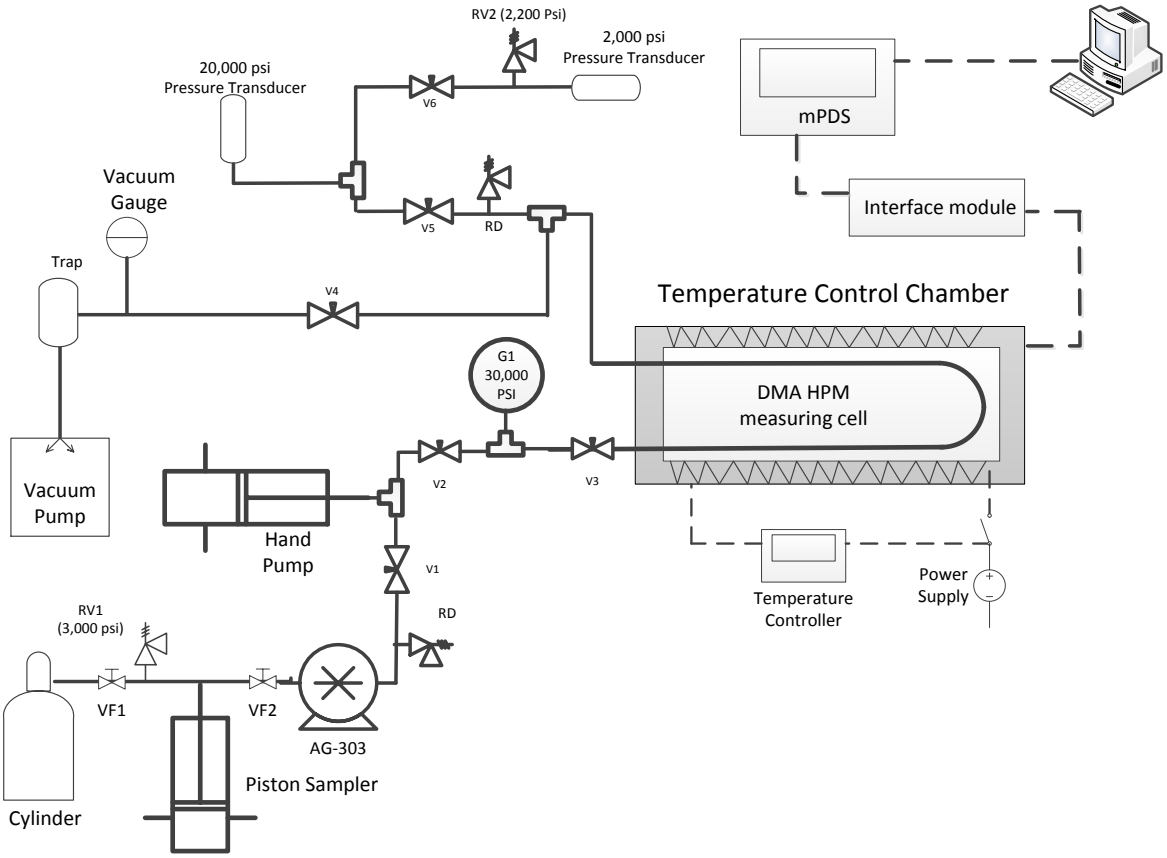

Figure 5. Schematic diagram of vibrating tube apparatus

2.1.1.2 Compression system

The apparatus has a versatile gas compression system that is capable of increasing the pressure in the vibrating tube apparatus up to 20,000 psi. The main instrument in the compression system is an oil-free Haskel gas booster, model AG-303. This compressor has a maximum outlet pressure of 39,000 psi and requires a minimum inlet pressure of 500 psi. It uses low purity nitrogen at 120 psi as a driving fluid. Increasing the drive pressure to 150 psi provides better performance for sample supply

pressures below 1,000 psi. The gas booster is a piston-chamber arrangement where the displacement of the piston decreases the volume thereby increasing pressure. Two check vales prevent back-flow of gas at both suction and discharge sides. At optimal conditions, the booster can increase the pressure up to 20 times the inlet pressure, but for this configuration the realized pressure ratio is about 10.

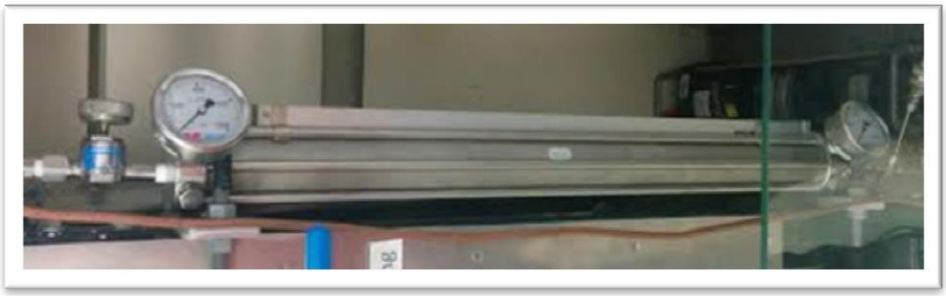

Figure 6. Piston sampler for pressurization of gas samples

The gas booster cannot operate with an inlet pressure lower than 500 psi, so gas mixtures at lower pressures require a pre-pressurization stage. A piston sampler device, see figure 6, with a maximum allowable working pressure of 1,800 psi serves as a secondary container. This device is a cylinder with a displaceable wall that moves under pressure differential, creating two chambers at mechanical equilibrium with variable volume. Also each chamber has independent gas inlet valves. After evacuation of each chamber and keeping VF1 and VF2 open, one of the chambers is filled with sample at gas cylinder pressure. Later, VF1 is closed to avoid back flow, and the other chamber is filled with a driving gas at the desire pressure. This driving gas can be low purity nitrogen, argon or methane. A pressure higher than 500 psi enables gas booster

operation, but an inlet pressure higher than 1,000 psi improves performance of the booster.

Gas boosters are effective for gross pressure increases, but they are not reliable for pressure tuning. The compression system includes a manually operated piston screw pump (hand pump) provided by HiP®, with maximum allowable working pressure of 30,000 psi. This instrument has a variable volume of 11 cc that allows pressure tuning. Because of the small volume of the VTD system, the hand pump can increase pressure from 10,000 psi to 20,000 psi in a single stroke. The hand pump is loaded with sample using the gas booster while fully open, then the volume is decreased to increase pressure. Later V1 is closed to avoid back flow and dead volumes. The process can be repeated as many times as required.

2.1.1.3 Vacuum system

The apparatus requires a vacuum system to remove residual gases to avoid sample contamination. Figure 5 shows the vacuum system connected to the VTD through V4. The system has a HP Varian model SD-200 mechanical pump with a free air displacement capacity of 10 m^3/hr and an ultimate vacuum of 10 mTorr. A thermocouple gauge measures the vacuum in the system. An oil trap between the mechanical pump and the system absorbs any oil that migrates from the pump toward the system.

2.1.1.4 Isothermal chamber

For accurate density measurements, the temperature in the vibrating tube apparatus must be stable so the measurement cell resides within a temperature control chamber. Figure 7 provides a schematic of the temperature control chamber.

Within the chamber, an aluminum cylinder provides an isothermal temperature shield. The isothermal shield is constructed from a piece of aluminum tubing alloy 6061 with 5 mm wall thickness and an inner diameter of 12.5 cm. Two cylindrical plates cover the ends to provide a complete enclosure.

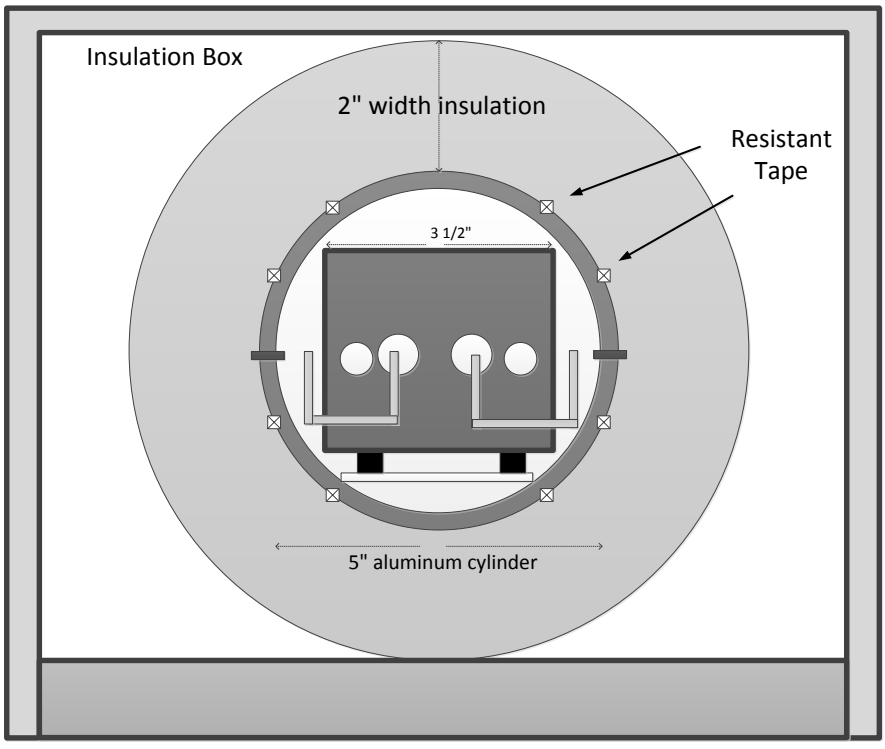

Figure 7. Isothermal shield for temperature control

The inner layer is a cellular glass insulation (FOAMGLAS®, manufactured by Pittsburgh Corning Corp) with a thermal conductivity of 0.042 $W \cdot m^{-1} \cdot K^{-1}$ rated up to

482 °C. It has an internal diameter of 6 inches and a wall 2 inches wide. Because FOAMGLAS is a fragile material susceptible to breaking under mechanical stress, then insulation cylinder is placed inside a PVC cylinder to reduce mechanical stress caused by the weight of the measurement cell. The PVC container consists of a split 11 inches internal diameter PVC pipe secured with two metal clamps. Figure 8 shows a picture of the insulation, the PCV cylinder and the metal clamps. The outer layer is a rectangular box made from foam sheets to minimize ambient air flow and stabilize the inlet line temperatures. Figure 7 is a schematic of the measurement cell inside the isothermal shield, including insulation box and cylinder.

Figure 8. FOAMGLAS insulation inside a PVC cylinder and secured with metallic clamps

The temperature sensor for the isothermal shield is a resistance thermometer (RTD) placed on the surface of the aluminum cylinder. The RTD provided by OMEGA® is a flat-shape sensor with a nominal resistance of 100 Ω at 0 °C. This thermometer is

accuracy class B, with 0.3 °C variation within a range of -50 °C to 500 °C. A heating tape with a resistance of 4.9 $\Omega \cdot ft^{-1}$ and maximum output energy of 52 $W \cdot ft^{-1}$, provided by Clayborn®, provides energy the aluminum shield. Two sets of tape are connected in series. One set is placed on the upper half of the cylinder and the second on the lower half to allow easy disassembly of the aluminum shield for internal modifications and repairs. The heaters are connected to a variable AC power supply with a maximum voltage of 140 V. Optimal voltage values and control parameters vary with the set temperature.

2.1.1.5 Temperature control

The temperature control routine utilizes a PID strategy implemented in Labview® 2012 to control the temperature of the isothermal shield. The RTD temperature is the control variable. The error or offset between observed temperature and the user specified set point is:

$$e(t) = T_{RTD}(t) - T_{SetPoint}(t) \quad [37]$$

The PID control algorithm has three components: proportional, integral, and derivative. The value of the manipulated variable I for PID control is:

$$u(t) = K_p e(t) + K_i \int_0^t e(t)\,dt + K_d \frac{\partial e(t)}{\partial t} \quad [38]$$

In this application, the manipulated variable is the amount of energy supplied to the cylinder by the heater tape. When using a fixed voltage supply to the heaters, the

amount of energy using an ON/OFF strategy where the ratio of time on to time off varies proportionally with $u(t)$ from equation 38.

A National Instrument® data acquisition card (DAQ, NI USB-6501) with 24 digital input/output lines provides the interface between the computer and the heater power supplies. Every temperature reading cycle takes 5 s, so the maximum output signal from the PID controller is equivalent to 5 s on and 0 s off. The DAQ generates a logic digital signal alternating between 0 and 5 volts. This signal stays active for a time equivalent to the PID controller output. A solid-state relay receives the logical command and allows or stops current flow through the heater tape.

Figure 9 represents the control loop for the isothermal aluminum cylinder. This includes the sensor (RTD), the controller (computer -DAQ) and the manipulated device (Relay). As a safety feature, an electronic switch sensitive to temperature located on the cylinder surface protects against overheating beyond the working range of the measuring cell by opening the electric circuit when the switch temperature exceeds 220 °C.

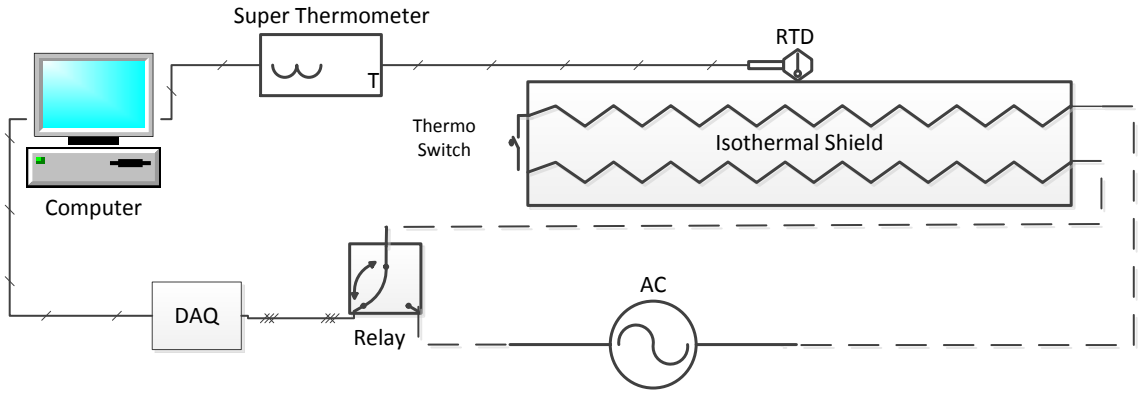

Figure 9. Diagram of a PID temperature controller in a feedback loop

2.1.2 Density measurement

The measurement cell is a commercial vibrating tube densimeter manufactured by Anton Paar® (DMA HPM). This unit can perform density measurements for fluids (liquid or gases) at temperatures from -10 °C to 200 °C and pressures from 0 to 1400 bar (20,000 psi). Figure 10 is an image of the DMA HPM cell, interface module and evaluation unit (display).

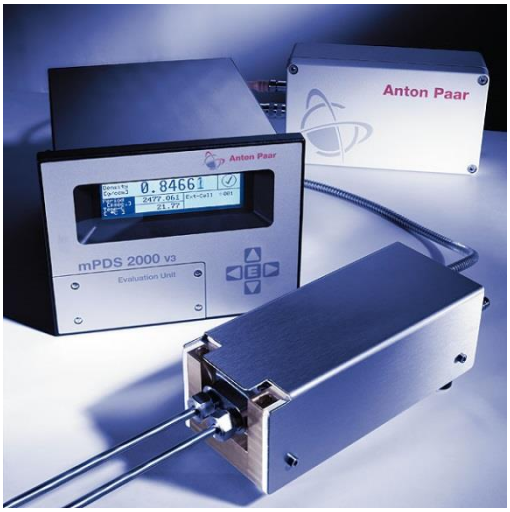

Figure 10. DMA HPM cell (bottom), interface module (upper right) and display unit (upper left) provided by Anton Paar. Acknowledgement: Anton Paar website

The DMA HPM has a U-shaped Hastelloy C-276® tube, two coils, two magnets, a base, an insulation block and a frequency counter [16]. This device uses the resonance frequency of the tube to determine fluid densities. Two small magnets at the free end of the vibrating tube and two coils mounted on the base create the oscillation. An external current source activates one of the coils (drive coil) using a pulse and it applies a force on one the magnets, moving the tube continuously. As the tube moves transversely, the second magnet moves relative to the second coil (pick-up coil), thereby inducing an

electric current with the same frequency as the tube vibrations. A frequency counter located at the bottom of the pick-up coil measures the frequency of the signal. The cell uses a feedback loop to optimize time between drive pulses in first coil to the resonant frequency of the tube. Also, an isolation block clamps both sides of the tube and protects it from external vibrations. Changes in tube oscillation represent fluid density variations because the resonant frequency of the tube is related to the mass of the tube and fluid cd within. The DMA HPM measurement cell has 6 mm inlet and outlet tube connections with a rated working pressure of 20,000 psia. Anton Paar also provides a temperature sensor located inside the measurement cell. Because this sensor has a range of -10 $^{\circ}$C to 200 $^{\circ}$C with a resolution of 0.1 $^{\circ}$C, it does not have sufficient accuracy to serve as the primary temperature measurement device.

The DMA HPM is connected to an interface module using a metal-jacketed cable. This module generates and produces the pulse required in the oscillation control loop [38]. Also, a sensor located inside the DMA HPM cell provides internal temperature measurements. A display unit (mPDS 200V3) receives and sends the data from the interface module to the computer.

2.1.3 Pressure measurement

For pressure measurement, the apparatus uses two oil-free absolute pressure transducers provided by Paroscientific®. The transducers have ranges of 2,000 psi (13.7 MPa) and 20,000 psi (137 MPa) with uncertainties of ±0.01 % full scale. A combination of two transducers allows high-pressure measurements while preserving accuracy at low

pressures. For pressures below 2,000 psi, the apparatus the uncertainty is ±0.2 psi (±0.00138 MPa), while for pressures higher than 2,000 psi, the uncertainty is ±2 psi (±0.01378 MPa).

Paroscientific Pressure transducers utilize a sensing mechanism that, through mechanical coupling, results in the variation of the resonant frequency of a quartz crystal with the pressure inside the transducer. The resonant frequency also varies with temperature, so the temperature must be monitored and a correction applied for temperature changes. A second quartz crystal, which is not coupled to the internal pressure, provides a temperature measurement. The transducer output contains two variables, each of which is a period of resonant oscillation. One is related to pressure (X_p), and other to temperature (T_p). A Model 735 display receives information and calculates pressure and temperature. Appendix A.2 contains the calibration coefficients used for calculating pressure using the periods provided by transducers, and details of the calibration certification.

Because temperature affects both the resonant frequency and the mechanical coupling mechanism, Paroscientific models offer error compensation for temperature. Because experience has shown that transducer performance is better when maintained at constant temperature, so the transducer temperatures are controlled at 50 $^{\circ}$C. This temperature is chosen to be near the upper end of the operating range to minimize the possibility of condensation or adsorption in the transducer or connecting tubing. Figure 11 shows a schematic drawing of the aluminum block that provides an isothermal environment for the transducers. An Omega i-series 1/32 temperature controller with a

RTD input sensor controls the temperature to ±0.2 °C by delivering electric power to two cylindrical cartridge heaters located in the block.

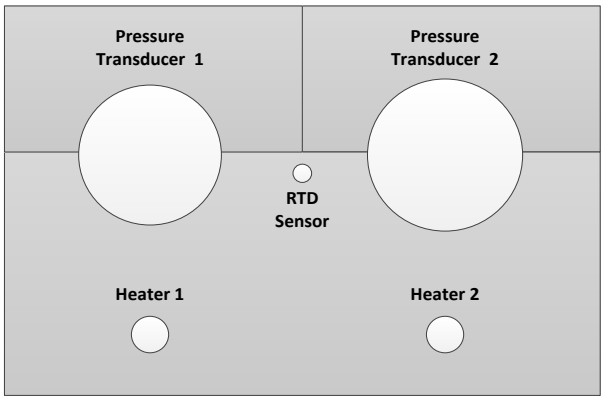

Figure 11. Schematic diagram of aluminum block that provides isothermal environment to the pressure transducers

2.1.4 Temperature measurement

The primary temperature sensor is a standard platinum resistance thermometer (SPRT), provided by Fluke Calibration (Model 5686-B Glass capsule SPRT, report number B3820054), and located in a thermometer well at the end of the measurement cell. This SPRT has a nominal resistance of 25 Ω with an operating temperature range of -260 °C to 232 °C. The reproducibility is ±0.001 °C or better with a drift of less than 0.001 $^{\circ}C \cdot yr^{-1}$. The manufacturer calibrated the SPRT on the ITS-90 thermometry scale. The calibration equation and parameters are given in in Appendix A.2.

A Fluke 1594A Super-Thermometer serves as the measuring instrument for both the SPRT and RTD. The 1594A Super - Thermometer is capable of measuring up to four sensors in a four wire configuration with a resolution ±0.000015 °C. The 100 Ω standard resistance that serves as the resistance reference has a 1-year stability equivalent to

±0.001 °C. Figure 12 shows an image of the instrument and a schematic representation of the thermometer lead wire configuration.

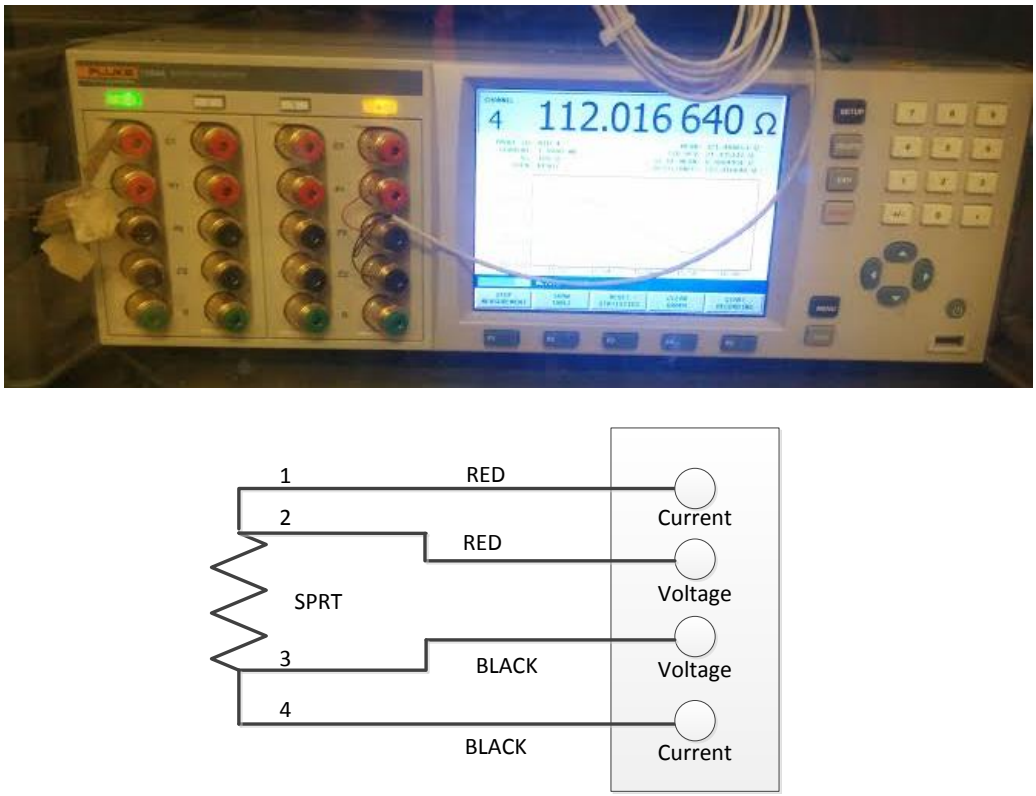

Figure 12. Top: Picture of Fluke 1594A Super-Thermometer Bottom: schematic representation of thermometer connection

The instrument measures voltage difference (V) between leads 2 and 3 that results from a constant current (I) that passes through leads 1 and 4. The SPRT resistance is given by:

$$R_{SPRT} = \frac{V_{SPRT}}{I} \qquad [39]$$

The super thermometer uses an external resistor to determine the current. The same current goes through the reference resistor and the SPRT. Using equation 39 for both resistances and solving the resulting simultaneous equations produces:

$$R_{SPRT} = \frac{V_{SPRT}}{V_{Ref}} R_{Ref} \qquad [40]$$

The RTD and SPRT sensors use the same methodology for measuring resistance values, but the conversion equations from resistance to temperature vary with each sensor. The SPRT uses the ITS-90 calibration equation and the RTD uses the Callendar-Van Dusen equation. These conversion equations and the calibration parameters appear in Appendices A.2 and A.3.

2.1.5 Labview data acquisition programs

During an experiment, a Labview® 2012 program records temperatures, pressures and periods of vibration approximately every 5 seconds. For every experiment the routine creates two output text files. One file includes all experimental variables for the entire experiment and the other (results file) includes some selected values for use in subsequent calculations. The results file records pressure, temperature, vibrational periods, and other significant information only when the system reaches equilibrium.

Calculation of the density of the fluid inside the apparatus requires pressure, temperature and period of oscillation values at equilibrium and a calibration model. The program also calculates the standard deviation for every experimental property using the last 10 minutes of measurements. The program determines when the system reaches

equilibrium using stability tolerance values that are specified by the user. When the standard deviations of all variables satisfy the specified tolerances, the system is at equilibrium. The recommended values for stability tolerances usually are the sensor uncertainties. To avoid false positives in detecting equilibrium, the program imposes a 20 minutes delay time after equilibrium is reached. The program then records and averages all experimental properties during a specified period (10 minutes) to reduce errors caused by noise.

The Labview® user interface has 6 tabs, each of them with different task. The first tab contains values from the RTD (Resistance thermometer) that read cylinder temperature (in $^{\circ}$C) from the super thermometer device. This tab also includes parameters for temperature control loop (set point, proportional gain, integral and derivative constant). The second tab shows VTD temperature from the measurement cell sensor, temperature from the SPRT and the standard deviation of this temperature. Third tab includes resonance period of oscillation with its standard deviation and average. The fourth and fifth tabs have pressure and temperature values from two pressure transducers. Finally the sixth tab has a preliminary value of density calculated continuously.

2.1.6 Sample preparation

This work performs density calibration measurements for three pure components (methane, nitrogen and argon). Research-grade ultra-high purity samples reduce errors caused by impurities in samples. The nitrogen sample came from Airgas with a specified

mole fraction of 0.999995. The argon and methane came from Airgas, both with a specified purity of 0.99995.

Carbon dioxide and ethane density measurements validate the calibration methodology. Matheson–Tri–Gas provided carbon dioxide with a specified purity of 0.99999 and ultra-high purity ethane with 0.9995 specified purity.

Finally, this work performs density measurements for nitrogen + methane mixtures at three different compositions using the VTD in the range of 303 K to 470 K at pressures up to 140 MPa. The mixtures are prepared in previously evacuated LP-50 aluminum cylinders using a gravimetric procedure. A Sartorius® IS64EDE-H balance with a resolution and repeatability of 0.1 g provides the mass measurements. The total amounts of sample varied from 2,500 g to 3,200 g so that the total uncertainty in composition is less than ±0.0004 molar fraction. Figure 13 shows a schematic of the mixture preparation apparatus, including the balance/cylinder enclosure and the temperature (T1) and pressure (P1) sensors used to calculate air buoyancy corrections.

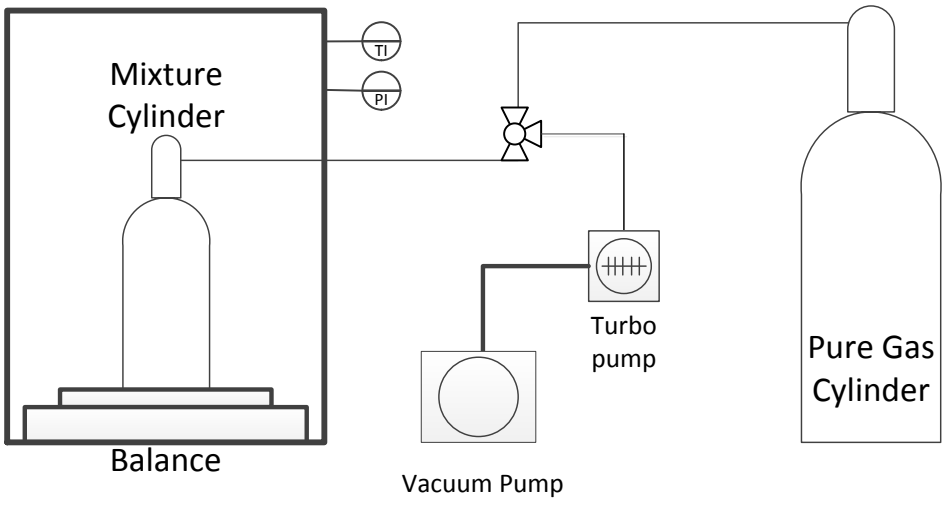

Figure 13. Schematic of gravimetric mixture preparation apparatus

2.2 Calibration methodology

The VTD requires a calibration equation to convert resonant period measurements into density of a fluid. The resonant period of the tube is a function of temperature, pressure and mass, but it is not a function of the physical properties of the contained fluid. Thus, a well-known fluid can be a reference for developing a calibration equation.

According to some authors [16] [23], calibration methodology defines the accuracy of the apparatus. There are empirical, semi-empirical and physically based calibration models. Bouchot and Richon [23] proposed a forced path mechanical calibration (FPMC) model, trying to set realistic paths for mechanical properties with variations of temperature and pressure. This physically based model limits the influence of calibration measurements when estimating densities. However, this model applies to apparatus with limited ranges in pressure and tubes with thin walls.

This work uses a calibration equation model similar to that of May et al. [25], which is an extended version of the one proposed by Holcomb and Outcalt [16] and with some similarities to the FPMC. May et al. describe the oscillation in the vibrating tube system as a freely vibrating uniform cantilever. They proposed an equation of motion and boundary conditions to solve system for resonance conditions. As in equation 19, May et al. [25] describe density of the fluid as a function of Young's modulus (E), moment of inertia (I) and length of the tube (L).

Using the mechanical properties for Hastelloy 265C, they defined Young's modulus, length of the tube and inertia moment as functions of temperature and pressure. Making some arrangements and simplifications, they recommended

$$\rho_F = \frac{(\rho_{00})}{(1+\alpha_v T+\beta_v P)}\left[\left(\frac{\tau}{\tau_{00}(1+\epsilon_{\tau 1}T+\epsilon_{\tau 2}T^2)}\right)^2(1+\beta_\tau P)-1\right] \quad [41]$$

for calibrating VTDs over wide pressure ranges.

The linear ($\varepsilon_{\tau 1}$) and quadratic ($\varepsilon_{\tau 2}$) temperature response coefficients and the resonance period of the tube (τ_{oo}) come from an empirical quadratic correlation in temperature based upon experimental measurements. However Outcalt and McLinden [22] showed that vacuum measurements do not have good repeatability and produce errors equivalent to ±0.3 kg·m^{-3}.

This work performs vacuum measurements before every isotherm, correcting vacuum values every time. Because small variations in temperature occur during an isotherm (no more than 40 mK), vacuum resonance values need corrections for temperature variations. The vacuum resonance values are expressed as a quadratic equation

$$\tau_o(T) = c_0 + c_1 T + c_2 T^2 \quad [42]$$

where the coefficients are determined using least squares regression of vacuum readings at different temperatures. A Taylor series expansion,

$$\tau_o(T) = \tau_o(T_o) + \frac{\partial \tau_o}{\partial T}(T - To) = \tau_o(T_o) + (c_1 + 2c_2 T)(T - To) \quad [43]$$

provides an expression to adjust the values of resonance oscillation (τ_o) for temperature variations. Iglesias et al. [24] showed that this approach can limit uncertainties to ±0.1 kg·m^{-3}. Values for c_1 and c_2 are 0.26259 and 0.000126 respectively for temperatures between 300 K and 470 K.

When using equation 44 to calculate resonance period at vacuum, the final calibration model is:

$$\rho_F = \frac{(\rho_{00})}{(1+\alpha_v T+\beta_v P)}\left[\left(\frac{\tau}{\tau_o(T)}\right)^2(1+\beta_\tau P)-1\right] \qquad [44]$$

where ρ_{oo} represents density at a reference state, α_v is the linear temperature response coefficient of tube volume, β_v is the pressure response coefficient and β_τ is the pressure response coefficient or spring constant. These 4 parameters have physical equivalency with mechanical properties of Hastelloy C-275, but those values vary for every apparatus and geometrical configuration.

3. DENSITY MEASUREMENTS

This VTD operates at temperatures between 300 K and 473 K at pressures ranging from 0 to 137 MPa. This system has low residence times and sample volumes compared to other accurate techniques, which reduces experimental issues associated with measuring data for corrosive and toxic fluids. The VTD measures densities by observing changes in the resonant frequency of a vibrating tube containing a specific fluid.

Equation 44 in section 2 is the calibration model, but requires four parameters that are characteristic of each specific instrument. This section contains results of a non-linear least squares minimization using densities of nitrogen, argon and methane as calibration fluids. It also includes information about equations of state used as reference models. Later, this section presents a detailed analysis for calculating experimental uncertainties.

To validate calibration, this work performs density measurement of carbon dioxide and ethane for pressures up to 140 MPa. Additionally, this section presents novel methane + nitrogen density data for three compositions up to 140 MPa. The mixing apparatus presented in section 2 prepares the mixtures gravimetrically. These new data appear as four isotherms (300 K, 350 K, 400 K and 470 K) for each composition sample. This work compared experimental data to density values calculated with GERG – 2008 [37].

3.1 Calibration results

Outcalt and McLinden [22] mention that uncertainties of reference fluids equations of state are among the highest contributors to errors. A suitable calibration fluid requires accurate density values from an equation of state within the temperature and pressure range. Figure 14 shows pressure as a function of density at several temperatures within the VTD operating range for nitrogen, helium, argon, methane, carbon dioxide and propane using REFPROP® software [39].

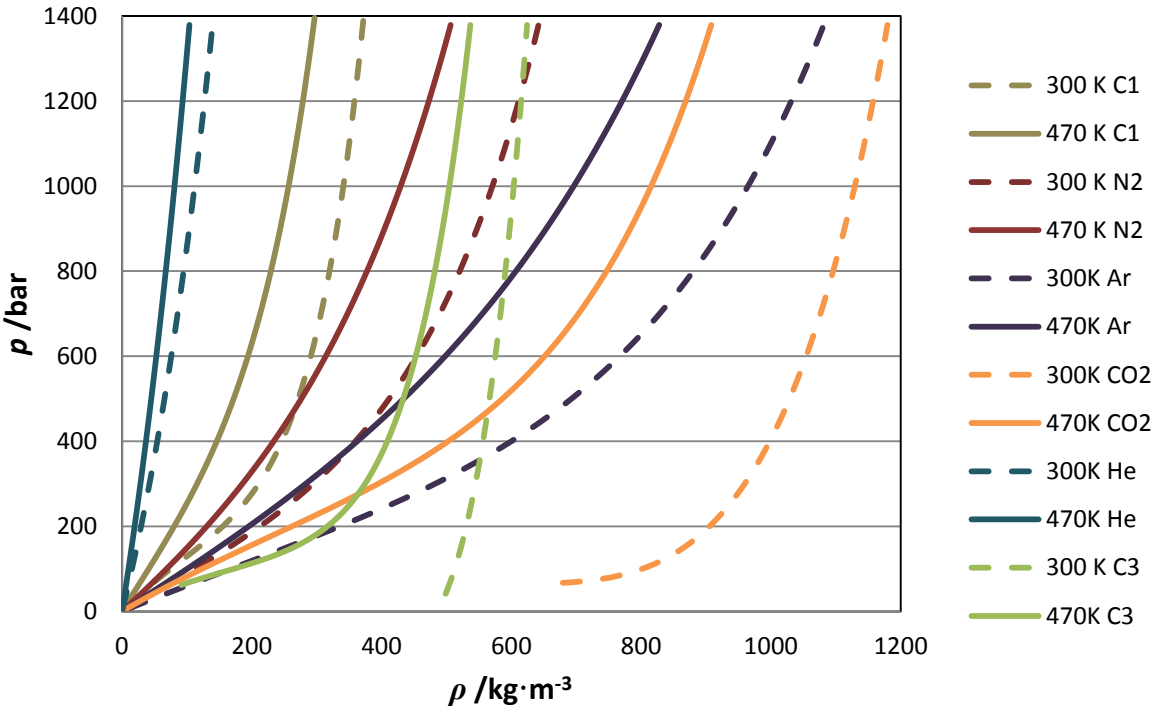

Figure 14. Density estimation using Refprop as EOS

Helium has a well-known equation of state, but it has a narrow range of density. Propane and carbon dioxide have critical temperatures within our calibration range, which can produce instability because of vapor-liquid equilibrium. Nitrogen, argon and

methane appear to be the best options for calibration fluids. Carbon dioxide is a useful alternative for future samples with density values higher than the methane-nitrogen-argon range.

This work uses highly accurate equations of state for pure nitrogen, argon and methane reducing EoS error contributions. The Span et al. [32] equation of state for nitrogen has an uncertainty of 0.02 % for densities between 240 K and 523 K and pressures up to 30 MPa. For higher pressures it claims errors less than 0.6 %. The Tegeler et al. [34] equation of state for argon behaves similarly to nitrogen with uncertainties in density of 0.03 % for pressures up to 30 MPa and less than 0.2 % for higher pressures. The Setzmann [36] equation of state for methane claims uncertainties of 0.03 % in density for pressure below 12 MPa and 0.07 % for values up to 50 MPa.

Reference equations of state need accurate data to achieve low uncertainties, but the authors did not have accurate p-ρ-T data between 40 MPa and 200 MPa during development of the equations for nitrogen, argon and methane. Mantilla et al. [8] used a MSD to show that the equation of state for nitrogen can reproduce data within 0.025 % up to 200 MPa. Also using same technique, Cristancho et al. [26] showed that the methane equation of state reproduces density values within 0.04 % for pressures up to 200 MPa for temperatures between 300 K and 450 K. Using the MSD technique [8] [26] [40], this work uses unpublished argon density measurements up to 200 MPa to show that errors in the reference equation of state for argon are less than 0.05 %. These data will appear in a subsequent publication.

The calibration measurements for nitrogen, argon and methane cover temperatures between 303 K and 474 K and pressures between 10 MPa and 137 MPa. Table B.1, B.2 and B.3 in Appendix B contain the calibration measurements for nitrogen, argon and methane.

Equation 44 describes nitrogen, argon and methane calibration data within ±0.1 $kg \cdot m^{-3}$ for densities lower than 200 $kg \cdot m^{-3}$ and ±0.05 % for densities up to 1000 $kg \cdot m^{-3}$. Table 1 contains the values and standard deviation for parameter in equation 44. It also includes values reported by May et al. [25] for several different VTD's. Figure 15 contains absolute residuals between densities calculated using reference EoS [32] [34] [36] and values estimated from equation 44.

Table 1. Values of calibration equation for Vibrating tube densimeter without outlier data

Coefficients	Values	σ	May et al.[25]
ρ_{00} / $kg \cdot m^{-3}$	16091.44	6.23	
α_v / K^{-1}	$4.348 \cdot e^{-5}$	$0.1038 \cdot e^{-5}$	$3.6 \cdot e^{-5}$
β_v / MPa^{-1}	$3.148 \cdot e^{-5}$	$0.1735 \cdot e^{-5}$	$2.3 \cdot e^{-5}$
β_τ / MPa^{-1}	$-3.191 \cdot e^{-6}$	$0.0060 \cdot e^{-6}$	-0.95 to $1.2 \cdot e^{-5}$

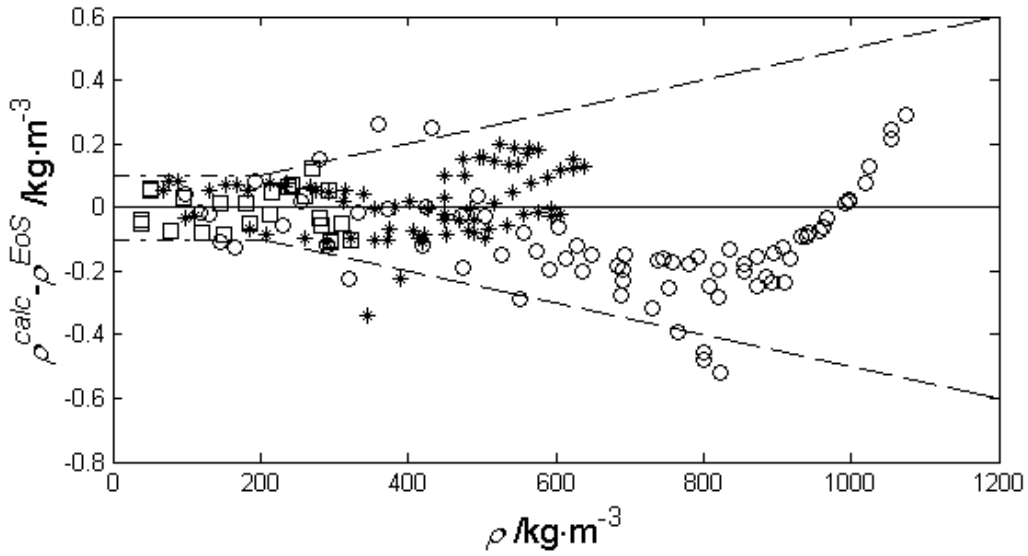

Figure 15. Absolute error for densities from equation of state (ρ^{EoS}) and densities from experimental measurements with the VTD (ρ^{calc}). (Nitrogen ✶, Argon ○, Methane □)

3.2 Uncertainty analysis

Outcalt and Mclinden [22] notes that the uncertainty in density measurements using VTDs depends strongly upon the reproducibility of vacuum readings and uncertainties in reference EoS for the calibration fluids. Overall uncertainty estimation needs all participant variables in the density calculation. The combined experimental uncertainty includes contributions from calibration errors, sensors (temperature, pressure), intrinsic errors caused by the technique (variation in period of oscillation) and composition effects as follows:

$$u(\rho) \approx u(\rho)^{cal} + \left(\frac{\partial \rho}{\partial P}\right)_{T,mi} u(P) + \left(\frac{\partial \rho}{\partial T}\right)_{P,mi} u(T) + \left(\frac{\partial \rho}{\partial \tau}\right)_{P,T} u(\tau) + \sum_{i=1}^{N} \left(\frac{\partial \rho}{\partial m_i}\right)_{P,T,m_{j\neq i}} u(m_i) \qquad [45]$$

The DMA HPM manufacturer claims density resolution and repeatability with this technique as 0.1 $kg \cdot m^{-3}$. The measured resonance values have standard deviations of approximately 0.0025 μs, which is equivalent to 0.06 $kg \cdot m^{-3}$ for 95 % confidence level. Temperatures from the SPRT have standard deviations of of approximately 1.5 mK, but the overall uncertainty with respect to ITS-90 is ±0.01 K. There are two Paroscientific pressure transducers, rated to 13.7 MPa and 137 MPa respectively, with each having an uncertaint of ±0.01 % full scale, as specified by the manufacturer. The partial derivative coefficients required for equation 45 come from the EoS.

Because the calibration technique uses three different reference fluids, it is complicated to estimate the influence of each fluid upon density uncertainties. However, the EoS for nitrogen, argon and methane do not have errors higher than ±0.05 % in density. Table 2 summarizes the overall uncertainty estimates and the specific estimates for the individual contributions.

The uncertainties vary for different values of density. The main contributions are: variability in apparatus readings and calibration fluids errors. For densities lower than 200 $kg \cdot m^{-3}$ the uncertainty is roughly ±0.1 $kg \cdot m^{-3}$ while for higher densities the errors are less than 0.05 % of value. Figure 15 verifies that equation 46 provides a good working representation of the combined uncertainty for the VTD.

$$u(r) = \pm\left(0.1\ \mathrm{kg \cdot m^{-3}} + 0.0005\, r\right) \qquad [46]$$

Table 2. Experimental uncertainty estimates

Property	Uncertainty (k=2)	Equivalence Density	Equivalent in Density (kg·m^{-3})
Period	0.005 μsec	$\left(\frac{\partial\rho}{\partial\tau}\right)_{P,T}$ from calibration equation	0.060
Temperature	2 mk	$\left(\frac{\partial\rho}{\partial T}\right)_{P,mi}$ from EOS	0.0005-0.004
Pressure	0.014 MPa* or 0.0014 MPa*	$\left(\frac{\partial\rho}{\partial P}\right)_{T,mi}$ from EOS	0.015-0.148
Calibration Error	0.01% -	Up to 640 [kg·m^{-3}]	0.128-0.55
Nitrogen	0.02%**	Up to 1000 [kg·m^{-3}]	
Argon	0.05%**	Up to 350 [kg·m^{-3}]	
Methane	0.04%**		
Overall uncertainty (k=2)			0.1-0.66

*Paroscientific Instrument provides pressure transducers within ±0.01 % at full scale.

** MSD measurements allows to reduce uncertainties in EOS component

3.3 Pure components: Carbon dioxide and ethane

Measurements for carbon dioxide and ethane as pure fluids help to validate the calibration model. This section presents the pure fluid measurements.

3.3.1 Carbon dioxide

This work contains the experimental results for carbon dioxide at three different temperatures (300 K, 400 K and 470 K) in the pressure range of 20 MPa to 137 MPa using the VTD. Table B.4 in Appendix B presents complete experimental results and

values of density from the Span and Wagner [33] EoS for carbon dioxide. Table B.4 also contains relative deviations between the experimental data and this EoS.

Figure 16 presents relative deviation as a function of pressure for 304 K, 400 K and 470 K, including error bars showing experimental uncertainties. The carbon dioxide densities at these conditions all are larger than 200 $kg \cdot m^{-3}$, so that the uncertainties equivalent to ±0.05 %. Figure 16 also includes carbon dioxide measurements performed by Mantilla et al. [40] at 310 K, 400 K and 450 K. Those measurements utilized an MSD, which does not depend upon calibration fluids [8] [41]. The VTD and MSD results agree well, proving that the calibration model is valid. The current results are the first at high pressures at 470 K.

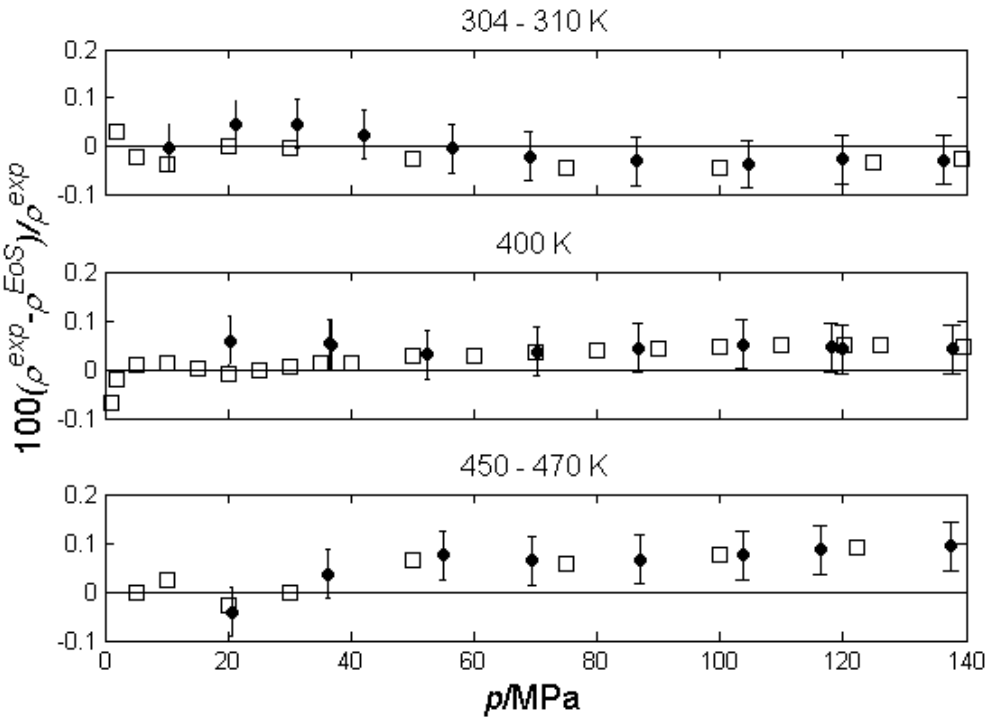

Figure 16. Carbon dioxide density measurements for this work ● (304 K, 400 K, 470 K) and Mantilla et al. □ [40] (310 K, 400 K, 450 K)

3.3.2 Ethane

The ethane density measurements performed in the VTD, at 304 K, 400 K and 470 K, from 10 MPa to 137 MPa appear in table B.5 of appendix B. Table B.5 also contains the relative deviations between the experimental densities and the Bucker and Wagner [42] EoS, which currently is the best available for ethane.

Figure 17 presents relative errors as functions of pressure, including experimental error bars. Because the vibrating tube has a minimum uncertainty of ±0.1 kg·m^{-3}, the relative deviation at 10 MPa becomes significant. Figure 17 also presents Cristancho et al. [41] ethane densities, measured using an MSD. The VTD results agree with the MSD densities, with some discrepancies at low pressure and high temperature. This region is problematic for both apparatus because of low pressure and density[9].

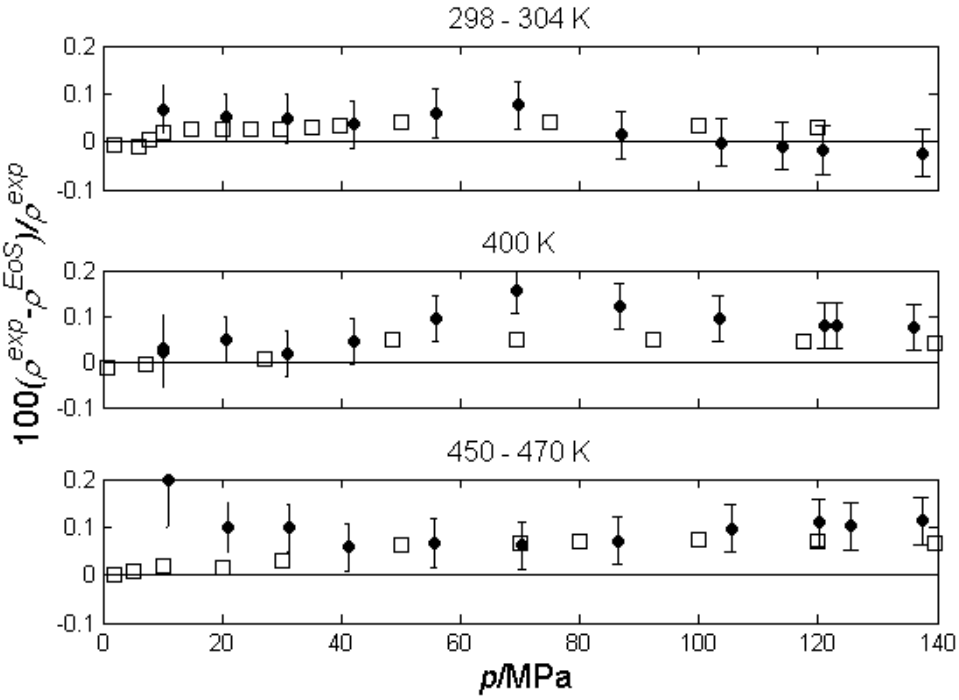

Figure 17. Ethane density measurements for this work ● (304 K, 400 K, 470 K) and Cristancho et al. □ [41] (298 K, 400 K, 450 K)

3.4 Nitrogen and methane mixtures

Nitrogen + methane mixtures were prepared using the mixture apparatus described in section 2. Binary mixtures help when estimating component interactions, for example cross virial coefficients. Eubank and Hall [43] found that the optimal mixture composition to determine those interactions are 0.25 and 0.75. Therefore, this work prepares and performs density measurements for these nominal compositions and an equimolar mixture. Table 3 shows the mass of each substance added to the mixture, the resulting mole fraction values of the mixtures, and the estimated uncertainty in the mixture composition.

Table 3. Methane + nitrogen mixture compositions

Sample	m_{CH4}/g	m_{N2}/g	x_{CH4}	x_{N2}	$U(x)$
25% CH_4 + 75% N_2	540.1	2831	0.24989	0.75011	0.00004
50% CH_4 + 50% N_2	1106.1	1934.9	0.49954	0.50046	0.00003
75% CH_4 + 25% N_2	1734.6	1015.6	0.74889	0.25111	0.00002

Very few accurate p-ρ-T data are available for these mixtures at pressures higher than 40 MPa and temperatures up to 470 K. These new data can improve methane + nitrogen correlations at high pressures. These data complement data from Seitz and Blencoe [29] who performed measurements up to 100 MPa with an uncertainty close to 1 $kg \cdot m^{-3}$.

3.4.1 25% Methane + 75% nitrogen

Table B.6 in appendix B presents the experimental results for 25 % methane + 75 % nitrogen, density values calculated using the GERG-2008 EoS developed by Kunz and Wagner [37], and the relative differences between the experimental and EoS values. Figure 18 shows the relative deviations for 304 K, 350 K, 400 K and 470 K.

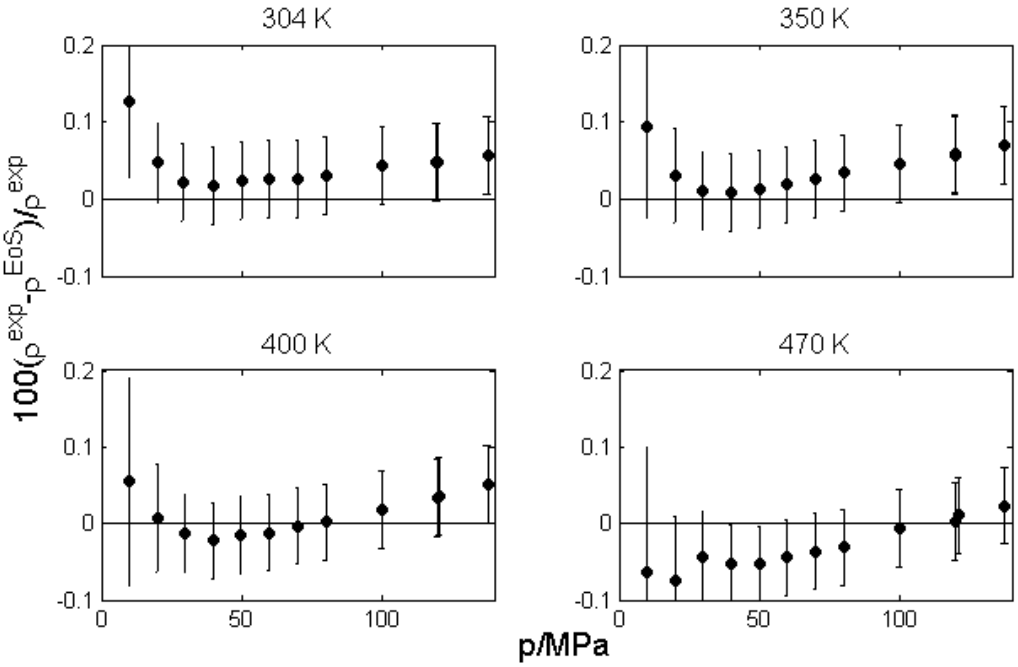

Figure 18. Density measurements for the 25/75 methane + nitrogen sample at 304 K, 350 K, 400 K and 470 K

3.4.2 50 % Methane + 50 % nitrogen

Table B.7 in appendix B contains experimental results for the 50 % methane + 50 % nitrogen mixture, the GERG-2008 densities, and the relative differences between the experimental and EoS values. Figure 19 contains the relative differences as a function of pressure for several temperatures.

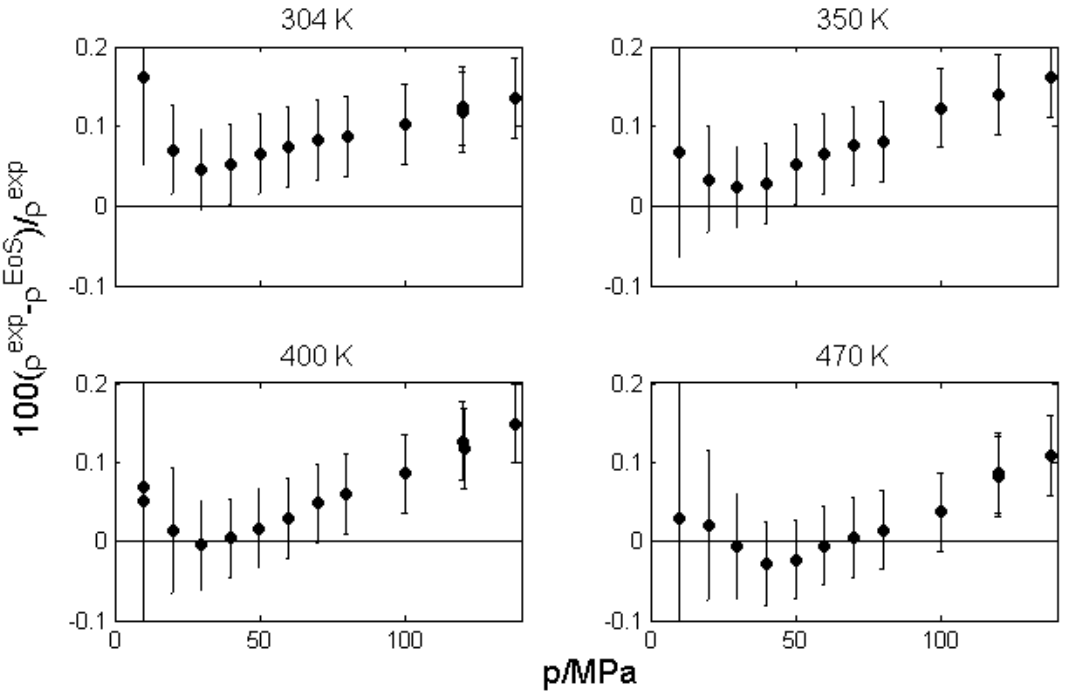

Figure 19. Density measurements for the 50/50 methane + nitrogen sample at 304 K, 350 K, 400 K and 470 K

3.4.3 75% Methane + 25% nitrogen

Finally, Table B.8 in appendix B presents experimental results, EoS values and relative differences for the 75 % methane + 25 % nitrogen mixture. Figure 20 shows the relative differences as a function of pressure for several temperatures.

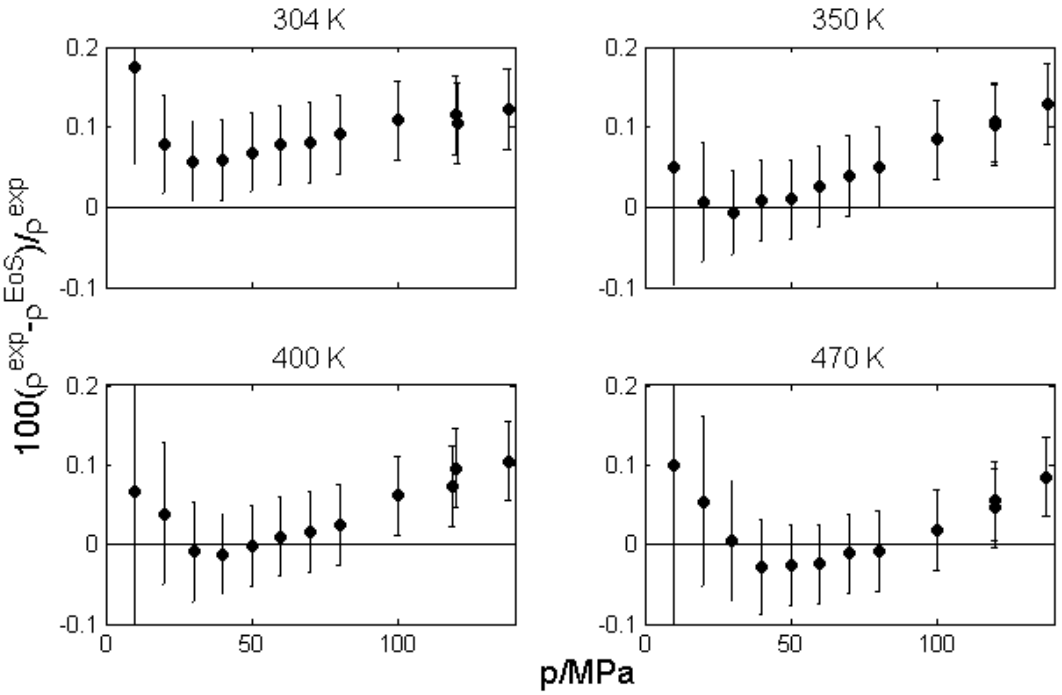

Figure 20. Density measurements for the 75/25 methane + nitrogen sample at 304 K, 350 K, 400 K and 470 K

Figures 18, 19 and 20 demonstrate that relative differences between GERG -2008 EoS [37] and the experimental results vary slightly with composition, but generally are quite small. For pressures below 40 MPa, the EoS describes the experimental results within their experimental uncertainties. The differences increase slightly at higher pressures, however the GERG-2008 EoS describes the experimental result within ±0.15 %.

4. RATIONAL EQUATION OF STATE

Chemical process modeling and design requires accurate models to predict energies, entropies and densities. These models, called Equations of State (EoS), can correlate all thermodynamic properties. Industry uses cubic EoS for many applications because they are simple to use and do not require massive computational capabilities for evaluating properties. However, cubic EoS can have large errors when predicting densities, and often cover limited ranges in pressure and temperature.

In recent years, researchers have suggested EoS based upon Helmholtz energy to describe accurately thermodynamic properties over wide ranges of temperature and pressure, including vapor-liquid equilibrium. These EoS usually express Helmholtz energy as an ideal gas part and residual part. The EoS GERG-2008 [37] defines the residual functional as an empirical combination of exponential terms that are functions of temperature and density, and it produces excellent results over wide ranges of pressure and temperature. However, this approach requires heavy computational capabilities, which increase calculation time for complex systems.

To find a balance between accuracy and computational cost, this work proposes an EoS based upon a rational form of the Helmholtz energy. Hard sphere theory uses a rational form to describe pressure [44] as function of density and temperature. In addition, Kumar and Starling [45] have described a completely general cubic EoS using a rational form. These studies suggest that residual energy could have similar form.

This section presents the development of accurate EoS for nitrogen, argon and methane covering a wide range of temperature and pressures based upon a rational form

of Helmholtz energy. The equation does not include exponential functions, which simplifies calculations and reduces computational time by a factor of 20 compared to GERG-2008.

4.1 Equations of state based in Helmholtz free energy

The Helmholtz energy is a fundamental property and is function of density and temperature as independent variables. The following equation presents Helmholtz energy as a combination of ideal and residual contributions [32].

$$A(T,\rho) = A^{id}(T,\rho) + A^{r}(T,\rho) \quad [47]$$

Equation 47 is transformed to a dimensionless form using reduced properties, where τ is the inverse of reduced temperature and δ is reduced density.

$$\frac{A(T,\rho)}{RT} = \alpha = \alpha^{id}(\tau,\delta) + \alpha^{r}(\tau,\delta) \quad [48]$$

$$\tau = \frac{T_c}{T} \quad [49]$$

$$\delta = \frac{\rho}{\rho_c} \quad [50]$$

Helmholtz energy, as function of density and temperature, can express all thermodynamic properties using its derivatives [35]. Table 4 shows some thermodynamic properties using reduced properties.

Table 4. Thermodynamic properties as function of Helmholtz free energy

Properties	
Pressure	$P = \rho RT\left(1+\delta\alpha_{\delta}^{r}\right)$
Compressibility factor	$Z = 1+\delta\alpha_{\delta}^{r}$
Second virial coefficient	$B = \lim_{\delta\to 0}\alpha_{\delta}^{r}$
Third virial coefficient	$C = \lim_{\delta\to 0}\alpha_{\delta\delta}^{r}$
Isochoric heat capacity	$\frac{C_v}{R} = -\tau^2\left(\alpha_{\tau\tau}^{id}+\alpha_{\tau\tau}^{r}\right)$
Speed of Sound	$\frac{w^2M}{RT} = 1+2\delta\alpha_{\delta}^{r}+\delta^2\alpha_{\delta\delta}^{r}-\frac{\left(1+\delta\alpha_{\delta}^{r}-\delta\tau\alpha_{\delta\tau}^{r}\right)^2}{\tau^2\left(\alpha_{\tau\tau}^{o}+\alpha_{\tau\tau}^{r}\right)}$
Specific Enthalpy	$\frac{h}{RT} = \tau\left(\alpha_{\tau}^{o}+\alpha_{\tau}^{r}\right)+1+\delta\alpha_{\delta}^{r}$

Abbreviations:

$\alpha_{\delta}^{r} = \partial\alpha^{r}/\partial\delta$; $\alpha_{\delta\delta}^{r} = \partial^2\alpha^{r}/\partial\delta^2$; $\alpha_{\tau}^{r} = \partial\alpha^{r}/\partial\tau$; $\alpha_{\tau\tau}^{r} = \partial^2\alpha^{r}/\partial\tau^2$

Ideal contributions of the Helmholtz energy have been described using ideal heat capacities and the ideal gas EoS. However, only an empirical based equation can describe the residual energy. This work uses the definitions for the ideal contributions to the Helmholtz energies for argon, methane and nitrogen published previously [32] [34] [36].

Reference equations of state for methane, argon and nitrogen propose an empirical form for residual terms based upon a combination of polynomial and exponential terms. Setzmann and Wagner [36] [46] and Tegeler [34] discuss some of the strategies for estimating parameters by combining linear and nonlinear techniques. The residual forms include polynomial terms, exponential terms and Gaussian (bell-shaped) terms as functions of reduced density and temperature. The Nitrogen EoS has a bank of 838 terms and the Argon EoS needs 650 terms.

A generalized form of the modern functional for the Helmholtz energy residual is

$$\alpha^r(\tau,\delta) = \sum_k N_k \delta^{i_k} \tau^{j_k} + \sum_k N_k \delta^{i_k} \tau^{j_k} \exp\left(-\delta^{l_k}\right) + \sum_k N_k \delta^{i_k} \tau^{j_k} \exp\left(-f_k (\delta - 1)^2 - b(\tau - 1)^2\right) \quad [51]$$

After optimization, the nitrogen EoS has 36 coefficients plus 12 Gaussian bell-shaped parameters. Argon needs 41 coefficients plus 12 Gaussian bell-shaped coefficients. Also, is noted that density exponents (*i*) are integers but temperature exponents (*j*) may be non-integer numbers.

4.2 Rational function for residual Helmholtz energy

This work suggests a rational form in density as an empirical description of the residual Helmholtz energy. This form is less complex than the modern functional, thus reducing computational costs. Based in the fact that pressure can be described as a rational equation [44], the proposed functional is a ratio of 6th and 3rd order polynomials,

$$\alpha^r = \frac{f}{g} = \frac{\sum_{i=1}^{6} N_i \delta^i}{1+\sum_{i=1}^{3} D_i \delta^i} = \frac{N_1\delta + N_2\delta^2 + N_3\delta^3 + N_4\delta^4 + N_5\delta^5 + N_6\delta^6}{1 + D_1\delta + D_2\delta^2 + D_3\delta^3} \quad [52]$$

The coefficients *N* (Numerator) and *D* (Denominator) are functions of temperature. Isothermal data for nitrogen [47] and argon [48] help identify the mathematical forms of those coefficients as functions of temperature. While the temperature dependence is a work in progress, this work uses 4th order polynomial functions of the inverse reduced temperature (τ) to define *N* and *D* coefficients.

These functions are sufficient for simple systems, but they may fail for more complex systems. Although exponential or non-integer powers might provide proper behavior, they have the undesired effect of increasing computational costs [49].

$$N_i = \sum_{j=0}^{j=4} c_{i,j}\tau^j \quad [53]$$

$$D_i = \sum_{j=0}^{j=4} b_{i,j}\tau^j \quad [54]$$

The parameters *N* and *D*, in equations 53 and 54 are functions only of temperature, which allows representing both the numerator and denominator as simple functions of reduced density at constant temperature. With this in mind, a simple

expression defines the residual Helmholtz derivatives as functions of reduced density (δ) at constant temperature (τ), simplifying evaluation of pressure.

$$\alpha_\delta^r = \frac{f' g - g' f}{g^2} \qquad [55]$$

$$f' = \left(\frac{\partial f}{\partial r}\right)_t = \sum_{i=1}^{6} i N_i \delta^{i-1} \qquad [56]$$

$$g' = \left(\frac{\partial g}{\partial \rho}\right)_\tau = \sum_{i=1}^{6} i D_i \delta^{i-1} \qquad [57]$$

The expression for pressure becomes

$$p = \rho RT\left(1 + \delta\alpha_\delta^r\right) = \rho RT\left(1 + \delta\left(\frac{f' g - g' f}{g^2}\right)\right) \qquad [58]$$

From this equation, it is clear that if the Helmholtz energy is expressed in rational form, the pressure also will have a rational form. For the Helmholtz energy form shown in Equation 52, the pressure effectively is a 10^{th} order polynomial in density so that there are ten density solutions.

At each temperature, the rational equation has a combination of complex and real roots. For temperatures above the critical temperature, eight solutions are complex and two are real. Only one of the real solutions is physically realistic because the other is either negative or greater than seven times the critical density. For temperatures below the critical temperature, the rational equation has four to six real roots with the remainder being complex roots.

For supercritical temperatures, numerical methods, such as those of Newton or Halley, can find density solutions from any initial estimate, so a crude model such as the

ideal gas suffices. Finding proper solutions at subcritical temperatures requires more accurate initial estimates in density, such as those provided cubic equations of state.

The virial equation is a good approximation for high temperature regions. The virial coefficients are related to the residual Helmholtz energy (see Table 2). For the rational form shown in equation 52, the second (B) and third (C) virial coefficients are related to N_1, N_2 and D_1 as shown in Equations 59 and 60.

$$B = \lim_{\delta \to 0} \alpha_{\delta}^{r} = N_1 = \sum_{j=0}^{j=4} c_{1,j} \tau^{j} \qquad [59]$$

$$C = \lim_{\delta \to 0} \alpha_{\delta\delta}^{r} = 2\left(N_2 - N_1 D_1\right) = 2\left(\sum_{j=0}^{j=4} c_{2,j} \tau^{j} - \sum_{j=0}^{j=4} c_{1,j} \tau^{j} \sum_{j=0}^{j=4} b_{1,j} \tau^{j} \right) \qquad [60]$$

Table 4 also shows the relations between the speed of sound, isochoric heat capacity and various derivatives of the residual Helmholtz energy with respect to density (δ) and inverse reduced temperature (τ). Appendix C contains complete expressions for the various first and second order derivatives.

4.3 Fitting procedures

One of the challenges in multi-parametric equations is to determine proper density and temperature functional forms. This work proposes a combination of polynomial and rational functions for describing density. This form does not involve high computational costs because simple operations such as multiplication and summation are sufficient to evaluate polynomial forms. However, the equation form must be capable of modeling real fluid properties.

A generalized rational equation can describe residual Helmholtz energy as a function of density at constant temperature. The *p*-ρ-*T* data of Nowak et al. [47] for nitrogen present density organized as isotherms, which is convenient for evaluating different mathematical forms. These data allow optimizing coefficients based upon density at constant temperature. The Nowak isotherms for nitrogen cover the critical, supercritical, and subcritical vapor-liquid regions.

A nonlinear least-squares solver function can evaluate different rational equation forms using isothermal data. This routine uses a Levenberg-Marquardt algorithm which is part of a commercial software package (MATLAB, the MathWork inc). This algorithm can solve nonlinear least squares problems, such as those related to curve fits, but the routine does not necessarily find a global minimum. The procedure needs good initial coefficient values to describe real fluid behavior correctly. The rational equation offers advantages for finding appropriate initial values. For example, first numerator coefficient (N_1) equals the second virial coefficient, which Nowak reports at different temperatures. Additionally, N_1, N_2 and D_1 comprise the third virial coefficient making easier to add constraints for preliminary calculations.

According to Kozoil [50], quintic equations in pressure can describe pure fluid properties with a reasonable accuracy. The current work first tested a residual Helmholtz functional with 3rd order in numerator and 1st order in denominator, which generates a quintic function in pressure.

$$\alpha^r = \frac{N_1\delta + N_2\delta^2 + N_3\delta^3}{1 + D_1\delta} \qquad [61]$$

Fitting parameters with the nonlinear least-squares fitting routine, equation 63 provides excellent results for nitrogen isotherms at high temperature (reduced temperatures greater than 1.3). However, density deviations are higher than desired for the critical region and liquid densities. This indicates that a higher order equation is necessary for describing pure fluids correctly. However, more parameters imply more degrees of freedom and higher probability of finding solutions with local minima.

The first and second derivatives of pressure as a function of density at the critical temperature equal zero. These critical point constraints are useful when developing EoS. For the critical isotherm of nitrogen at 126.192 K, Nowak, et al. report 35 density measurements at different pressures.

Eubank and Hall proposed a mathematical methodology to apply critical point constraints [51] which is useful with rational equations. Equation 62 shows the Eubank and Hall approach. In this method, *f* and *g* represent numerator and denominator for an equation explicit in pressure. However, high order density polynomial functions are difficult to solve and a numerical approach is more convenient.

$$\frac{P_c}{RT_c} = \frac{f}{g} = \frac{f'}{g'} = \frac{f''}{g''} \qquad [62]$$

The critical constraints are related to the residual Helmholtz energy and its derivatives with respect to density by

$$\left(\frac{\delta p}{\delta \rho}\right)_T = RT\left[1 + 2\delta\alpha_\delta^r + \delta^2\alpha_{\delta\delta}^r\right] \text{ so, at critical point (CP), } \left[1 + 2\alpha_\delta^r + \alpha_{\delta\delta}^r\right] = 0 \qquad [63]$$

$$\left(\frac{\delta^2 p}{\delta \rho^2}\right)_T = \frac{RT}{\rho}\left[2\delta\alpha_\delta^r + 4\delta^2\alpha_{\delta\delta}^r + \delta^3\alpha_{\delta\delta\delta}^r\right] \text{ so, at CP, } \left[2\alpha_\delta^r + 4\alpha_{\delta\delta}^r + \alpha_{\delta\delta\delta}^r\right] = 0 \qquad [64]$$

Critical constraints reduce the degrees of freedom in the nonlinear optimization problem, and critical isotherm data reveal the order required for the rational equation. This work finds that a rational equation with 6^{th} order in the numerator and 3^{rd} order in the denominator works well with the critical isotherm data.

In total, the rational equation has 9 density coefficients (6 in the numerator and 3 in the denominator), which are functions of temperature. Equation 61 describes densities at high temperatures accurately, indicating that some of the coefficients go to zero with increasing temperature. For reduced temperatures higher than 1.3, N_4, N_5, N_6, D_2 and D_3 should have negligible values. Using isothermal data for other temperatures, the mathematical form reveals values for each coefficient at different temperatures. Coefficient values calculated for each temperature provide initial values for a global optimization.

A modified version of the same computational routine provides the nonlinear least squares global optimization for the Nowak et al. data set using a 6- over 3-degree rational equation form. Polynomial functions in temperature with integer exponents describe the behavior of coefficients for rational equations when applied to simple systems. Exponential and non-integer power functions can have similar results, but polynomial functions have significantly lower computational cost [49].

A preliminary calculation using the nonlinear least square fitting routine describes the Nowak et al. data within acceptable deviations. These results offer good initial values for further global optimizations. Observations show that nitrogen and argon

coefficients demonstrate similar behavior, making it possible to use the same initial values for an argon global optimization.

This rational equation of state must describe thermodynamic properties of fluids over wide ranges of pressure and temperature. With this in mind, this work performed a global optimization, including *p*-ρ-*T* data sets covering the subcritical, critical and supercritical regions. This global optimization, based upon the Levenberg-Marquardt algorithm, includes statistical weights that are inversely proportional to reported uncertainties. EoS for nitrogen, argon and methane use a similar procedure.

Pure fluids are complex in nature, especially in the vapor + liquid two phase region. The global routine requires complementary thermodynamic properties such as vapor pressure, and saturated liquid and vapor densities having different weights in the global function.

The rectilinear diameter constraint and Maxwell equal area rule create a better representation for vapor liquid equilibrium. The equal area rule:

$$P_v\left(V_G - V_L\right) = \int_{V_L}^{V_G} P dV \qquad [65]$$

when applied to the residual Helmholtz energy and its derivatives, becomes

$$RT * \left(\ln\left(\frac{\delta_L}{\delta_v}\right) + \alpha^r\left(\delta_L\right) - \alpha^r\left(\delta_v\right) \right) - \frac{P_v}{\rho_c}\left(\frac{1}{\delta_v} - \frac{1}{\delta_L}\right) = 0 \qquad [66]$$

Equations of state with multiple parameters may have multiple local minima, which can lead to misinterpretations of the real pure fluid behavior. Isochoric heat

capacities and speed of sound data sets can complement the analysis. These properties include first and second derivatives in density and temperature.

Speeds of sound and isochoric heat capacities are function of residual Helmholtz energy and its derivatives. The nonlinear optimization routine includes multiple data sets from different authors using weights inversely proportional to the data uncertainties.

In summary, the nonlinear least squares weighted optimization routine uses a Levenberg-Marquardt algorithm and includes p-ρ-T data, vapor pressure data, saturated densities, isochoric heat capacities, speeds of sound and applicable constraints. Weights vary for each property and data set to incorporate the experimental uncertainties into the fits. This methodology produces excellent results for all properties in all regions except for the subcritical liquid data. In the liquid region, the derivative of pressure as a function of density at constant temperature $(\partial p/\partial \rho)_T$ is large. Thus, small errors in density produce large errors in pressure. A different approach is necessary to find a final solution.

A common least square fitting routine takes temperature and density as fixed values. However, temperature and density measurements have errors that are relevant in the liquid region. Orthogonal distance regression is a methodology that includes errors in all variables. ODRPACK is a software package for weighted orthogonal distance regression to find the parameters that minimize the sum of squares for weighted sets of observations to determine coefficients [52]. Using this package, this work calculates EoS parameters using errors for temperature, density and pressure reported by different authors. Using parameter values from Levenberg-Marquardt algorithm as initial

estimates, ODRPACK calculates the final coefficients describing all data within the experimental pressure, temperature and density uncertainties.

Table 5 presents the parameters for rational equations of state for nitrogen, argon and methane. The coefficients describe p-ρ-T data, isochoric heat capacities, speeds of sound and saturation properties within the uncertainty reported by authors. Table 5 presents the coefficients for equation 52. The first column shows the powers applied to inverse reduced temperature in equation 53 and 54. The following sections show all data sets used in the nitrogen, argon and methane EoS. Also, it presents deviation plots and discussion of results for these three pure fluids.

Table 5. Coefficients for Rational equations of nitrogen, argon and methane

N_1	**Nitrogen**	**Argon**	**Methane**
0	0.440921454	0.416925175	0.40999340
1	-0.744789222	-0.783555867	-0.63513418
2	-1.186842847	-1.056851105	-1.45361301
3	0.501561416	0.383270348	0.74668505
4	-0.161989909	-0.122881189	-0.25449607

N_2	**Nitrogen**	**Argon**	**Methane**
0	-0.478688238	-0.550946744	-0.96102278
1	2.509959515	6.136062868	3.91649965
2	-3.293978926	-17.05656731	-1.75703187
3	0.677067618	14.11092015	-5.55471736
4	1.929315252	-1.34847563	5.29692590

N_3	**Nitrogen**	**Argon**	**Methane**
0	0.06913669	0.447604333	0.04921353
1	-0.015026845	-3.346381066	0.40266297
2	-1.234382041	8.640473334	-4.51527044
3	2.497264781	-5.916462755	9.66619191
4	-2.211216163	-0.797338531	-6.38107962

Table 5. Continued

N_4	**Nitrogen**	**Argon**	**Methane**
0	0.068290145	-0.07998447	-0.06436001
1	-0.458361383	0.500984381	-0.05313680
2	1.445287769	-0.905016697	1.96621840
3	-1.849957326	-0.484697165	-4.60805740
4	1.063039841	1.302235057	3.08211809

N_5	**Nitrogen**	**Argon**	**Methane**
0	-0.011610772	0.014143604	0.05780445
1	0.122702717	-0.00889715	-0.24369838
2	-0.419616359	-0.121084387	-0.05748681
3	0.514956099	0.454949814	1.11027044
4	-0.278322011	-0.448908692	-1.01694825

N_6	**Nitrogen**	**Argon**	**Methane**
0	0.001026553	-0.004936928	-0.00550612
1	-0.006090794	0.012028566	0.03763616
2	0.038933966	0.005182345	-0.03698095
3	-0.049327864	-0.037524696	-0.09146431
4	0.028851902	0.046462564	0.12798097

D_1	**Nitrogen**	**Argon**	**Methane**
0	-1.271672005	-1.096702216	-2.45928402
1	3.41175686	8.813455461	5.20393643
2	-3.136492165	-11.73014881	-2.19477173
3	0.110410272	3.505391751	-0.89243617
4	-0.080370166	-0.371129385	-0.18450084

D_2	**Nitrogen**	**Argon**	**Methane**
0	0.549880908	0.96759586	0.55754001
1	-1.31589903	-5.573183035	-0.95673580
2	1.259980385	7.264618787	-0.34382404
3	-0.000809216	-2.395347432	0.99182581
4	0.046305301	0.282094862	0.10712970

D_3	**Nitrogen**	**Argon**	**Methane**
0	-0.033526391	-0.198152731	0.02738641
1	0.127632131	0.974840143	-0.15828509
2	-0.14371306	-1.189500448	0.17423043
3	0.010842503	0.442589979	0.01938048
4	-0.006815818	-0.054507197	-0.02223127

4.4 Equation of state for nitrogen

Nitrogen is one of the most important components in process modeling, where it often finds use as a calibration or reference fluid. Several authors have estimated its thermodynamics using various methodologies. Table 6 presents the triple point and critical point values for nitrogen reported in the GERG reference EoS [32]. The current work uses density (p-ρ-T), vapor pressure, isochoric heat capacity and speed of sound data and estimates empirical coefficient values for a rational residual Helmholtz energy function.

Table 6. Physical properties of nitrogen

	T/K	p/kPa	ρ/ kg·m^{-3}
Triple Point	63.151± 0.003	12.523±0.010	
Critical Point	126.192±0.010	3395.800±1.700	313.3±0.4

4.4.1 Data sets

Many experimental studies of widely varying accuracy have been reported for nitrogen. While developing the reference equation for nitrogen, Span et al. [32] performed an extensive review of the accuracy of the experimental data. Their work provides the basis for selecting the best data sets to use for developing the rational EoS. Table 7 provides a listing of the data sets used in this work and some general information about each.

4.4.1.1 *p-ρ-T*

Density is one of the most widely studied properties for nitrogen. Several data sets are available covering wide ranges of temperatures and pressures. The selected sets are accurate density data spanning a wide range of temperatures and pressures that demonstrate the capabilities of the rational equation in describing pure fluids.

Nowak et al. [47] have published density measurements using a "two-sinker densimeter" with an overall uncertainty between ± 0.010–0.015 % in density for temperatures from 66 K to 340 K and pressures up to 12 MPa. The data cover the critical region, slightly super critical data and subcritical isotherms. Klimeck et al. [53] in 1998 used a "single sinker densimeter" to increasing the pressure range up to 30 MPa and the temperature range to 520 K with uncertainties up to ±0.012 % in density.

Straty et al. [54] present density measurements from 80 K to 300 K with pressures up to 34.8 MPa. These data extend the pressure range for subcritical temperatures. Finally, Robertson et al. [55] report data covering pressures up to 1000 MPa with estimated uncertainties of ±0.3 %. These data improve the extrapolation behavior and density estimation at high pressures. Table 7 summarizes the density data sets and contains uncertainties.

4.4.1.2 Vapor pressure

Vapor pressure data complement density measurements, for EoS development. The fitting procedure requires vapor pressures, along with saturated vapor and liquid densities to apply the Maxwell equal rule constraints. Nowak et al. [56] presents vapor pressure data from 66 K up to the critical point. For subcritical temperatures the

uncertainty is ±0.01 %, but near the critical temperature and pressure the uncertainty increases rapidly. Exclusion of some of these points avoids misinterpretation and inconsistency using the most accurate data.

4.4.1.3 Virial coefficients

Virial coefficients are not included in fitting routines, but they evaluate coefficients behavior in the EoS. Nowak et al. [47] provides virial coefficients from 98 K to 340 K. Low temperature values have higher uncertainties, especially for third virial coefficients. Table 7 presents details about these data.

4.4.1.4 Speed of sound

Speed of sound and isochoric heat capacity measurements complement information provided by density data. When fitting an empirical function describing residual Helmholtz energy, local minima in the objective can occur with incorrect coefficient values. Speed of sound is a good tool for evaluating and finding a proper minimum, because it includes second derivatives in density, temperature and cross terms. This work uses 6 data sets covering temperatures from 80 K to 350 K with pressures up to 30 MPa. Costa-Gomes and Trusler [57] and Ewing [58] present accurate measurements within uncertainties from ±0.001 % up to ±0.010 %. Table 7 presents speed of sound data used in this work.

4.4.1.5 Isochoric heat capacity

Isochoric heat capacity contains the second derivative in temperature of the residual Helmholtz energy. An accurate description of this thermodynamic property indicates an appropriate temperature function. The best calorimetric measurements have

uncertainties ranging from ±0.5 to 2 %. Such large errors in the experimental measurements present a challenge when assigning overall uncertainties.

Table 7. Summary of selected *p*-*ρ*-*T*, vapor pressure, second and third virial, speed of sound and isochoric heat capacities experimental data used to develop the rational EoS for nitrogen

Density						
Source	**Year**	T /K	p /MPa	ΔT /mK	$\Delta p/p$ (%)	$\Delta \rho/\rho$ (%)
Robertson et al. [55]	1969	308 – 573	164 – 1011			
Straty et al. [54]	1980	80 – 300	0.83 – 34.8			
Nowak et al. [47]	1997	66 – 340	0.10 – 12.0	1.5 – 3	greater of 0.04	0.01 – 0.015
Klimeck et al. [53]	1998	240 – 520	1.11 – 30.1	4 – 10	0.006	0.012
Vapor Pressure						
Source	**Year**	T /K	p /MPa	ΔT /mK	$\Delta p/p$ (%)	$\Delta \rho/\rho$ (%)
Nowak et al. [56]	1997	66 – 125		1.5 – 3		0.01 – 0.015
Second Virial Coefficient						
Source	**Year**	T /K	p /MPa		ΔB /cm^3·mol^{-1}	
Nowak et al. [47]	1997	98 – 340			0.25 – 0.80	
Third Virial Coefficient						
Source	**Year**	T /K	p /MPa		ΔC /cm^6·mol^{-2}	
Nowak et al. [47]	1997	98 – 340			100 – 800	
Speed of Sound						
Source	**Year**	T /K	p /MPa	ΔT /mK	$\Delta p/p$ (%)	$\Delta w/w$ (%)
Boyes [59]	1992	250 – 325	0.05 – 6.64			0.73
El – Hakeem [60]	1965	273 – 294	0.10 – 7.09			
Lestz [61]	1963	273 – 304	0.10 – 1.21			
Costa Gomes [57]	1998	250 – 350	0.10 – 30.1	3	4 kPa	0.001 – 0.01
Ewing [58]	1992	80 – 373	0.00 – 0.58	3	0.02	0.001
Younglove [62]	1980	80 – 350	0.03 – 1.51			

Table 7. Continued

Isochoric Heat Capacity						
Source	**Year**	T /K	ρ /mol·dm^{-3}	ΔT /mK	$\Delta p/p$ (%)	$\Delta C_v/C_v$ (%)
Benedict [63]	1937	303	20.3 – 34.7			
Magee [64]	1991	66 – 307	6.09 – 31.0	30	0.2	0.5 – 2
Weber [65]	1981	91 – 242	10.7 – 27.5			

4.4.2 Nitrogen results

The rational equation of state describes density measurements within their uncertainties in all regions except near the critical point. For the Nowak et al. [47] [56] and Klimeck et al. [53] data, the equation has errors of ±0.01 % for temperatures below 110 K and for vapor phase densities. Liquid densities have similar errors, however the steep slope of liquid isotherms can generate ambiguities when estimating pressure based upon density and temperature measurements. In the region near the critical point, deviation errors increase up to ±0.04 % in density and ±0.2 % in pressure. For temperatures higher than 150 K, deviations are ±0.01 % or lower. Figure 21 presents results for these data.

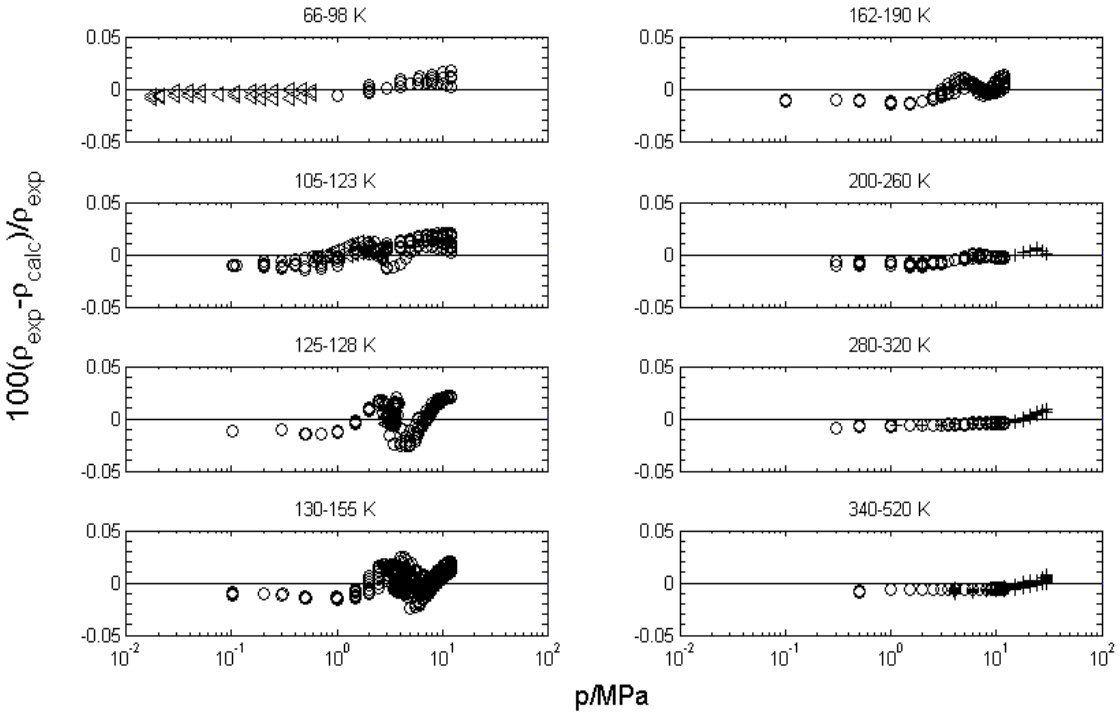

Figure 21. Relative deviations of *p-ρ-T* nitrogen data from Nowak and Klimeck

The Straty et al. [54] and Robertson et al. [55] data cover a wide pressure range. The highest deviation for the Straty data is ±0.05 %, which agrees with the uncertainty in density. For the Robertson data, deviations rise to ±0.07 % in density at high pressures. High-pressure data can improve extrapolation behavior. Figure 22 presents the deviations of the rational equation at different pressures and temperatures.

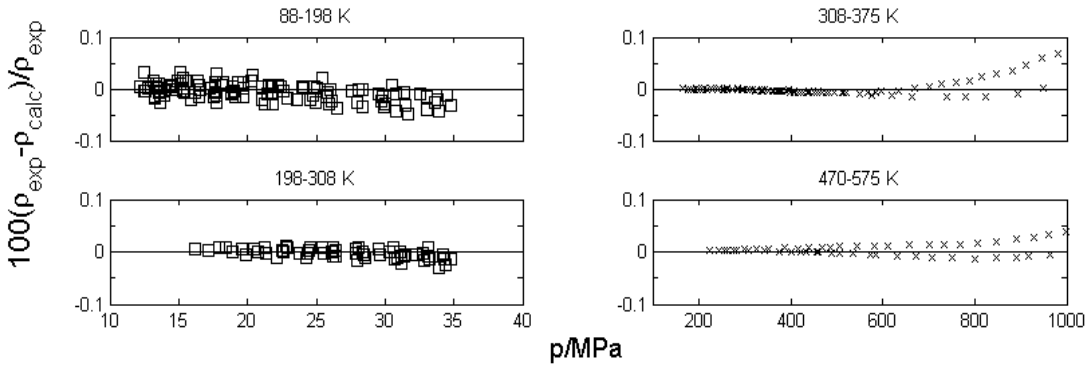

Figure 22. Relative deviations of Rational Equation of State from the p-ρ-T nitrogen data of Straty and Robertson

Industrial applications require accurate EoS. The Rational EOS (REOS) reproduces vapor and liquid saturated densities from Nowak et al. [56] within the uncertainties of the experimental data. Liquid densities must include the effects of uncertainties in pressure. The REOS describes vapor pressures within the experimental uncertainties everywhere except near the critical point where deviations rise to ±0.04 %, which is greater than the uncertainty reported by Nowak. At temperatures below 80 K, vapor pressure errors have larger relative uncertainties because the pressures are very low.

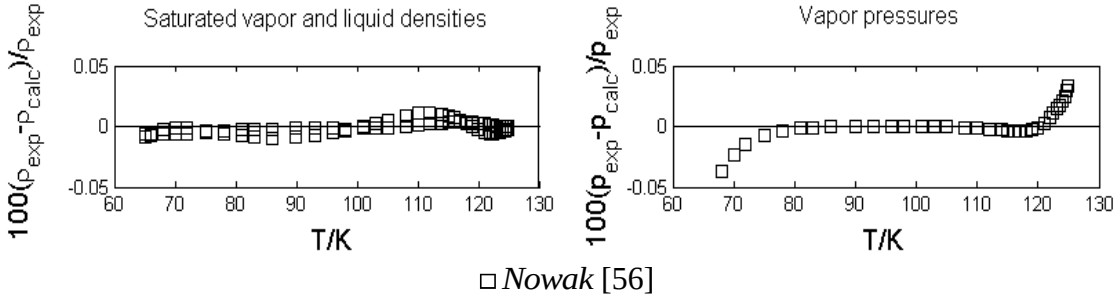

Figure 23. Relative deviations of saturated liquid and vapor densities (left), and vapor pressure (Right) for Nowak

The REOS describes second virial coefficients reported by Nowak [47] properly with absolute residuals smaller than errors claimed by the author. However, the temperature has a limited range, and the REOS might have larger errors at higher and/or lower temperatures. The REOS also predicts third virial coefficients within their estimated errors. At lower temperatures, the values increase in error, however the REOS has proper theoretical behavior with values tending toward zero at high temperatures and toward minus infinity at low temperatures. Because the parameter estimation does not use virial coefficients as input data, they provide an independent test of the REOS behavior. Figure 24 shows that the global optimization produces a good representation of the virial coefficients.

Many speed of sound data sets exist in the literature. The REOS estimates selected data sets within ±0.1 % relative error. These data cover from 80 K to 380 K up to 30 MPa. Costa Gomes and Trusler [57] and Ewing and Trusler [58] claim uncertainties lower than 0.01 %. The REOS reproduces those data within ±0.05 %. This indicates that a rational form in density can describe thermodynamic properties that require second derivatives in density, as shown in figure 25.

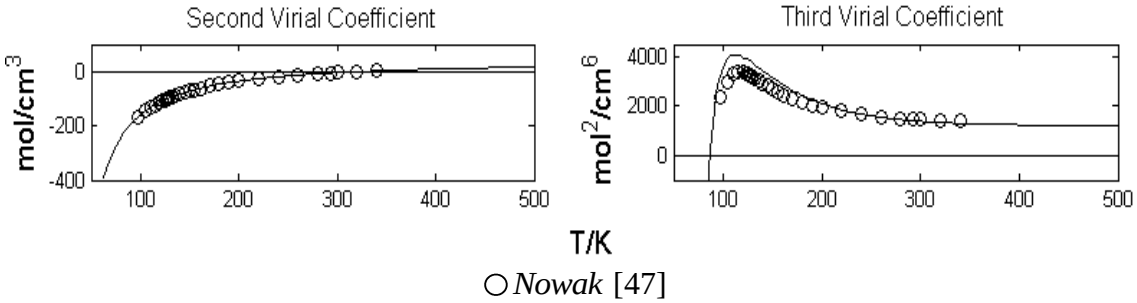

Figure 24. Second virial coefficient (left) and third virial coefficient (right) from Nowak et al. [47]

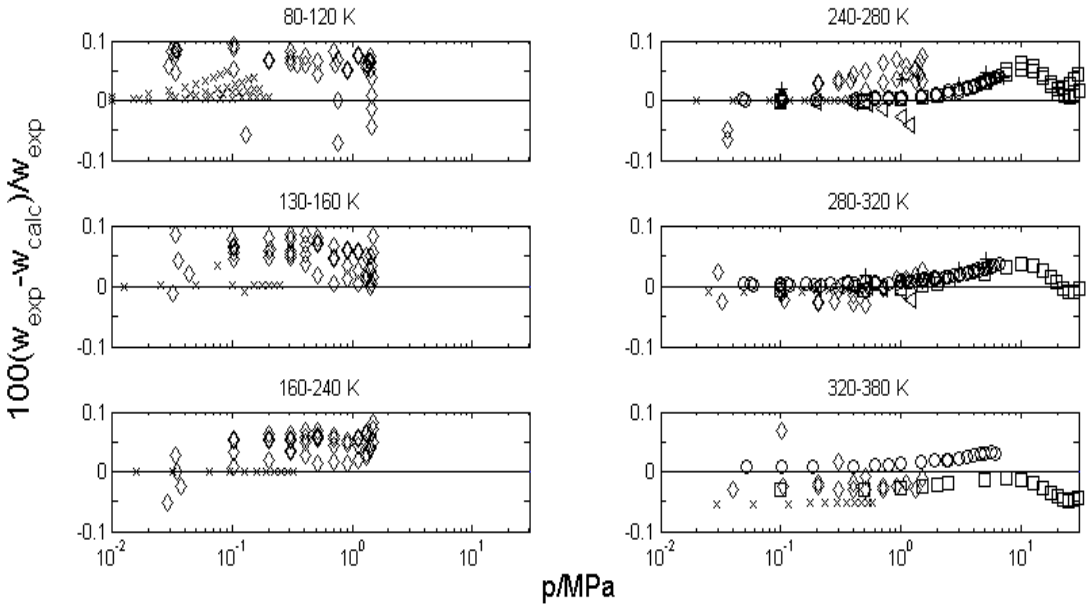

○ *Boyes* [59] □ *Costa Gomes and Trusler* [57]

\+ *El – Hakeem* [60] × *Ewing and Trusler* [58]

◁ *Lestz* [61] ◊ *Younglove and McCarty* [62]

Figure 25. Percent deviation of speed of sound for nitrogen calculated with the REOS

There are few isochoric heat capacity data sets with low uncertainties. The REOS describes three independent data sets covering 66 K to 300 K up to 35 mol·dm^{-3}. Figure 26 demonstrates that the REOS describes these data within ±2 %.

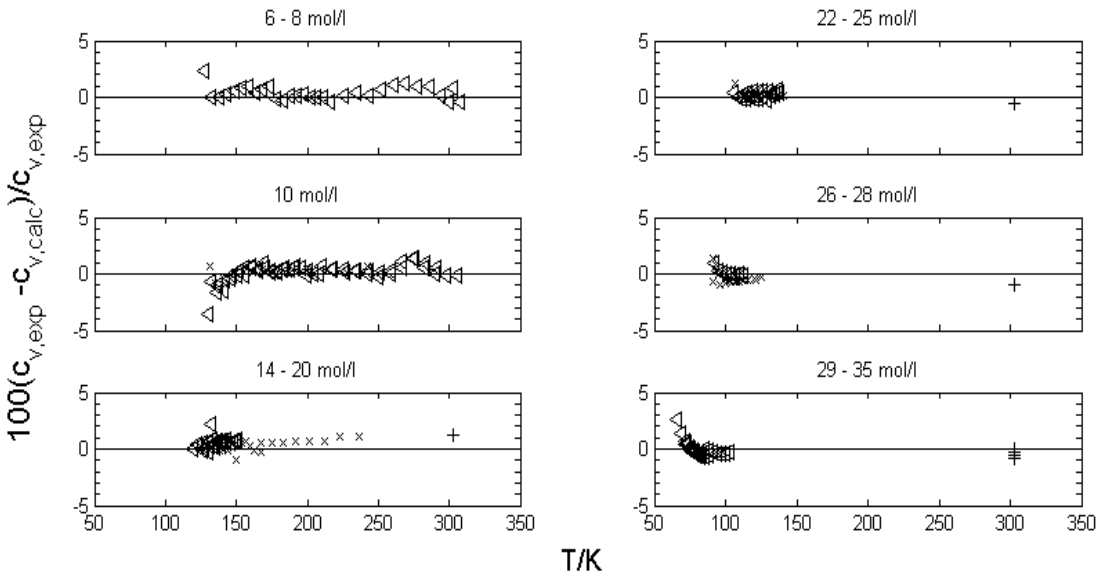

Figure 26. Relative error of isochoric heat capacities from REOS

4.4.2.1 Extrapolation behavior

Evaluation of EoS requires different approaches and methods. There are certain parameters that help to identify problems or prove proper behavior. Particularly, this analysis helps with high pressure and high temperature tendencies. The four properties used to assess equations are the ideal compression factor, Joule Inversion, Boyle and Joule-Thomson inversion curves. Table 8 shows definition of these parameters.

Figure 27 presents the locus of the parameters as a function of reduced temperature and pressure calculated using the REOS for nitrogen. These curves have reasonable shape, and they do not oscillate within the range of the data. Span et al. [32] present the same curves with a similar shape and values. This indicates that the REOS can describe thermodynamic properties in real pure fluids.

Table 8. Ideal curves definition

Curve Name	
Ideal	$Z = 1$
Boyle	$\left(\frac{\delta Z}{\delta p}\right)_T = 0$
Joule – Thomson Inversion	$\left(\frac{\delta Z}{\delta T}\right)_p = 0$
Joule Inversion	$\left(\frac{\delta Z}{\delta p}\right)_\rho = 0$

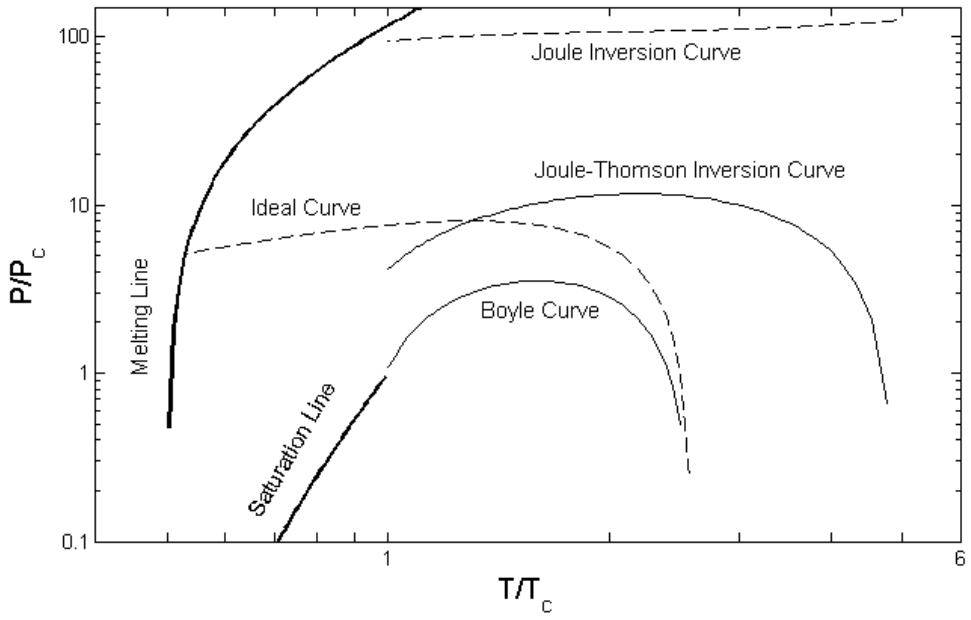

Figure 27. Characteristic curves calculated from rational equation of state

4.5 Equation of state for argon

Argon has industrial and scientific importance. Theoretically, its molecular simplicity is attractive because it is a monoatomic, nonpolar and spherical molecule with an acentric factor of zero. Argon can be a reference or calibration fluid. Table 9 contains some of its physical properties.

Table 9. Physical properties of argon

	T /K	p /kPa	ρ/kg·m^{-3}
Triple Point	83.8058	68.891±0.002	
Critical Point	150.687±0.015	4863.000±3.000	535.6±1.0

4.5.1 Data sets

Many experimental studies of widely varying accuracy have been reported for argon. While developing the reference equation for argon, Tegeler et al. [34] performed an extensive review of the accuracy of the experimental data. Their work provides the basis for selecting the best data sets to use for developing the rational EoS. Table 10 provides a listing of the data sets used in this work and some general information about each.

4.5.1.1 *p-ρ-T*

This paper uses three accurate *p-ρ-T* data sets for argon. Gilgen et al. [48] present data with an uncertainty of ±0.02 % in density for temperatures from 90 to 340 K and pressures up to 12 MPa with slightly higher uncertainties in the critical region. Klimeck

et al. [53] extend the pressure range up to 30 MPa with similar accuracy for temperatures between 235 K and 520 K. The third set of data, Robertson et al. [66], extends the pressure range up to 1000 MPa, but is of lower accuracy.

4.5.1.2 Vapor pressure

Vapor pressures and saturation densities improve behavior at the vapor-liquid equilibrium boundary. Gilgen et al. [67] complements his work by reporting vapor pressures and saturated liquid and vapor densities for temperatures between 110 K and 148 K. The data have an average uncertainty of ±0.017 % up to 148 K. Values closer to the critical temperature have higher uncertainties and are not included in global fitting.

4.5.1.3 Virial coefficients

Gilgen et al. [67] presents values for second and third virial coefficients. Once again, note that these virial coefficients do not apply to optimization. For second virial coefficients, the range of temperatures is from 110 K to 340 K while the third virial coefficients range from 130 to 340 K.

4.5.1.4 Speed of sound

Many speed of sound data are available with a variety of uncertainties. This work uses 12 different data sets to include wide ranges in pressure and temperature while avoiding confusion caused by uncertainties. The overall range in temperature is from 90 to 470 K at pressures up to 800 MPa. Speeds of sound data have a wide range of uncertainties, from as low as ±0.01 % up to ±1 %. Estrada & Trusler [68] and Ewing & Trusler [58] report accurate data with a claimed maximum error of ±0.03 %.

4.5.1.5 Isochoric heat capacities

Some isochoric heat capacities data sets have uncertainties up to ±4 %. The temperature ranges from 87 K to 263 K with densities up to 1393 mol·dm^{-3}.

Table 10. Summary of selected *p*-*ρ*-*T* experimental data for argon

Density						
Source	**Year**	T /K	p /MPa	ΔT /mK	$\Delta p/p$ (%)	$\Delta \rho/\rho$ (%
Robertson et al. [66]	1969	308 – 673	120 – 1050	300	0.1	0.4
Gilgen et al. [48]	1997	90 – 340	0.2 – 12.1	1.5 – 3	0.006	0.020
Klimeck et al. [53]	1998	235 – 520	2.0 – 30.1	10 – 16	0.006	0.02
Vapor Pressure						
Source	**Year**	T /K	p /MPa	ΔT /mK	$\Delta p/p$ (%)	$\Delta \rho/\rho$ (%
Gilgen et al. [67]	1994	90 – 148		3	0.006	0.017
Second Virial						
Source	**Year**	T /K	p /MPa		ΔB /cm^3·mol^{-1}	
Gilgen et al. [48]	1994	110 – 340			0.25 – 1.30	
Third Virial						
Source	**Year**	T /K	p /MPa/		ΔC /cm^6·mol^{-2}	
Gilgen et al. [48]	1994	130 – 340			60 – 120	

Table 10. Continued

Speed of Sound

Source	Year	T /K	p /MPa	ΔT /mK	$\Delta p/p$ (%)	$\Delta w/w$ (%)
Beckermann	1993	250 – 350	0.5 – 1.0			
Boyes [59]	1992	252 – 350	0.05 – 10			0.015
Carome et al. [69]	1968	90.3 – 140	0.5 – 11			
Estrada & Trusler [68]	1995	110 – 450	0.01 – 19			0.03
Ewing & Trusler [58]	1992	90.1 – 373	0.01 – 0.6			0.003
Hurly [70]	2003	293.15 – 373.15	1.5 – 3.3			
Kachanov [71]	1983	373 – 423	100 – 800			1
Lacam [72]	1956	298 – 473	5.1 – 111			
Sharif [73]	1989	273.15 – 298.15	1 – 32.4			
Streett [74]	1974	90.1 – 160	0.1 – 345			0.5
Thoen [75]	1969	100 – 150	0.8 – 52			0.6
Van Itterbeek [76] [77]	1961	84.8 – 300	0.5 – 20			

Isochoric Heat Capacity

Source	Year	T /K	ρ /mol·dm^{-3}	ΔT /mK	$\Delta p/p$ (%)	$\Delta C_v/C_v$ (%)
Anisimov [78]	1975	151 – 263	295 – 693			3
Gladun [79]	1971	87.8 – 151	738 – 1393			4

4.5.2 Argon results

The REOS describes p-ρ-T data within the claimed uncertainties except in the critical region. At temperatures lower than 120 K, the densities have ±0.015 % average deviation. Errors increase near the critical isotherm from 135 to 150 K with a maximum deviation of ±0.04 % in temperature and ±0.1 % in pressure. The Gilgen data [48] at

temperatures higher than 200 K have average deviations less than ±0.01 %. The REOS also reproduces Klimeck [53] densities within ±0.01 % up to pressures of 30 MPa. Figure 28 presents the Gilgen [48] and Klimeck [53] data organized by temperatures showing relative differences between experimental values and the REOS.

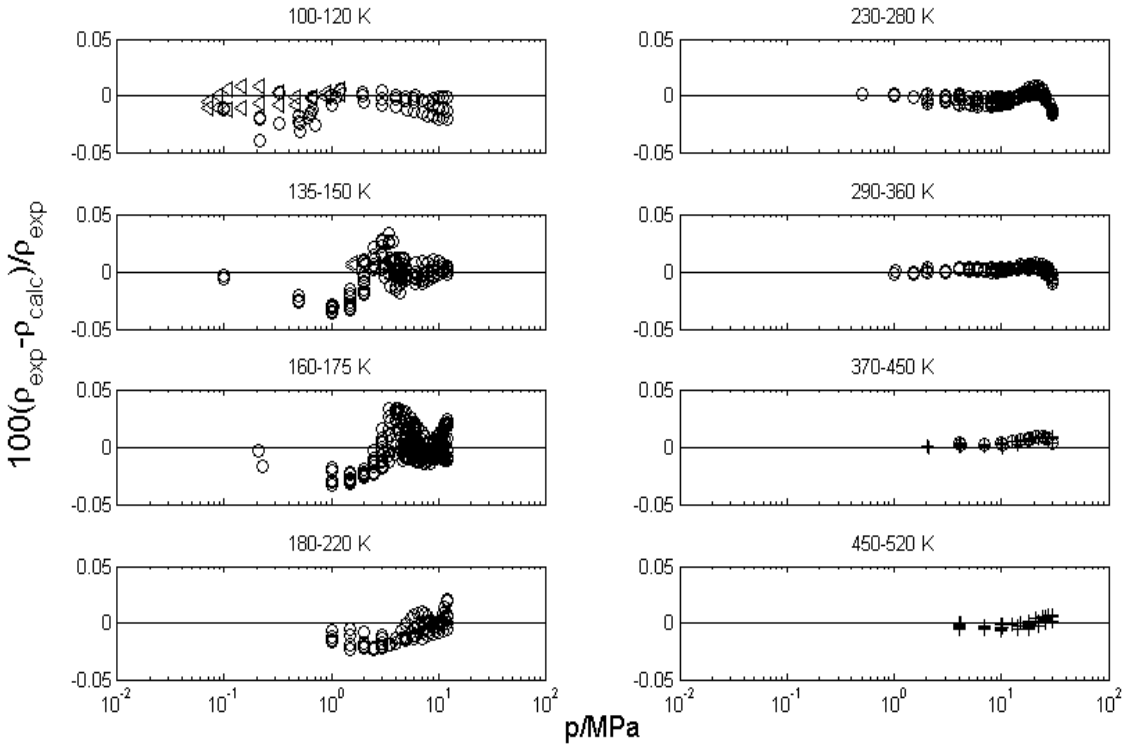

Figure 28. Comparison of *p-ρ-T* Argon data sets from Gilgen and Klimeck and rational equation of state

The Robertson data demonstrate that the REOS behaves properly at pressures up to 1000 MPa. The equation reproduces densities within their uncertainties having maximum error values of ±0.6 %. Figure 29 presents density deviation as a function of

pressure for temperatures ranging from 308 K to 673 K. Errors increase at high pressures values, which reflects experimental inaccuracies.

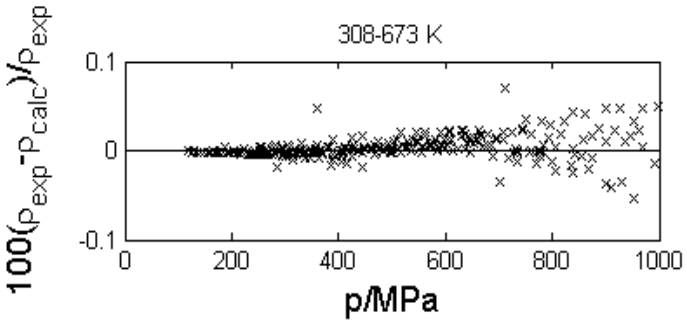

×*Robertson et al* [66]

Figure 29. Relative deviations of rational equation of state from Robertson et al. high-pressure data

The argon REOS describes saturation liquid and vapor densities within ±0.01 % from 90 K to 148K. These errors are within the experimental uncertainties for vapor pressures. The errors increase near the critical point, but the deviations are not more than ±0.03 %. Figure 30 presents saturated densities and vapor pressures from Gilgen et al [67].

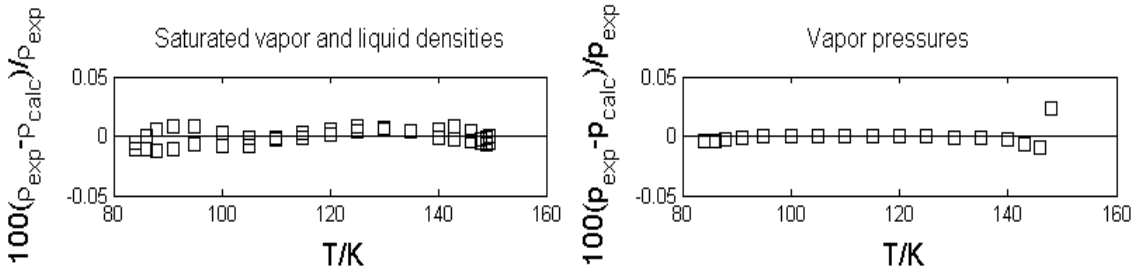

Gilgen et al [67]

Figure 30. Relative deviations for saturated vapor and liquid densities (left) and vapor pressure (right)

Speed of sound requires first and second derivatives of residual Helmholtz energy as function of temperature and density. These data can detect improper fitting parameters in the EoS caused by local minima. The REOS describes 12 speed of sound data sets within ±1 %. In some cases, errors from this EoS are higher than the uncertainties claimed by the authors. However, no evidence of a systematic error as a function of pressure is apparent. Also, the REOS describes the Estrada & Trusler [68]data within ±0.2 % and the Ewing and Trusler [58] data within ±0.08 % at the 95% confident level. Figure 31 compares speeds of sound experimental values to the REOS.

Figure 32 compares isochoric heat capacity data to the REOS calculations. This describes 95 % of the values within ±5 %. However, the discrepancy is greater at the critical temperature. Also, all experimental error values have a displacement from 0, which indicates a bias error of 2 %, but well within the experimental uncertainty. New experimental data of higher accuracy would be most useful for EoS development.

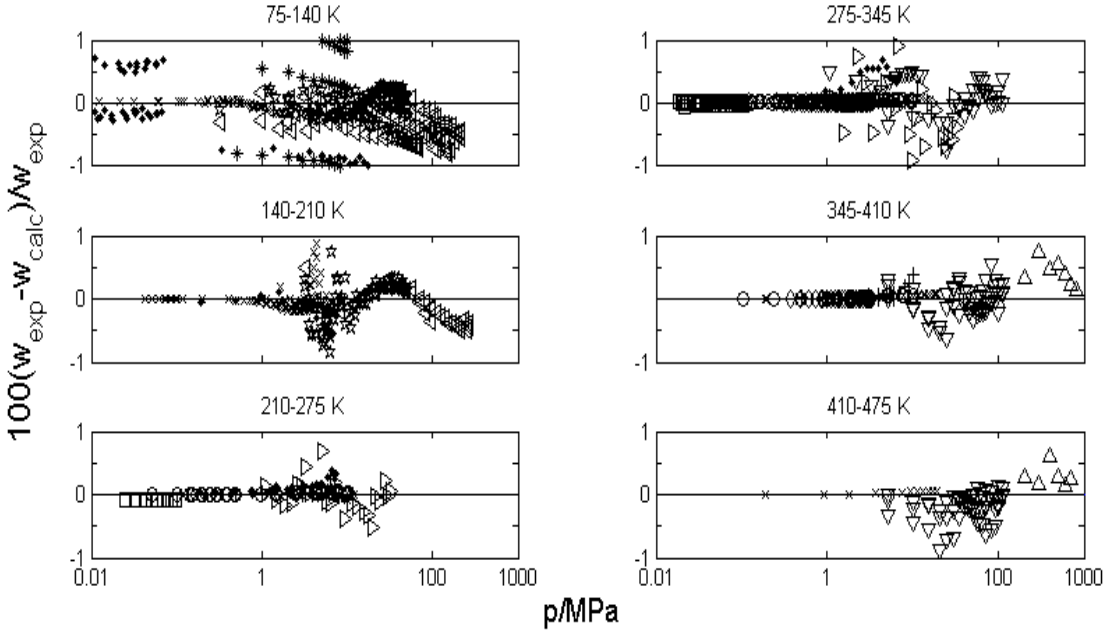

+ *Beckermann* (1993)
○ *Boyes* [59]
* *Carome et al* [69]
× *Estrada & Trusler* [68]
□ *Erwing & Trusler* [58]
◊ *Hurly* [70]
▵ *Kachanov* [71]
▽ *Lacam* [72]
▷ *Sharif* [73]
◁ *Streett* [74]
☆ *Thoen* [75]
◆ *Van Itterbeek* [76] [77]

Figure 31. Comparison of speed of sound data with rational equation

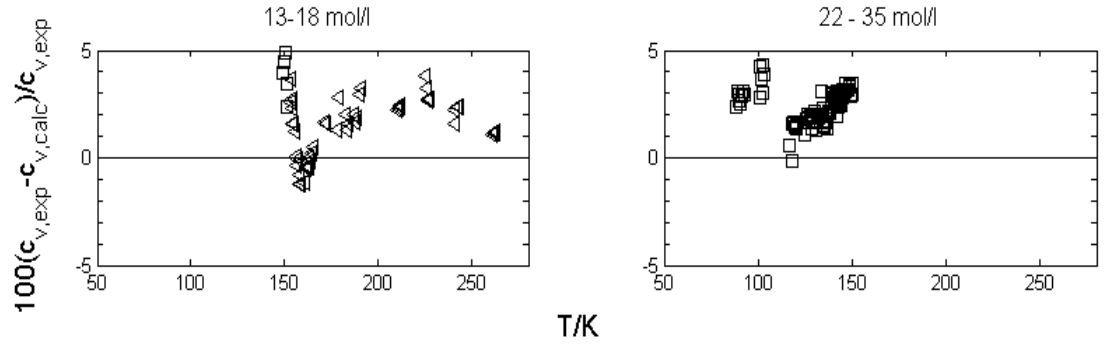

◁ *Anisimov* [78]
□ *Gladun* [79]

Figure 32. Relative error from isochoric heat capacities data and rational equation

4.6 Equation of state for methane

Methane is the simplest compound in the group of alkanes. It also is of practical interest because methane is the major component in natural gas, and it is important in production of chemical products. Accurate predictions of thermophysical properties are important in optimization and design of chemical plants [36]. Additionally, liquefied natural gas (methane) production requires accurate predictions over wide ranges of pressure and temperature. Table 11 contains some methane physical properties.

Table 11. Physical properties of methane

	T /K	p /kPa	ρ / kg·m^{-3}
Triple Point	90.6941±0.0025	11.696±0.002	
Critical Point	190.5640±0.0120	4592.200±2.000	162.66±0.2

4.6.1 Data sets

Many experimental data are available in the literature because of its importance to the natural gas industry. However, data uncertainty must be known in order to develop accurate EoS. Also, combinations of different thermodynamic properties give an idea of fluid behavior over wide ranges. The development of the EoS for methane uses a similar approach to that for nitrogen. Table 12 presents the selected methane data sets, which are based upon the assessment presented by Setzmann and Wagner [36].

4.6.1.1 *p-ρ-T*

The EoS for methane uses 11 *p-ρ-T* sets that cover temperatures from 100 K to 623 K and pressures up to 1,000 MPa. In 1964, Douslin et al. [80] measured gas

compressibility of methane from 0 °C to 350 °C at pressures up to 38 MPa, using a stainless steel pycnometer. Later, Jaeschke and Hinze [81] performed density measurements using a Burnett apparatus from 270 K to 353 K at pressures up to 30 MPa with an uncertainty of ±0.05 %. In 1988, Kleinraham et al. [82] used a two-sinker magnetic suspension densimeter (MSD) up to 8 MPa and temperatures from 273 K to 323 K with uncertainties of ±0.02 % in density. Later, Pieperbeck et al. [83] used a modified version of that MSD to collect data up to 12 MPa with similar range in temperature. In 1991, Achtermann et al. [84] measured refractive index and density isotherms for methane from 273 K to 373 K at pressures up to 34 MPa with ±0.04 % of error. Additionally in 1991, Handel et al. [85] published a p-ρ-T relation for the homogeneous gas and liquid regions for temperatures from 100 K to 260 K at pressures up to 8 MPa. These are unique data with consistent measurements in the liquid region. In 2001, Klimeck et al. [86] extended the temperature range to 520 K with uncertainties of ±0.07 %. Kortbeek and Schouten [87] presented densities of methane at 298 K up to 1,000 MPa. Recently, Cristancho et al. [26] used a high-pressure MSD for pressures up to 200 MPa and temperatures from 298 K to 450 K with a claimed experimental accuracy of ±0.05 %. Table 12 summarizes data information including ranges and uncertainties.

4.6.1.2 Vapor pressure

In 1986, Kleinrahm [10] measured liquid and vapor saturated densities for temperatures from 90 K to the critical point. His claimed uncertainty is ±0.02 %, but according to previous work [36] the data below 180 K data could have higher errors.

4.6.1.3 Virial coefficients

Douslin et al. [80] and Kleinramn et al. [82] calculated second virial coefficients for temperatures from 273 K to 623 K with a claimed uncertainty of ±0.2 $cm^3 \cdot mol^{-1}$.

4.6.1.4 Speed of sound

This work uses three speeds of sound data sets covering temperatures from 150 K to 375 K at pressures up to 1,000 MPa. Lemming [88] and Trusler [89] covered values up to 0.5 MPa and 10 MPa, respectively, with reported uncertainties between ±0.01 % and ±0.07 %. Kortbeek and Schouten [87] measured speeds of sound for pressures up to 1,000 MPa and temperatures from 148 K to 298 K. These authors claim errors of ±0.5 % in speeds of sound, but because of extreme pressure conditions, experiments could have higher uncertainties.

4.6.1.5 Isochoric heat capacities

Younglove [90] measured isochoric heat capacities for compressed and liquefied methane. These data cover temperatures from 91 K to 300 K at densities from 8 to 28 $mol \cdot cm^{-3}$. The author claims uncertainties of ±0.5 % with higher values at the critical point. However Setzmann and Wagner [36] show that the errors could be as high as ±5 %. Table 12 shows details about the Younglove heat capacity data.

Table 12. Summary of selected *p*-ρ-*T* experimental data for Methane

Density

Source	**Year**	*T* /K	*p* /MPa	Δ*T* /mK	Δ*p*/*p* (%)	Δρ/ρ (%)
Douslin et al. [80]	1964	273-623	1.6-38	1	0.03	0.03-0.2
Pope	1972	126-191	0.1-4.7	10	0.01	0.03-0.06
Kleinrahm et al. [10]	1986	180-190	3.2-4.6	3	0.007	0.02
Jaeschke & Hinze[81]	1991	269-353	0.3-30			0.05
Kleinrahm et al. [82]	1988	273-313	0.1-8	3	0.007	0.02
Achtermann et al. [84]	1991	273-373	1-34			0.04
Handel et al. [85]	1991	100-260	0.1-8	3	0.007	0.02
Kortbeek & Schouten [87]	1989	298.15	150-1000			0.1
Pieperbeck et al. [83]	1990	273-323	0.1-12	5	0.007	0.02
Klimeck et al. [86]	2001	240-520	2-30			0.07
Cristancho et al. [26]	2010	298-450	1-180	2		0.05

Vapor Pressure

Source	**Year**	*T* /K	*p* /MPa	Δ*T* /mK	Δ*p*/*p* (%)	Δρ/ρ (%)
Kleinrahm et al. [10]	1986	90-190	0.01-4.6	3	0.08	0.08

Second Virial

Source	**Year**	*T* /K	*p* /MPa	Δ*B* /cm^3·mol^{-1}
Douslin et al. [80]	1964	273-623		0.2
Kleinrahm et al. [82]	1988	273-323		0.15

Speed of Sound

Source	**Year**	*T* /K	*p* /MPa	Δ*T* /mK	Δ*p*/*p* (%)	Δ*w*/*w* (%)
Trusler [89]	1992	150-375	0.09-10			0.01-0.07
Lemming [88]	1989	230-350	0.1-0.5			0.01
Kortbeek et al. [87]	1989	148-298	100-1000			0.1-0.5

Table 12. Continued

Isochoric Heat Capacity						
Source	**Year**	T /K]	ρ /mol·dm^{-3}	ΔT /mK	$\Delta p/p$ (%)	$\Delta C_v/C_v$ (%)
Younglove [90]	1974	91-300	8-28			1-5

4.6.2 Methane results

Figure 33 shows six *p-ρ-T* data sets described within their uncertainty values except in the critical region. For temperatures below 220 K, density predictions are within ±0.05 % but pressure errors can increase up to ±0.1 %. For temperatures between 220 and 280 K predictions are within ±0.05 % in density for pressures below 12 MPa and ±0.07 % for higher pressures. For temperatures higher than 280 K and pressures lower than 12 MPa, predictions are within ±0.02 % and higher pressure errors increases up 0.05 %.

Figure 34 contains relative deviations for three *p-ρ-T* data from 100 K to 630 K. The REOS predicts density values within the experimental uncertainty for Pope and Douslin [80] data. Handel et al. [85] data have greater errors because pressure uncertainties in liquid region are significant higher.

The REOS can predict density values for high-pressure regions as well. Figure 35 shows predictions of density within 0.05 % for pressures below 200 MPa from the data reported by Cristancho et al. [26] and within 0.15 % up to 1,000 MPa for the values reported by Kortbeek et al. [87].

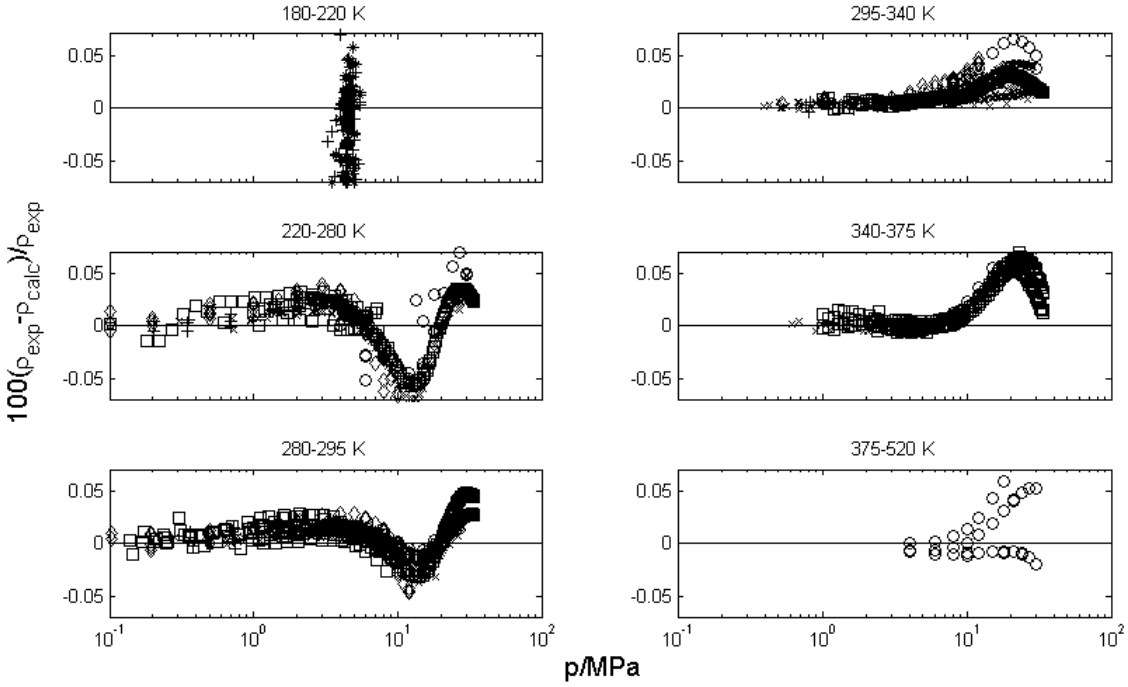

+ *Kleinrahm* [82] ○ *Klimeck* [86]
× *Jaeschke &Hinze* [81] □ *Achtermann* [84]
◊ *Pieperbeck* [83] **Kleinrahm* [10]

Figure 33. Comparison of accurate *p-ρ-T* methane data sets and rational equation of state

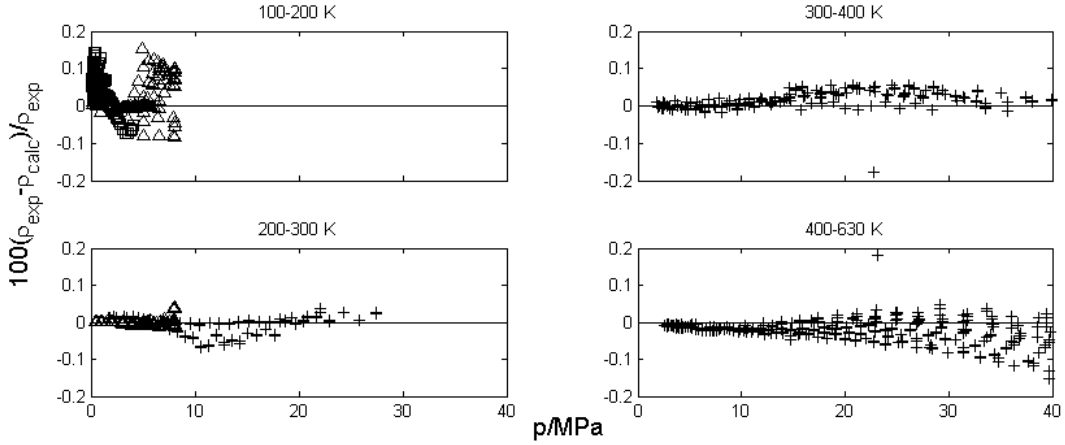

+ *Douslin* [80] □ *Pope* △ *Handel* [85]

Figure 34. Relative error of *p-ρ-T* methane data sets up to 40 MPa and rational equation of state

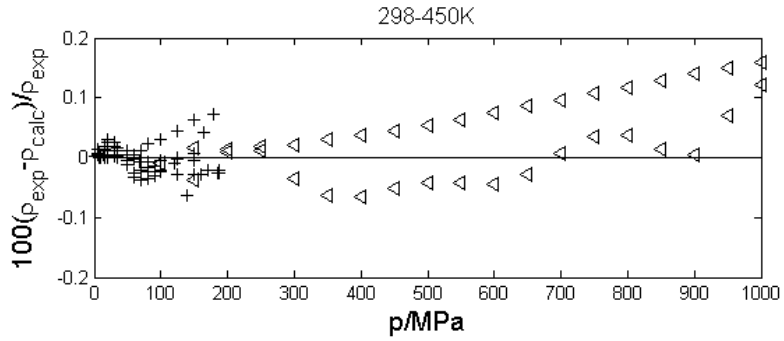

+ *Cristancho* [26] ◁ *Kortbeek & Schouten* [87]

Figure 35. Relative error of high pressure *p-ρ-T* methane data sets and rational equation of state

The REOS describes saturated vapor densities within ±0.01 % for temperatures from 90 K to critical points, however, the saturated liquid densities have errors up 0.12 %. The REOS describes vapor pressures within ±0.05 % except those at low temperatures, which may indicate problems. In liquefied region pressure errors are significant because of the density-pressure derivative $(\partial p/\partial \rho)_T$, especially for low temperatures where vapor pressure values are lower than atmospheric pressure. It is possible that densities and vapor pressures values below 115 K are over-predicted causing issues, but there are not enough data to check that assumption.

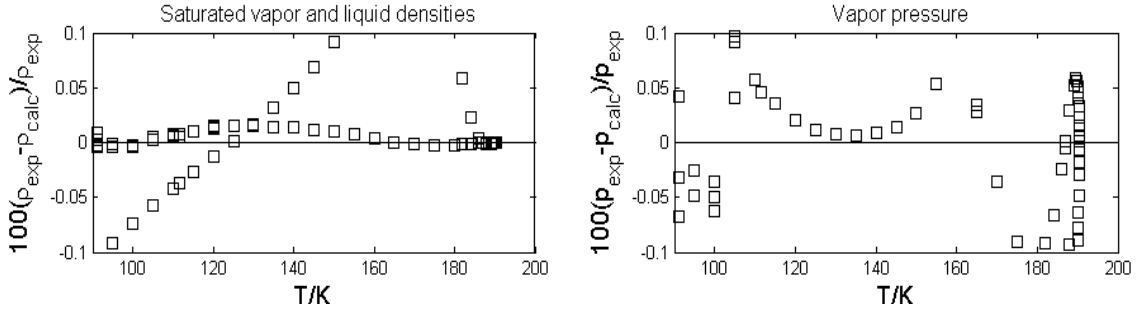

□ *Kleinrahm* [10]

Figure 36. Liquid and vapor saturated densities (left) and vapor pressure (right) for methane

Figure 37 shows REOS predictions for second virial coefficients over a wide range of temperature. Experimental data are available for temperatures higher than 273 K. The REOS describes experimental second virial coefficient data and theoretical behavior adequately.

Speed of sound data are organized in two pressure ranges. For speeds of sound below 10 MPa, the REOS predicts values within ±0.15 %, which is higher than claimed uncertainties. However, it predicts most of the data within ±0.05 % similar to the uncertainty values. The claimed uncertainty at higher pressures is ±0.5 %, The REOS calculates values within ±2 %, which is a reasonable prediction for this pressure range. Figure 38 contains speed of sound predictions using two different pressure ranges.

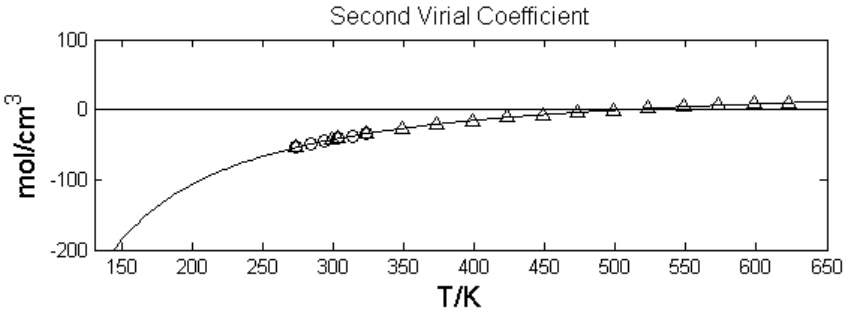

Δ *Douslin* [80] ○ *Kleinraham* [82]

Figure 37. Second virial coefficient data and predicted values from rational equation (-)

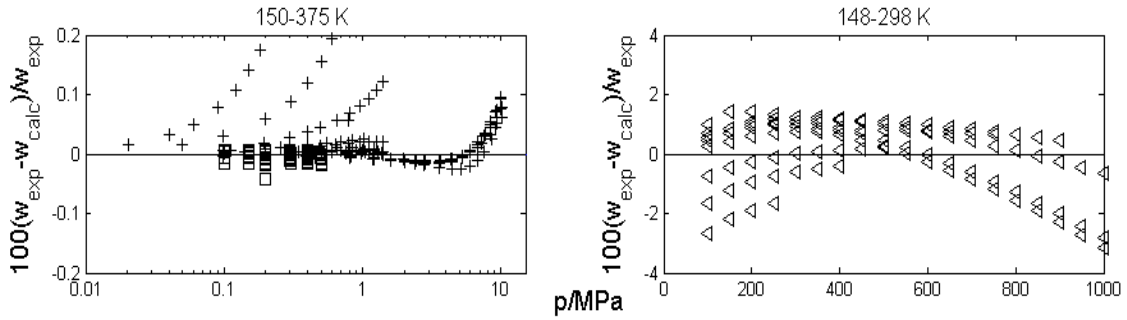

+ *Trusler* [89] □ *Lemming* [88] ◁ *Kortbeek et al* [87]

Figure 38. Comparison of speed of sound data and rational equation.

Figure 39 compares REOS predictions for isochoric heat capacity with the Younglove data. For supercritical temperatures, the REOS calculations are within 1.5 %, but deviations increase rapidly for values below 190 K especially for high densities.

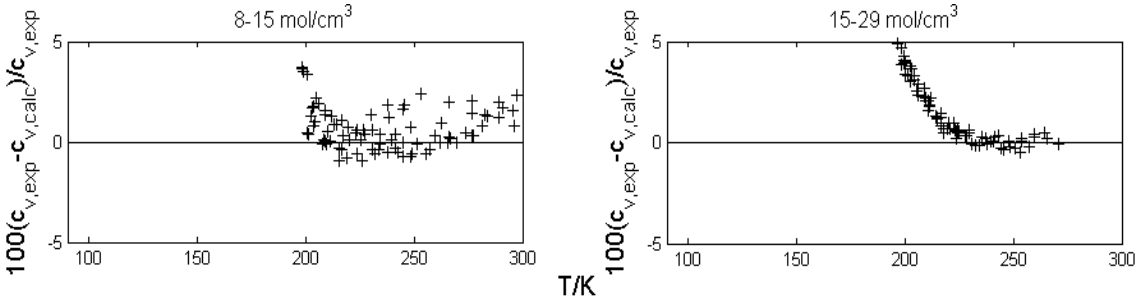

+ *Younglove* [90]

Figure 39. Relative error of isochoric heat capacity data from the REOS

4.7 Computational speed analysis

Previous sections have illustrated that the REOS can describe *p-ρ-T* and vapor pressure data for pure nitrogen and argon within the uncertainty values claimed by authors. Also, this equation makes reasonable predictions of derivative thermodynamic properties such as speeds of sound and isochoric heat capacities. The REOS has accuracy similar to reference EoS for nitrogen and argon with a similar number of

coefficients, but it does not include exponential terms. This work seeks to prove that similar accuracies are possible with lower computational costs.

To do a comparative analysis of computational cost with different EoS, the reference equation of state for nitrogen [32] and the REOS were programmed using C++, presented in Appendix E. Both equations define pressure as function of Helmholtz energy, but each has its own residual functional. The REOS function and coefficient values are in equation 52 and table 5 respectively. Details about the form and coefficient values of the reference equation of state appear in Span et al. [32].

The C++ code evaluates pressure using temperature and density values with both residual Helmholtz energy definitions, and repeats the process 1 million times. The program records initial and final times and later calculates time required per evaluation. Repeating this routine several times produced similar values every time. The REOS requires approximately 0.035 microseconds per evaluation compared to 0.700 microseconds for the reference equation of state.

The REOS computes at least 20 times faster than the reference form. It does not include exponential functions and uses only integer powers, which improves computational time significantly. According to Mathias et al. [49], evaluating a multiplication function is 15 times faster than evaluating an exponential. Furthermore, they note that multiplication is 32 times faster than power function evaluations. The REOS uses only power functions with integer values, because integer power functions can be calculated as a combination of multiplication operations (*e.g.*, Horner's method).

4.8 Conclusions

This section has shown that an REOS based upon the residual Helmholtz energy is an acceptable alternative for developing an EoS to calculate densities and vapor-liquid equilibrium. Additionally, it presents examples of REOS for nitrogen and argon, including p-ρ-T, vapor pressures, speeds of sound and isochoric heat capacities up to 1000 MPa. Ideal curves for nitrogen show that the REOS has proper behavior at high temperatures and pressures. Finally, a computational time analysis shows that the REOS is at least 20 times faster than the reference equation that incorporate exponential terms to achieve the same level of accuracy.

5. MIXING RULE BASED UPON HELMHOLTZ FREE ENERGY

Industrial applications require predictions of thermophysical properties for multicomponent mixtures. Section 4 covered the development of a rational EoS for pure components over wide ranges of temperature and pressure. However, predictions in mixtures must include interactions effects among molecules of different species. A statistical-mechanical solution relating thermophysical properties and intermolecular potentials [91] does not currently exist. Empirical models do exist for predicting mixtures properties as function of measurable variables.

This Section discusses some of the classical and empirical mixing rules. Also this Section describes the mixing rules used by GERG-2008, which has showed remarkable results for some multicomponent mixtures. Later, this work proposes a mixing rule based upon residual Helmholtz energy and a classical approach. Finally an empirical rational form and a least square regression routine calculate binary interaction coefficients for nitrogen + methane mixture using p-ρ-T data presented in Section 3.

5.1 Classical definition of mixing rule

The virial EoS describes the compressibility factor as an infinite series in density or pressure. Virial coefficients for pure fluids are functions of temperature and are related to intermolecular potentials between molecules [91] [92]. In pure fluids, interactions occur only between molecules of the same species, but in mixtures interactions occur between molecules of different species as well. The n^{th} virial

coefficient reflects *n*-body interactions [92]. Truncating Equation 67 after a few terms is common, but limits the applicable density range.

$$Z = \frac{PV}{RT} = 1 + B\rho + C\rho^2 + \ldots \quad [67]$$

Statistical mechanics offers theoretical expressions for second (B) and third (C) virial coefficients for mixtures in terms of mole fraction and factors representing 2- and 3-body interactions respectively.

$$B = \sum_{i=1}^{N}\sum_{j=1}^{N} x_i x_j B_{ij}(T) \quad [68]$$

$$C = \sum_{i=1}^{N}\sum_{j=1}^{N}\sum_{k=1}^{N} x_i x_j x_k C_{ijk}(T) \quad [69]$$

For a binary mixture, equation 68 becomes:

$$B = x_1^2 B_{11} + 2x_1 x_2 B_{12} + x_2^2 B_{22} \quad [70]$$

In this equation, B_{11} is the second virial coefficient for pure fluid 1, which is the contribution from 2-body interactions between molecules of component 1, B_{22} is the second virial coefficient for pure fluid 2, which is the contribution from interactions between molecules of component 2, and B_{12} is the contribution from intermolecular interactions between molecules of two different species. Cross virial coefficients (B_{12}) cannot be predicted exactly from pure virial coefficients, because the unique interaction does not contribute to either pure virial.

Equation 70 can be rearranged as:

$$B_{mix} = \sum_{i=1}^{n} x_i B_{ii} + \sum_{i=1}^{n} \sum_{j=i+1}^{n} x_i x_j \delta B_{ij} \qquad [71]$$

in which

$$\delta B_{ij} = (2B_{ij} - B_{ii} - B_{jj}) \qquad [72]$$

McGregor et al. [92] [93] showed that mixture third virial coefficients also can be expressed as a quadratic form

$$C_{mix} = \sum_{i=1}^{n} x_i C_{iii} + \sum_{i=1}^{n} \sum_{j=i+1}^{n} x_i x_j \delta C_{ij} \qquad [73]$$

based on the approximation

$$dC_{ij} \approx 3C_{iij} - 2C_{iii} - C_{jjj} \approx 3C_{ijj} - C_{iii} - 2C_{jjj} \qquad [74]$$

The errors introduced by this approximation were smaller than the experimental uncertainties for the mixtures considered by McGregor et al. [92].

5.2 Mixing rule in GERG – 2008

The dimensionless Helmholtz energy of a mixture, expressed as a combination of ideal and residual contributions is:

$$\frac{A(\rho,T,x)}{RT} = \alpha(\delta_m, \tau_m, x) = \alpha^o(\rho,T,x) + \alpha^r(\delta_m, \tau_m, x) \qquad [75]$$

The ideal contribution the Helmholtz energy for an ideal gas mixture of *N* components

$$\alpha^o(\rho,T,x) = \sum_{i=1}^{N} x_i \left[\alpha_{oi}^0(\rho,T) + \ln x_i \right] \qquad [76]$$

GERG-2008[37] uses a modern functional to describe the residual Helmholtz energy. This modern functional has shown remarkable results for describing pure components over wide ranges of density and temperature. Kunz and Wagner [37] described residual Helmholtz energy of mixtures as

$$\alpha^r\left(\delta_m,\tau_m,x\right)=\sum_{i=1}^{N}x_i\alpha_{oi}^r\left(\delta_m,\tau_m\right)+\sum_{i=1}^{N-1}\sum_{j=i+1}^{N}\Delta\alpha_{ij}\left(\delta,\tau,x\right) \quad [77]$$

in which

$$\tau_m=\frac{T_r\left(x\right)}{T} \quad [78]$$

$$\delta_m=\frac{\rho}{\rho_r\left(x\right)} \quad [79]$$

The first sum is the mole fraction average of the residual energies of pure substances (α_{oi}^r) at the same reduced temperature and density as the mixture, and the second sum is a departure function that describes the contribution of interactions between molecules of different species. This departure function has a generalized form with fitted parameters for each binary mixture.

In pure components, reference density (ρ_r) and temperature (T_r) are the critical point values. Because there is not a rigorous theoretical definition for critical temperature or density in mixtures, the reducing parameters for temperature and density are defined arbitrarily. GERG-2008 proposed,

$$T_r\left(x\right)=\sum_{i=1}^{N}\sum_{j=1}^{N}x_ix_j\beta_{T,ij}\gamma_{T,ij}\frac{x_i+x_j}{\beta_{T,ij}^2x_i+x_j}\left(T_{c,i}T_{c,j}\right)^{0.5} \quad [80]$$

$$\frac{1}{\rho_r\left(x\right)}=\sum_{i=1}^{N}\sum_{j=1}^{N}x_ix_j\beta_{\rho,ij}\gamma_{\rho,ij}\frac{x_i+x_j}{\beta_{\rho,ij}^2x_i+x_j}\frac{1}{8}\left(\frac{1}{\rho_{c,i}^{1/3}}+\frac{1}{\rho_{c,j}^{1/3}}\right)^3 \quad [81]$$

to define the reference temperature (T_r) and density (ρ_r) for mixtures. Every binary mixture requires four fitted parameters along with the critical density and temperature of pure substances.

The departure function ($\Delta\alpha^r$) improves the accuracy of the model describing the system as a non-ideal mixture. In general, the correction is minor compared to the contributions of the pure substance values. The form of the departure function form for the modern functional of free energy is

$$\Delta\alpha^r\left(\delta_m,\tau_m,x\right)=\sum_{i=1}^{N-1}\sum_{j=i+1}^{N}x_i x_j F_{ij}\alpha_{ij}^r=\sum_{i=1}^{N-1}\sum_{j=i+1}^{N}x_i x_j F_{ij}\alpha_{gen}^r \qquad [82]$$

in which F_{ij} is a unique parameter for each cross interaction and α_{gen} is a generalized form of the interaction energy (α_{ij}^r).

The generalized form proposed by Lemmon and Jacobsen [94] for the interaction energy (α_{ij}^r) in multi-component mixtures is

$$\alpha_{gen}^r=\sum_{k=1}^{10}n_k\delta_m^{dk}\tau_m^{tk} \qquad [83]$$

They applied this generalized function to 22 binary mixtures, using same coefficients, but varying parameters F_{ij} for each mixture

Adding to Lemmon and Jacobsen [94] work, Kunz and Wagner [37] developed specific departure functions for some binary mixtures. The functional form for a specific departure function in GERG-2008 is

$$\alpha_{ij}^r\left(\delta_m,\tau_m\right)=\sum n_k\delta_m^{dk}\tau_m^{tk}+\sum n_k\delta_m^{dk}\tau_m^{tk}\exp\left[-\eta\left(\delta_m-\epsilon_k\right)^2-\beta_k\left(\delta_m-\gamma_k\right)\right] \qquad [84]$$

Similar to the residual Helmholtz energy in pure fluids, the departure function number and value of coefficients change with each binary mixture. The function includes a summation of Gaussian bell shaped-terms (ε, γ, η) and non-integer exponent values for temperature (t_k). For the nitrogen + methane mixture, equation 87 contains nine linear coefficients (n_k), six Gaussian bell-shaped terms and six non-integer exponents.

The departure function for a multicomponent mixture is the sum of all departure functions (generalized or specific) for each binary mixture involved [37]. Figure 40 shows which binary mixtures have specific or generalized departure functions. Binary mixtures in yellow have specific departure functions. Those in orange have generalized departure functions. Binary mixtures in blue, green and gray do not have departure functions.

GERG-2008 [37] can predict with high accuracy some multicomponent gas mixtures [7]. However, the departure function requires binary data over wide ranges of temperature and density due to the complicated mathematical form and the large number of fit parameters. Figure 40 shows that only seven specific and eight generalized functions out of 210 possible binary mixtures are available. GERG-2008 uses reducing functions in residual Helmholtz energy for most of the mixtures without departure functions.

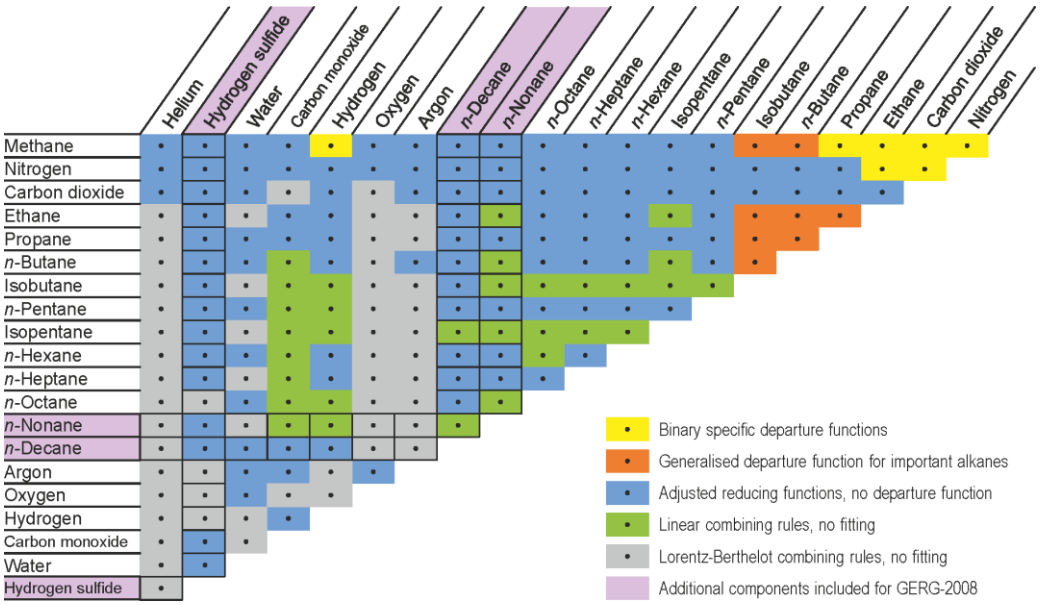

Figure 40. Overview of the 210 binary mixtures implemented in GERG-2008. *Acknowledgment:* [37]. This EoS includes 21 natural gas components.

GERG-2008 evaluates Helmholtz energies at reduced conditions of the mixture, but the reducing parameters are not the true critical temperature and pressure for the mixture. Equations 83 and 84 calculate the reference temperature and density of a mixture using empirical forms and fitted parameters because a theoretical solution does not exist. This approach assumes that molecules of components behave similarly at the same reduced conditions. However, because pure fluid equations evaluate properties at reduced conditions they do not use real density and temperature values. In effect, same reduced conditions impose different actual conditions for the mixture under study. This situation violates the ideal mixture approach and would create problems for mixtures without data for validation.

5.3 Binary interaction based upon a rational form

This work proposes a combination of classical mixing rules and an EoS based upon Helmholtz energy. As table 4 shows, the second virial coefficient is the zero density limit of the derivative of the residual Helmholtz energy with respect to density ($B = \lim_{\delta \to 0} \alpha_{\delta}^{r}$).

Based upon the statistical mechanics solution for mixture second virial coefficients (equation 70), and the McGregor et al [92] [93]approximation for third virial coefficients (equation 73), where both the second and third virial coefficients are described as quadratic functions, this work proposes a quadratic mixing rule for residual Helmholtz energy:

$$\frac{A_{mix}^{r}(T,r)}{RT} = \sum_{i=1}^{N} \sum_{j=1}^{N} a_{i,j}^{r} x_i x_j \qquad [85]$$

This equation has the same form as the second virial coefficient (see Section 5.1), so the same algebra applies. Using a binary mixture as an example, and following equations 70, 71 and 72, provides an alternate form for the residual Helmholtz energy of a mixture:

$$\frac{A_{mix}^{r}(T,\rho)}{RT} = x_1 \alpha^{r}{}_1 + x_2 \alpha^{r}{}_2 + x_1 x_2 \Delta \alpha_{1,2}^{r} \qquad [86]$$

in which

$$\Delta \alpha_{1,2}^{r} = 2\alpha_{1,2}^{r} - \alpha^{r}{}_2 - \alpha^{r}{}_1 \qquad [87]$$

Equation 87 shows that the departure function ($\Delta\alpha_{1,2}^r$) is a combination of pure component energies and the interaction energies of molecules of different species. The corresponding forms for multicomponent mixtures are:

$$\frac{A_{mix}^r(T,\rho)}{RT} = \sum_{i=1}^{n}\sum_{j=1}^{n} x_i x_j \alpha_{ij}^r \qquad [88]$$

$$\frac{A_{mix}^r(T,r)}{RT} = \sum_{i=1}^{n} x_i a_i^r(T,r) + \sum_{i=1}^{n}\sum_{j=i+1}^{n} x_i x_j \left(2a_{i,j}^r(T,r) - a_i^r(T,r) - a_j^r(T,r)\right) \qquad [89]$$

An exact solution for intermolecular interaction energy between two different components ($\alpha_{1,2}^r$) does not exist. Some authors (*e.g.* Kreglewsky [95]) have used empirical equations to describe those effects. Following the rational equation of state model, this work proposes a rational equation in density, with temperature dependent parameters,

$$\alpha_{1,2}^r = \left(\frac{\gamma_1\rho + \gamma_2\rho^2}{1+\gamma_3\rho}\right) \qquad [90]$$

in which

$$\gamma_k = c_{0,k} + c_{1,k}/T \qquad [91]$$

The coefficients may vary for each binary mixture, but the functional form should be similar for all binary mixtures.

Section 3 presented *p*-ρ-*T* data for three nitrogen + methane mixtures from 300 to 470 K at pressures up to 140 MPa. The definition of compressibility factor is

$$Z = \frac{P}{\rho RT} \qquad [92]$$

Equation 93 calculates an experimental value for the derivative of the Helmholtz energy ($\alpha^r_{\rho,mix}$) using compressibility factors. The pure component derivatives are expressed as functions of reduced densities, but for mixtures it is more convenient to use molar density because the critical parameters of mixtures usually are not known accurately. The residual Helmholtz energy for the mixture is given in terms of the compressibility factor by:

$$\frac{1}{RT}\frac{\partial A^r_{mix}}{\partial \rho} = \alpha^r_{\rho,mix} = \frac{Z_{mix} - 1}{\rho_{mix}} \qquad [93]$$

For the quadratic mixing rule.

$$\frac{1}{RT}\frac{\P A^r_{mix}}{\P r} = a^r_{r,mix} = x_1^2 a^r_{d,1}\left(t_1, d_1\right) + x_2^2 a^r_{d,2}\left(t_2, d_2\right) + 2a^r_{r,1,2}\left(T, r_{mix}\right)x_1 x_2 = \frac{Z_{mix} - 1}{r_{mix}} \qquad [94]$$

in which the Helmholtz energy derivatives for methane and nitrogen come from the rational equations of state. All REOS terms are evaluated at the temperature and pressure of the mixture, so that for methane $d_1 = r_{mix} / r_{c,1}, \tau_1 = T_{c,1} / T$, and for nitrogen $d_2 = r_{mix} / r_{c,2}$ and $\tau_2 = T_{c,2} / T$.

The interaction energies are functions of density and temperature. The cross interaction energy derivative from the proposed rational form is:

$$\alpha^r_{\rho,1,2} = \frac{\left(\gamma_1 + 2\gamma_2\rho\right)\left(1 + \gamma_3\rho\right) - \left(\gamma_3\right)\left(\gamma_1\rho + \gamma_2\rho^2\right)}{\left(1 + \gamma_3\rho\right)^2} \qquad [95]$$

Combining this result with equation 94 leads to a working equation for evaluating the parameters

$$\frac{\left(\gamma_1 + 2\gamma_2\rho\right)\left(1+\gamma_3\rho\right) - \left(\gamma_3\right)\left(\gamma_1\rho + \gamma_2\rho^2\right)}{\left(1+\gamma_3\rho\right)^2} = \frac{1}{2x_1x_2}\left[\frac{Z_{mix}-1}{\rho_{mix}} - x_1^2\alpha_{\delta,1}^r\left(\tau_1,\delta_1\right) - x_2^2\alpha_{\delta,2}^r\left(\tau_2,\delta_2\right)\right] \quad [96]$$

Table 13 contains the parameters for obtained for the methane-nitrogen cross interaction energies by fitting equation 96 to the experimental compressibility factors. Figure 41 presents the relative deviations between the experimental compressibility factors from the REOS mixture model for methane + nitrogen mixtures. The agreement is excellent and shows that the REOS approach to the cross terms is capable of describing mixtures accurately for the Methane + nitrogen binary system.

Table 13. Binary interaction parameter for methane-nitrogen mixtures from 300 K to 470 K and up to 140 MPa

$c_{j,k}$	j	k	
$c_{0,1}$ / kmol^{-1}·m^3	0	1	0.0528
$c_{1,1}$ / kmol^{-1}·m^3·K	1	1	-21.0427
$c_{0,2}$ / kmol^{-2}·m^6	0	2	-0.0004
$c_{1,2}$ / kmol^{-2}·m^6·K	1	2	0.4239
$c_{0,3}$ / kmol^{-3}·m^9	0	3	-0.0166
$c_{1,3}$ / kmol^{-3}·m^9·K	1	3	-0.7537

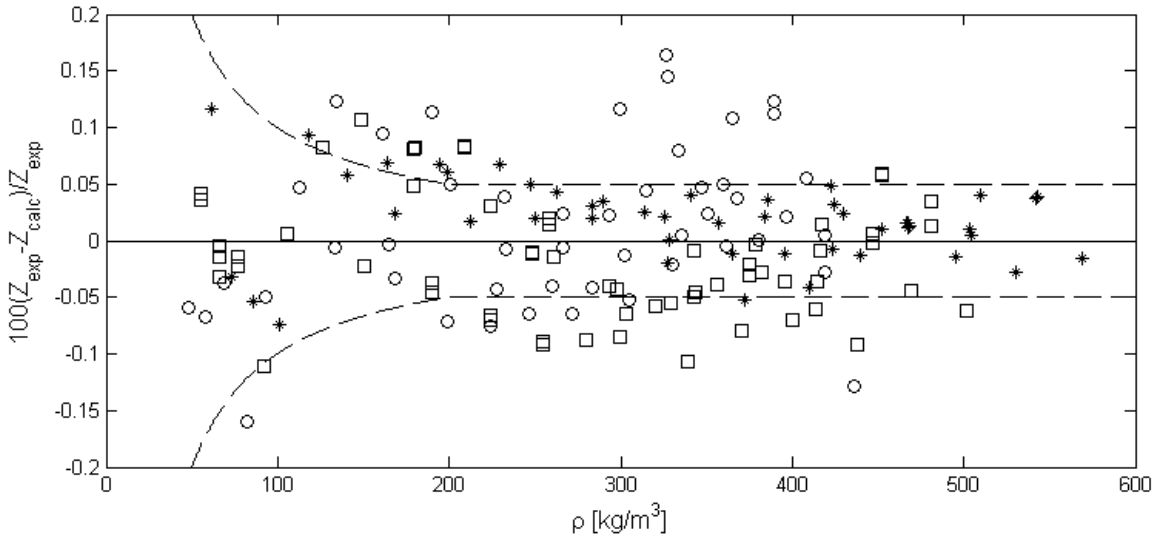

Figure 41. Relative deviations between the experimental compressibility factors and the rational equation of state values for nitrogen + methane mixtures.
($\circ x_{CH4}$=0.75,$\square x_{CH4}$=0.50 and $\ast\, x_{CH4}$=0.25)

6. CONCLUSIONS AND RECOMMENDATIONS

This work describes a vibrating tube apparatus for measuring densities from 300 K to 470 K at pressures up to 140 MPa. This instrument provides an accurate and fast method for high-pressure density measurements with errors of 0.1 kg/m^3, which is remarkable for high pressure vibrating devices. The calibration methodology is the main factor for reducing total uncertainties. Measurements for methane, nitrogen and argon and accurate equations of state provide the calibration information for the VTD. This combination of well-known fluids reduces significantly the experimental uncertainties over a wide range of densities. In addition, a physically-based model with only four parameters describes the temperature and internal pressure dependence of the VTD calibration, reducing overall measurement uncertainties. Repeating the vacuum resonant period for each isotherm improves repeatability and minimizes hysteresis effects over long periods of time.

The VTD uses small volumes of sample, thus minimizing undesired consequences in a release scenario. It can measure hazardous fluids at high pressures with a reduced risk. Hydrogen sulfide is a common element in natural gas mixtures, and it is highly corrosive and toxic. The VTD is a good selection for studies of this component.

This work validated the VTD calibration methodology using ethane and carbon dioxide measurements. P-ρ-T data cover pressures up to 140 MPa. This work compares VTD densities with previously published MSD results. The MSD technique does not require calibration and can perform high accuracy measurements. The VTD also

produced measurements of nitrogen + methane mixtures for four isotherms between 300K and 470 K at pressures up to 140 MPa. These data cover a range of high-pressure data that can validate, improve and develop current and new EoS.

Many binary mixtures lack data at high pressures. The VTD can perform fast measurements with good accuracy. Methane + ethane, methane + propane, ethane + propane, ethane + nitrogen, argon + nitrogen, argon + methane and propane + nitrogen are some of the mixtures that should be measured with a VTD. Also, some ternary mixture data would help when developing new EoS and studying intermolecular interactions.

Section 4 of this dissertation presents a new equation of state based upon a rational form of the residual Helmholtz energy. This form describes behavior of pure fluids properties accurately over wide ranges of temperature and pressure. This EOS has similar accuracy to that of the modern functional with a more efficient mathematical form. According to preliminary calculations, computational time is 20 times faster compared to modern functional equations. Section 4 presents an REOS for nitrogen, argon and methane.

More REOS for pure components should be developed using the similar methodologies. This work suggests the same mathematical form in density for other components, but temperature behavior could be modified for more complex molecules. The REOS can be improved using fitting software developed by NIST to improve behavior in regions lacking data. An alternative solution for the critical region is a Gaussian function near the critical temperature. It may improve predictions slightly, but

it will increase computational time. In the two-phase region, denominator values go to zero at certain temperature and density conditions creating poles. The poles do not affect prediction for pure components, but they could affect predictions for mixtures. The fitting program must include a constraint to prevent those poles.

Section 5 presents a mixing rule for the residual Helmholtz energy of a binary mixture. This rule is based upon a quadratic form and statistical mechanics definitions of the second virial coefficient. This approach follows the ideal solution concept and requires a small number of coefficients to make a correction. REOS for methane and nitrogen provide pure component contributions. A least squares minimization calculates interaction parameters for the mixture nitrogen + methane using density data from the VTD. This mixing rule describes data within 0.1 %, which is slightly higher than experimental uncertainty.

A quadratic mixing rule for the residual energy should be applied to more binary mixtures. The calculation of the binary parameters requires data at different temperatures and compositions. Other functions for the interaction parameter should be proposed and tested.

REFERENCES

[1] U.E.I. Administration, Annual energy outlook 2015, in, Washington, DC, **2015**.

[2] W. Wagner, R. Kleinrahm, H.W. Lösch, J.T.R. Watson, V. Majer, A.A.H. Pádua, L.A. Woolf, J.C. Holste, A.M. De Figueiredo Palavra, K. Fujii, J.W. Stansfeld, 5 - density, in: K.N.M. A.R.H. Goodwin, W.A. Wakeham (Eds.) *Experimental thermodynamics*, *Elsevier*, Amsterdam, **2003**, pp. 125-235.

[3] C. Fan, W. Shi, P. Zhang, H. Lu, N. Zhang, S. Work, H. Al-Saiari, A. Kan, M. Tomson, Ultrahigh-temperature/ultrahigh-pressure scale control for deepwater oil and gas production, *SPE Journal*, **17** (**2012**).

[4] P. Patil, S. Ejaz, M. Atilhan, D. Cristancho, J.C. Holste, K.R. Hall, Accurate density measurements for a 91% methane natural gas-like mixture, *The Journal of Chemical Thermodynamics*, **39** (**2007**) 1157-1163.

[5] M. Atilhan, High accuracy p-ρ-t measurements up to 200 MPa between 200 K and 500 K using a compact single sinker magnetic suspension densimeter for pure and natural gas like mixtures, Ph.D Dissertation, *Texas A&M University*,College Station, TX **2007**.

[6] M.O. McLinden, R. Kleinrahm, W. Wagner, Force transmission errors in magnetic suspension densimeters, *International Journal of Thermophysics*, **28** (**2007**) 429-448.

[7] M. Atilhan, S. Aparicio, S. Ejaz, D. Cristancho, I. Mantilla, K.R. Hall, *P–ρ–t* behavior of three lean synthetic natural gas mixtures using a magnetic suspension densimeter and isochoric apparatus from (250 to 450) K with pressures up to 150 MPa: Part II, *Journal of Chemical & Engineering Data*, **56** (**2011**) 3766-3774.

[8] D.E. Cristancho, I.D. Mantilla, S. Ejaz, K.R. Hall, G.A. Iglesias-Silva, M. Atilhan, Force transmission error analysis for a high-pressure single-sinker magnetic suspension densimeter, *International Journal of Thermophysics*, **31** (**2010**) 698-709.

[9] D.O. Ortiz-Vega, I.D. Mantilla, H.Y. Acosta, M.A. Gomez-Osorio, J.C. Holste, K.R. Hall, G.A. Iglesias-Silva, Uncertainty estimates for experimental density measurements: Effects of temperature, pressure and sample preparation, *The Journal of Chemical Thermodynamics*, **58** (**2013**) 14-19.

[10] R. Kleinrahm, W. Wagner, Measurement and correlation of the equilibrium liquid and vapour densities and the vapour pressure along the coexistence curve of methane, *The Journal of Chemical Thermodynamics*, **18** (**1986**) 739-760.

[11] J.C. Holste, K.R. Hall, P.T. Eubank, K.N. Marsh, High pressure *pvt* measurements, *Fluid Phase Equilibria*, **29** (**1986**) 161-176.

[12] J. Zhou, P. Patil, S. Ejaz, M. Atilhan, J.C. Holste, K.R. Hall, (*p, vm, t*) and phase equilibrium measurements for a natural gas-like mixture using an automated isochoric apparatus, *The Journal of Chemical Thermodynamics*, **38** (**2006**) 1489-1494.

[13] M. Atilhan, S. Aparicio, S. Ejaz, D. Cristancho, K.R. Hall, *Pρt* behavior of a lean synthetic natural gas mixture using magnetic suspension densimeters and an isochoric apparatus: Part I, *Journal of Chemical & Engineering Data*, **56** (**2011**) 212-221.

[14] P.L. Acosta-Perez, D.E. Cristancho, I.D. Mantilla, K.R. Hall, G.A. Iglesias-Silva, Method and uncertainties to determine phase boundaries from isochoric data, *Fluid Phase Equilibria*, **283** (**2009**) 17-21.

[15] A.d.P. Tibaduiza, D.E. Cristancho, D. Ortiz-Vega, I.D. Mantilla, M.A. Gomez-Osorio, R.A. Browne, J.C. Holste, K.R. Hall, Calculation of energies and entropies from isochoric and isothermal experimental data, *Journal of Chemical & Engineering Data*, **59** (**2014**) 999-1005.

[16] C.D. Holcomb, S.L. Outcalt, A theoretically-based calibration and evaluation procedure for vibrating-tube densimeters, *Fluid Phase Equilibria*, **150–151** (**1998**) 815-827.

[17] D.R. McGregor, A high pressure, high temperature vibrating tube densimeter: Densities of toluene, ethylbenzene, and 2,2,4-trimethylpentane, Ph.D Dissertation, *Texas A&M University*,College Station, TX, **1989**.

[18] L.A. Galicia-Luna, D. Richon, H. Renon, New loading technique for a vibrating tube densimeter and measurements of liquid densities up to 39.5 MPa for binary and ternary mixtures of the carbon dioxide-methanol-propane system, *Journal of Chemical & Engineering Data*, **39** (**1994**) 424-431.

[19] A.T. Sousa, P.S. Fialho, C.A.N. de Castro, R. Tufeu, B. Le Neindre, Density of hcfc 142b and of its mixture with hcfc 22, *Fluid Phase Equilibria*, **80** (**1992**) 213-225.

[20] O. Kratky, H. Leopold, S. H, Determination of density of liquids and gases to an accuracy of 10-6g/cm^3, with a sample volume of only 0,6-cm^3, *Zeitschrift fur Angewandte Physik*, **27** (**1969**) 273.

[21] P. Picker, E. Tremblay, C. Jolicoeur, A high-precision digital readout flow densimeter for liquids, *Journal of solution Chemistry*, **3** (**1974**) 377-384.

[22] S.L. Outcalt, M.O. McLinden, Automated densimeter for the rapid characterization of industrial fluids†, *Industrial & Engineering Chemistry Research*, **46** (**2007**) 8264-8269.

[23] C. Bouchot, D. Richon, An enhanced method to calibrate vibrating tube densimeters, *Fluid Phase Equilibria*, **191** (**2001**) 189-208.

[24] G.A. Iglesias-Silva, M. Bravo-Sánchez, A. Estrada-Baltazar, C. Bouchot, K.R. Hall, *p–ρ–T* data for 1-butanol and isobutyl alcohol from (283.15 to 363.15) K at pressures up to 66 MPa, *Journal of Chemical & Engineering Data*, **60** (**2015**) 1076-1090.

[25] E.F. May, W.J. Tay, M. Nania, A. Aleji, S. Al-Ghafri, J.P. Martin Trusler, Physical apparatus parameters and model for vibrating tube densimeters at pressures to 140 MPa and temperatures to 473 k, *Review of Scientific Instruments*, **85** (**2014**) 095111.

[26] D.E. Cristancho, I.D. Mantilla, S. Ejaz, K.R. Hall, M. Atilhan, G.A. Iglesia-Silva, Accurate *ρpt* data for methane from (300 to 450) K up to 180 MPa, *Journal of Chemical & Engineering Data*, **55** (**2010**) 826-829.

[27] C.R. Chamorro, J.J. Segovia, M.C. Martín, M.A. Villamañán, J.F. Estela-Uribe, J.P.M. Trusler, Measurement of the (pressure, density, temperature) relation of two (methane + nitrogen) gas mixtures at temperatures between 240 and 400 K and pressures up to 20 MPa using an accurate single-sinker densimeter, *The Journal of Chemical Thermodynamics*, **38** (**2006**) 916-922.

[28] G.C. Straty, D.E. Diller, (*p, v, T*) of compressed and liquefied (nitrogen + methane), *The Journal of Chemical Thermodynamics*, **12** (**1980**) 937-953.

[29] J.C. Seitz, J.G. Blencoe, R.J. Bodnar, Volumetric properties for {(1 −x)CO_2+xCH_4}, {(1 −x)CO_2+xN_2}, and {(1 −x)CH_4+xN_2} at the pressures (9.94, 19.94, 29.94, 39.94, 59.93, 79.93, and 99.93) MPa and temperatures (323.15, 373.15, 473.15, and 573.15) K, *The Journal of Chemical Thermodynamics*, **28** (**1996**) 521-538.

[30] J. Moore, F. Keyes, J. Keenan, P. Hill, Steam tables. Thermodynamic properties of water including vapor, liquid, and solid phases, in, *John Wiley & Sons, Inc.:* New York, **1969**.

[31] R. Schmidt, W. Wagner, A new form of the equation of state for pure substances and its application to oxygen, *Fluid Phase Equilibria*, **19** (**1985**) 175-200.

[32] R. Span, E.W. Lemmon, R.T. Jacobsen, W. Wagner, A. Yokozeki, A reference equation of state for the thermodynamic properties of nitrogen for temperatures from 63.151 to 1000 K and pressures to 2200 MPa, *Journal of Physical and Chemical Reference Data*, **29** (**2000**) 1361-1433.

[33] R. Span, W. Wagner, A new equation of state for carbon dioxide covering the fluid region from the triple-point temperature to 1100 K at pressures up to 800 MPa, *Journal of Physical and Chemical Reference Data*, **25** (**1996**) 1509-1596.

[34] C. Tegeler, R. Span, W. Wagner, A new equation of state for argon covering the fluid region for temperatures from the melting line to 700 K at pressures up to 1000 MPa, *Journal of Physical and Chemical Reference Data*, **28** (**1999**) 779-850.

[35] E.W. Lemmon, M.O. McLinden, W. Wagner, Thermodynamic properties of propane. III. A reference equation of state for temperatures from the melting line to 650 K and pressures up to 1000 MPa, *Journal of Chemical & Engineering Data*, **54** (**2009**) 3141-3180.

[36] U. Setzmann, W. Wagner, A new equation of state and tables of thermodynamic properties for methane covering the range from the melting line to 625 K at pressures up to 100 MPa, *Journal of Physical and Chemical Reference Data*, **20** (**1991**) 1061-1155.

[37] O. Kunz, W. Wagner, The gerg - 2008 wide-range equation of state for natural gases and other mixtures: An expansion of GERG-2004, *Journal of Chemical & Engineering data*, **57** (**2012**) 3032-3091.

[38] Anton Paar, Instruction manual. DMA-HPM density measuring cell for high pressure and high temperarures, Graz, Austria, **2006**.

[39] E. Lemmon, M. Huber, M. McLinden, Refprop: Reference fluid thermodynamic and transport properties, *NIST standard reference database*, **23** (**2007**).

[40] I.D. Mantilla, D.E. Cristancho, S. Ejaz, K.R. Hall, M. Atilhan, G.A. Iglesias-Silva, *P-ρ-t* data for carbon dioxide from (310 to 450) K up to 160 MPa, *Journal of Chemical & Engineering Data*, **55** (**2010**) 4611-4613.

[41] D.E. Cristancho, I.D. Mantilla, S. Ejaz, K.R. Hall, M. Atilhan, G.A. Iglesias-Silva, Accurate *ρpt* data for ethane from (298 to 450) K up to 200 MPa, *Journal of Chemical & Engineering Data*, **55** (**2010**) 2746-2749.

[42] D. Bücker, W. Wagner, A reference equation of state for the thermodynamic properties of ethane for temperatures from the melting line to 675 K and pressures up to 900 MPa, *Journal of Physical and Chemical Reference Data*, **35** (**2006**) 205-266.

[43] P.T. Eubank, K.R. Hall, Optimum mixture compositions for measurement of cross virial coefficients, *AIChE Journal*, **36** (**1990**) 1661-1668.

[44] E. Thiele, Equation of state for hard spheres, *The Journal of Chemical Physics*, **39** (**1963**) 474-479.

[45] K.H. Kumar, K.E. Starling, The most general density-cubic equation of state: Application to pure nonpolar fluids, *Industrial & Engineering Chemistry Fundamentals*, **21** (**1982**) 255-262.

[46] U. Setzmann, W. Wagner, A new method for optimizing the structure of thermodynamic correlation equations, *International Journal of Thermophysics*, **10** (**1989**) 1103-1126.

[47] P. Nowak, R. Kleinrahm, W. Wagner, Measurement and correlation of the (*p,ρ,T*) relation of nitrogen. I. The homogeneous gas and liquid regions in the temperature range from 66 K to 340 K at pressures up to 12 MPa, *The Journal of Chemical Thermodynamics*, **29** (**1997**) 1137-1156.

[48] R. Gilgen, R. Kleinrahm, W. Wagner, Measurement and correlation of the (pressure, density, temperature) relation of argon I. The homogeneous gas and liquid regions in the temperature range from 90 K to 340 K at pressures up to 12 MPa, *The Journal of Chemical Thermodynamics*, **26** (**1994**) 383-398.

[49] P.M. Mathias, M.S. Benson, Computational aspects of equations of state: Fact and fiction, *AIChE Journal*, **32** (**1986**) 2087-2090.

[50] A. Koziol, Quintic equation of state for pure substances in sub- and supercritical range, *Fluid Phase Equilibria*, **263** (**2008**) 18-25.

[51] P.T. Eubank, K.R. Hall, New identities for critical-point constraints with application to cubic equations of state, *Industrial & Engineering Chemistry Research*, **43** (**2004**) 4446-4451.

[52] P.B. Boogs, R, J. Rogers, R. Schabel, Reference guide for odrpack version 2.01 software for weighted ortogonal regression, in, **1992**.

[53] J. Klimeck, R. Kleinrahm, W. Wagner, An accurate single-sinker densimeter and measurements of the (*p,ρ,T*) relation of argon and nitrogen in the temperature range from (235 to 520) K at pressures up to 30 MPa, *The Journal of Chemical Thermodynamics*, **30** (**1998**) 1571-1588.

[54] G.C. Straty, D.E. Diller, (*p,v,T*) of saturated and compressed fluid nitrogen, *The Journal of Chemical Thermodynamics*, **12** (**1980**) 927-936.

[55] S.L. Robertson, S.E. Babb, Isotherms of nitrogen to 400°C and 10 000 bar, *The Journal of Chemical Physics*, **50** (**1969**) 4560-4564.

[56] P. Nowak, R. Kleinrahm, W. Wagner, Measurement and correlation of the (*p,ρ,T*) relation of nitrogen. II. Saturated-liquid and saturated-vapour densities and vapour

pressures along the entire coexistence curve, *The Journal of Chemical Thermodynamics*, **29** (**1997**) 1157-1174.

[57] M.F. Costa Gomes, J.P.M. Trusler, The speed of sound in nitrogen at temperatures between *T*=250 K and *T*=350 K and at pressures up to 30 MPa, *The Journal of Chemical Thermodynamics*, **30** (**1998**) 527-534.

[58] M.B. Ewing, J.P.M. Trusler, Second acoustic virial coefficients of nitrogen between 80 and 373 k, *Physica A: Statistical Mechanics and its Applications*, **184** (**1992**) 415-436.

[59] Boyes, The speed of sound in gases with application to equations of state and socin nozzles, *University of London*, **1992**.

[60] A.S. El-Hakeem, Velocity of sound in nitrogen and argon at high pressures, *The Journal of Chemical Physics*, **42** (**1965**) 3132-3133.

[61] S.S. Lestz, Acoustic isotherms for nitrogen, argon, and krypton, *The Journal of Chemical Physics*, **38** (**1963**) 2830-2834.

[62] B.A. Younglove, R.D. McCarty, Speed-of-sound measurements for nitrogen gas at temperatures from 80 to 350 K and pressures to 1.5 MPa, *The Journal of Chemical Thermodynamics*, **12** (**1980**) 1121-1128.

[63] M. Benedict, Pressure, volume, temperature properties of nitrogen at high density. I. Results obtained with a weight piezometer, *Journal of the American Chemical Society*, **59** (**1937**) 2224-2233.

[64] J.W. Magee, Molar heat capacity for saturated and compressed liquid and vapor nitrogen from 65 to 300 K at pressures to 35 MPa, *Journal of Research of the National Institute of Standards and Technology*, **96**.

[65] L.A. Weber, Measurements of the heat capacities cv of dense gaseous and liquid nitrogen and nitrogen trifluoride, *The Journal of Chemical Thermodynamics*, **13** (**1981**) 389-403.

[66] S.L. Robertson, S.E. Babb, G.J. Scott, Isotherms of argon to 10 000 bars and 400°C, *The Journal of Chemical Physics*, **50** (**1969**) 2160-2166.

[67] R. Gilgen, R. Kleinrahm, W. Wagner, Measurement and correlation of the (pressure, density, temperature) relation of argon II. Saturated-liquid and saturated-vapour densities and vapour pressures along the entire coexistence curve, *The Journal of Chemical Thermodynamics*, **26** (**1994**) 399-413.

[68] A.F. Estrada-Alexanders, J.P.M. Trusler, The speed of sound in gaseous argon at temperatures between 110 K and 450 K and at pressures up to 19 MPa, *The Journal of Chemical Thermodynamics*, **27** (**1995**) 1075-1089.

[69] E.F. Carome, C.B. Cykowski, J.F. Havlice, D.A. Swyt, Temperature and pressure dependence of the velocity of ultrasound in argon, *Physica*, **38** (**1968**) 307-311.

[70] J.J. Hurly, K.A. Gillis, J.B. Mehl, M.R. Moldover, The viscosity of seven gases measured with a greenspan viscometer, *International Journal of Thermophysics*, **24** (**2003**) 1441-1474.

[71] Y.L. Kachanov, B.É. Kanishchev, L.L. Pitaevskaya, Velocity of sound in argon and in helium-argon and nitrogen-carbon dioxide gas mixtures at high pressures, *Journal of Engineering Physics*, **44** (**1983**) 1-4.

[72] A. Lacam, Etude expérimentale de la propagation des ultrasons dans les fluides en fonction de la pression (1200 atmosphères) et de la température (200° c), *Impr. J. et R. Sennac*, **1956**

[73] M.A.R. Sharif, T.K. Groves, Apparatus for the measurement of decompression wave front velocity based sound speeds and of associated densities and isothermal compressibility coefficients in moderately dense gases, *Chemical Engineering Communications*, **86** (**1989**) 199-223.

[74] W.B. Streett, M.S. Constantino, Measurements of the velocity of sound in liquid argon from 90 to 160 K and pressures to 3400 atm, *Physica*, **75** (**1974**) 283-296.

[75] J. Thoen, E. Vangeel, W. Van Dael, Sound velocity measurements in liquid argon as a function of pressure and temperature, *Physica*, **45** (**1969**) 339-356.

[76] A. van Itterbeek, W. Grevendonk, W. van Dael, G. Forrez, Sound velocity measurements in liquid argon under high pressure, *Physica*, **25** (**1959**) 1255-1258.

[77] A. Van Itterbeek, W. Van Dael, The velocity of sound in liquid argonand liquid nitrogen at high pressures, *Cryogenics*, **1** (**1961**) 226-228.

[78] M. Anisimov, B. Koval'Chuk, B. Rabinovich, V. Smirnov, Experimental investigation of the isochoric heat capacity of argon over a wide range of parameters of state, including the critical points, *Thermophysical Properties of Matter and Substances*, **8** (**1975**).

[79] C. Gladun, The specific heat of liquid argon, *Cryogenics*, **11** (**1971**) 205-209.

[80] D.R. Douslin, R.H. Harrison, R.T. Moore, J.P. MuCullough, *Journal of Chemical & Engineering Data*, **9** (**1964**) 358-363.

[81] M. Jaeschke, H.M. Hinze, H.J. Achtermann, G. Magnus, *Pvt* data from burnett and refractive index measurements for the nitrogen—hydrogen system from 270 to 353 K and pressures to 30 MPa, *Fluid Phase Equilibria*, **62** (**1991**) 115-139.

[82] R. Kleinrahm, W. Duschek, W. Wagner, M. Jaeschke, Measurement and correlation of the (pressure, density, temperature) relation of methane in the temperature range from 273.15 K to 323.15 K at pressures up to 8 MPa, *The Journal of Chemical Thermodynamics*, **20** (**1988**) 621-631.

[83] N. Pieperbeck, R. Kleinrahm, W. Wagner, M. Jaeschke, Results of (pressure, density, temperature) measurements on methane and on nitrogen in the temperature range from 273.15 K to 323.15 K at pressures up to 12 MPa using a new apparatus for accurate gas-density measurements, *The Journal of Chemical Thermodynamics*, **23** (**1991**) 175-194.

[84] H.J. Achtermann, J. Hong, W. Wagner, A. Pruss, Refractive index and density isotherms for methane from 273 to 373 K and at pressures up to 34 MPa, *Journal of Chemical & Engineering Data*, **37** (**1992**) 414-418.

[85] G. Händel, R. Kleinrahm, W. Wagner, Measurements of the (pressure, density, temperature) relation of methane in the homogeneous gas and liquid regions in the temperature range from 100 K to 260 K and at pressures up to 8 MPa, *The Journal of Chemical Thermodynamics*, **24** (**1992**) 685-695.

[86] J. Klimeck, R. Kleinrahm, W. Wagner, Measurements of the(p,ρ,t) relation of methane and carbon dioxide in the temperature range 240 K to 520 K at pressures up to 30 MPa using a new accurate single-sinker densimeter, *The Journal of Chemical Thermodynamics*, **33** (**2001**) 251-267.

[87] P.J. Kortbeek, J.A. Schouten, Measurements of the compressibility and sound velocity in methane up to 1 gpa, revisited, *International Journal of Thermophysics*, **11** 455-466.

[88] W. Lemming, Fortschr-Ber, *Reine 6*, **19** (**1989**).

[89] J.P.M. Trusler, M. Zarari, The speed of sound and derived thermodynamic properties of methane at temperatures between 275 K and 375 K and pressures up to 10 MPa, *The Journal of Chemical Thermodynamics*, **24** (**1992**) 973-991.

[90] B. Younglov, Specific-heats, csigma, and cv, of compressed and liquefied methane, *Journal of Research of the National Bureau of Standards Section A-Physics and Chemistry*, (**1974**) 401-410.

[91] S. I. Sandier, H. Orbey, 9 mixing and combining rules, in: R.F.K.C.J.P. J.V. Sengers, H.J. White (Eds.) *Experimental thermodynamics*, *Elsevier*, **2000**, pp. 321-357.

[92] D.R. McGregor, J.C. Holste, P.T. Eubank, K.N. Marsh, K.R. Hall, J. Schouten, An interaction model for third virial coefficients which provides simplified equations for mixtures, *Fluid Phase Equilibria*, **35** (**1987**) 153-164.

[93] D.R. McGregor, J.C. Holste, P.T. Eubank, K.N. Marsh, K.R. Hall, Simple solution models applied to virial coefficients, *AIChE Journal*, **32** (**1986**) 1221-1223.

[94] E. Lemmon, R. Jacobsen, A generalized model for the thermodynamic properties of mixtures, *International journal of thermophysics*, **20** (**1999**) 825-835.

[95] A. Kreglewski, Equilibrium properties of fluids and fluid mixtures, **1984**.

APPENDIX A

A.1 Pressure Transducer Calibrations

Transducer Model	**420K-102**	**42K-101**
Pressure Range	0 to 20000 psia	0 to 2000 psia
Serial	118253	82703
Calibration date	06/2013	04/2012
Calibration Source	Paroscientific	Paroscientific/NIST
Temperature Coefficients		
U_o $[\mu sec]$	5.824821	5.873541
Y_1 $[\deg C / \mu sec]$	-3874.321	-3930.171
Y_2 $[\deg C / \mu \sec^2]$	-9116.728	-11485.22
$Y_3[\deg C / \mu \sec^3]$	0	0
Pressure Coefficients		
C_1 $[psia]$	-149069.2	-7273.990
C_2 $[psia / sec]$	-11428.76	346.9426
C_3 $[psia / \mu \sec^2]$	799775.9	18114.01
D_1	0.021083	0.050502
D_2	0	0
T_1	30.12706	30.18612
T_2	0.681343	1.516436
T_3	67.18435	47.20004
T_4	0	81.02094

Temperature Coefficients

$$X = Temperature\ period\ (\mu \sec)$$

$$U = X - U_o$$

Temperature: degC

$$Temp = Y_1 U + Y_2 U^2 + Y_3 U^3$$

Pressure Coefficients

$$T = pressure\ period\ (\mu sec)$$

$$C = C_1 + C_2 U + C_3 U^2$$

$$D = D_1 + D_2 U$$

$$T_o = T_1 + T_2 U + T_3 U^2 + T_4 U^3$$

Pressure: (psia)

$$p = C\left(1 - \frac{T_o^2}{T^2}\right)\left(1 - D\left(1 - \frac{T_0^2}{T^2}\right)\right)$$

A.2 SPRT Calibration (ITS-90 Coefficients)

The International Temperature Scale (ITS-90) can characterize the absolute thermodynamic scale in the range of 0.65 K to 1358 K. It expresses the temperature in term of the ratio of the measure resistance of the PRT at the triple point of water (R_0).

$$W = R(T) / R_o$$

For the 5686-B Glass capsule SPRT with a temperature range of -260 °C to 232 °C, the ratio of resistance needs a correction as following equation shows.

$$W_r = W + a_9 \left(W - 1\right) + b_9 \left(W - 1\right)^2$$

Following equation shows temperature expressed in Kelvin as a function of corrected ratio resistance using coefficients in Report no. B3820054 provided by Fluke®.

$$T_{90} = D_0 + \sum_{i=1}^{9} D_i \left((W_r - 2.64) / 1.64\right)^i + 273.15$$

ITS-90 Coefficients	
R_0	25.40652
a_9	4.79703634e-04
b_9	2.04471571e-05
D_0	439.932854
D_1	472.418020
D_2	37.684494
D_3	7.472018
D_4	2.920828
D_5	0.005184
D_6	-0.963864
D_7	0.188732
D_8	0.191203
D_9	0.049025

A.3 RTD Calibrations (Callendar-Van Dusen Equation)

For temperature: 0°C <T<661°C. Following calibration information was provided by OMEGA® by 01/2013.

$$R_T = R_0\left(1 + AT + BT^2\right)$$

RTD Omega Class B	
R_o [Ω]	100.50359
A	3.559852e-03
B	0

APPENDIX B

Table B.1 Nitrogen calibration data

T/K	p/MPa	τ / μs	τ_o / μs	ρ_{EoS} / kg·m^{-3}
		T = 473 K		
473.353	129.846	2708.267	2666.430	489.85
473.347	137.859	2709.526	2666.427	504.38
473.320	129.810	2708.247	2666.417	489.81
473.322	119.835	2706.578	2666.418	470.51
473.318	110.044	2704.812	2666.416	450.09
473.306	100.000	2702.850	2666.411	427.38
473.308	89.797	2700.683	2666.412	402.17
473.318	79.935	2698.398	2666.416	375.38
473.322	69.893	2695.843	2666.418	345.23
473.313	60.062	2693.003	2666.414	312.38
473.317	49.955	2689.770	2666.416	274.48
473.312	39.932	2686.149	2666.414	232.00
473.308	29.900	2682.040	2666.412	183.73
473.303	20.012	2677.448	2666.410	129.77
473.300	10.032	2672.226	2666.409	68.40
		T = 405 K		
405.503	137.636	2687.432	2641.122	549.98
405.503	130.049	2686.271	2641.122	536.43
405.502	119.901	2684.612	2641.121	517.03
405.516	109.691	2682.807	2641.127	495.79
405.520	99.880	2680.914	2641.128	473.49
405.519	89.850	2678.793	2641.128	448.43
405.520	80.053	2676.513	2641.128	421.28
405.520	69.721	2673.817	2641.128	389.18
405.519	59.930	2670.898	2641.128	354.74
405.518	49.922	2667.513	2641.127	314.54
405.517	39.965	2663.636	2641.127	268.36
405.513	29.633	2658.949	2641.125	212.51
405.510	19.993	2653.868	2641.124	151.93
405.504	9.617	2647.588	2641.122	77.09

Table B.1 Continued

T/K	p/MPa	τ / μs	τ_o / μs	ρ_{EoS} / kg·m^{-3}
		T = 370 K		
370.503	129.108	2675.501	2628.523	562.29
370.507	137.578	2676.771	2628.524	577.20
370.505	129.811	2675.608	2628.523	563.56
370.504	120.004	2674.039	2628.523	545.09
370.502	109.941	2672.291	2628.522	524.47
370.500	100.028	2670.414	2628.522	502.19
370.495	89.934	2668.305	2628.520	477.12
370.493	79.986	2665.993	2628.519	449.53
370.492	70.055	2663.401	2628.518	418.47
370.490	60.002	2660.390	2628.518	382.57
370.490	49.936	2656.912	2628.518	340.93
370.492	39.952	2652.874	2628.518	292.48
370.489	29.989	2648.108	2628.517	235.26
370.484	20.070	2642.492	2628.516	167.81
370.484	10.076	2635.908	2628.516	88.75
		T = 336 K		
335.757	129.846	2665.534	2616.246	593.99
335.752	137.697	2666.670	2616.244	607.41
335.751	130.072	2665.568	2616.244	594.39
335.749	119.956	2663.999	2616.243	575.83
335.748	110.044	2662.328	2616.243	555.99
335.747	99.997	2660.474	2616.242	533.87
335.746	89.946	2658.417	2616.242	509.28
335.744	80.027	2656.146	2616.242	482.05
335.743	69.981	2653.538	2616.241	450.71
335.743	59.992	2650.552	2616.241	414.74
335.750	49.990	2647.053	2616.244	372.47
335.746	39.985	2642.874	2616.242	321.98
335.744	29.977	2637.813	2616.241	260.74
335.741	19.977	2631.661	2616.240	186.31
335.743	9.999	2624.372	2616.241	98.16

Table B.1 Continued

T/K	p/MPa	τ / μs	τ_o / μs	ρ_{EoS} / kg·m^{-3}
		T = 304 K		
304.163	128.808	2656.735	2605.408	622.77
304.163	137.857	2658.001	2605.408	637.76
304.161	129.998	2656.908	2605.408	624.81
304.158	120.000	2655.417	2605.407	607.08
304.156	109.973	2653.790	2605.406	587.64
304.154	99.985	2652.009	2605.405	566.30
304.153	90.040	2650.042	2605.405	542.64
304.152	80.011	2647.812	2605.404	515.75
304.157	69.988	2645.269	2605.406	484.97
304.155	60.031	2642.334	2605.406	449.39
304.153	50.052	2638.846	2605.405	406.98
304.152	39.978	2634.559	2605.405	354.80
304.151	29.980	2629.257	2605.404	290.20
304.149	20.001	2622.600	2605.404	209.09
304.147	10.022	2614.471	2605.403	110.16

Table B.2 Argon calibration data

T/K	p/MPa	τ / μs	τ_o / μs	ρ_{EoS} / kg·m^{-3}
		T = 473 K		
473.343	130.306	2734.162	2666.419	800.72
473.342	137.586	2736.070	2666.419	823.15
473.339	129.827	2734.030	2666.417	799.20
473.341	119.873	2731.242	2666.418	766.38
473.327	109.946	2728.233	2666.413	730.98
473.322	99.889	2724.924	2666.411	691.97
473.338	89.928	2721.351	2666.417	649.70
473.335	79.924	2717.404	2666.416	603.05
473.331	69.926	2713.074	2666.414	551.53
473.357	59.961	2708.245	2666.424	494.49
473.362	50.042	2702.897	2666.426	431.28
473.362	39.893	2696.807	2666.426	359.12
473.357	29.865	2690.114	2666.424	279.78
473.338	19.841	2682.728	2666.417	192.46
473.329	9.973	2674.846	2666.414	99.39

Table B.2 Continued

T/K	p/MPa	τ / μs	τ_o / μs	ρ_{EoS} / kg·m^{-3}
		T = 405 K		
404.629	131.421	2715.068	2640.760	891.58
404.627	137.728	2716.653	2640.759	910.51
404.624	129.498	2714.566	2640.758	885.63
404.584	119.810	2711.920	2640.743	854.19
404.580	109.949	2709.005	2640.742	819.30
404.578	100.040	2705.797	2640.741	780.86
404.578	89.854	2702.154	2640.741	737.11
404.576	79.887	2698.189	2640.740	689.34
404.573	70.049	2693.779	2640.739	636.36
404.570	59.895	2688.620	2640.738	574.33
404.566	49.858	2682.783	2640.737	504.18
404.561	39.940	2676.174	2640.735	424.70
404.557	29.913	2668.535	2640.734	332.86
404.556	19.963	2659.987	2640.733	230.22
404.556	10.014	2650.624	2640.733	118.12
		T = 369 K		
368.972	130.428	2705.775	2627.915	941.49
368.974	137.821	2707.578	2627.916	963.17
368.972	130.050	2705.680	2627.915	940.34
368.970	120.027	2703.049	2627.914	908.63
368.971	109.557	2700.038	2627.915	872.29
368.974	100.053	2697.026	2627.916	835.91
368.974	89.999	2693.497	2627.916	793.19
368.976	80.124	2689.606	2627.917	746.04
368.974	70.313	2685.224	2627.916	692.92
368.973	59.995	2679.922	2627.915	628.62
368.972	49.974	2673.921	2627.915	555.82
368.974	39.994	2666.915	2627.916	470.87
368.981	30.039	2658.735	2627.918	371.72
369.001	19.861	2649.103	2627.926	255.13
368.989	9.991	2638.780	2627.921	130.59

Table B.2 Continued

T/K	p/MPa	τ / μs	τ_o / μs	ρ_{EoS} / kg·m^{-3}
		T = 335 K		
334.635	130.069	2697.707	2615.851	997.16
334.642	137.731	2699.495	2615.853	1018.81
334.640	129.959	2697.682	2615.853	996.83
334.638	119.904	2695.152	2615.852	966.15
334.636	110.029	2692.434	2615.851	933.10
334.635	99.982	2689.379	2615.851	895.90
334.634	89.992	2685.985	2615.851	854.53
334.633	80.014	2682.157	2615.850	807.76
334.633	70.042	2677.766	2615.850	754.11
334.634	60.084	2672.653	2615.851	691.64
334.632	49.665	2666.288	2615.850	613.83
334.645	39.889	2659.091	2615.854	525.75
334.641	30.026	2650.325	2615.853	418.72
334.637	19.963	2639.718	2615.852	289.41
334.641	10.012	2627.971	2615.853	146.62
		T = 304 K		
303.641	130.071	2691.144	2605.231	1053.69
303.636	137.701	2692.829	2605.229	1074.23
303.633	137.959	2692.883	2605.228	1074.90
303.629	129.991	2691.125	2605.227	1053.48
303.622	119.780	2688.692	2605.224	1023.81
303.622	109.853	2686.102	2605.224	992.09
303.620	99.773	2683.188	2605.224	956.38
303.618	89.899	2679.992	2605.223	917.13
303.616	80.057	2676.380	2605.222	872.71
303.615	69.891	2672.064	2605.222	819.61
303.615	59.881	2667.032	2605.222	757.78
303.613	49.907	2660.982	2605.221	683.23
303.612	40.019	2653.552	2605.221	591.69
303.610	30.038	2644.100	2605.220	475.35
303.607	19.409	2631.523	2605.219	320.89
303.607	10.012	2618.796	2605.219	165.26

Table B.3 Methane calibration data

T/K	p/MPa	τ / μs	τ_o / μs	ρ_{EoS} / kg·m^{-3}
		T = 470 K		
470.132	123.206	2689.529	2665.188	281.89
470.124	137.782	2690.728	2665.185	295.25
470.110	137.817	2690.725	2665.179	295.28
470.115	120.838	2689.313	2665.181	279.57
470.108	103.075	2687.600	2665.179	260.36
470.114	86.372	2685.701	2665.181	238.77
470.133	70.173	2683.487	2665.188	213.21
470.132	55.425	2680.988	2665.188	184.34
470.100	41.267	2677.987	2665.175	149.60
470.089	31.472	2675.479	2665.171	120.42
470.070	19.602	2671.913	2665.164	78.85
470.054	9.325	2668.439	2665.158	38.33
470.101	9.291	2668.446	2665.176	38.19
		T = 399 K		
398.975	122.339	2665.084	2638.711	310.22
398.966	137.838	2666.267	2638.707	323.53
398.962	121.101	2664.979	2638.706	309.09
398.958	103.674	2663.421	2638.705	291.49
398.953	86.506	2661.590	2638.703	270.54
398.965	68.568	2659.214	2638.707	242.85
398.961	55.185	2656.942	2638.706	216.24
398.971	41.055	2653.825	2638.709	179.43
398.970	30.993	2650.946	2638.709	145.34
398.958	19.404	2646.793	2638.705	96.11
398.964	10.395	2643.072	2638.707	51.89
398.988	10.397	2643.081	2638.715	51.90

Table B.3 Continued

T/K	p/MPa	τ / μs	τ_o / μs	ρ_{EoS} / kg·m^{-3}
		T = 304 K		
304.106	121.936	2635.171	2605.402	357.43
304.112	137.748	2636.184	2605.404	368.85
304.110	119.972	2635.038	2605.403	355.90
304.108	99.943	2633.529	2605.403	338.60
304.104	79.950	2631.669	2605.401	316.97
304.104	70.181	2630.565	2605.401	303.97
304.103	59.973	2629.200	2605.401	287.81
304.101	50.009	2627.562	2605.400	268.28
304.099	40.034	2625.437	2605.400	242.79
304.104	29.784	2622.367	2605.401	205.70
304.101	20.052	2617.919	2605.400	151.76
304.103	10.047	2611.504	2605.401	73.83
304.103	10.047	2611.504	2605.401	73.83

Table B.4 Experimental (p-ρ-T) values for carbon dioxide

T/K	p/MPa	ρ_{exp} / kg·m^{-3}	ρ_{EoS} / kg·m^{-3}	$100(\rho_{exp}-\rho_{EoS})/\rho_{exp}$
		T = 304 K		
304.303	119.826	1148.82	1149.13	-0.027
304.304	136.467	1169.87	1170.20	-0.028
304.300	104.549	1127.06	1127.47	-0.036
304.297	86.449	1097.67	1097.98	-0.028
304.293	69.065	1063.89	1064.08	-0.017
304.290	56.603	1034.73	1034.73	0.000
304.287	42.233	992.73	992.44	0.030
304.285	31.385	950.66	950.15	0.054
304.294	21.349	895.09	894.61	0.054
304.294	10.390	768.95	768.89	0.008
		T = 399 K		
398.610	118.142	975.99	975.55	0.044
398.617	137.833	1012.46	1012.04	0.041
398.619	119.829	979.32	978.92	0.041
398.614	103.727	944.72	944.24	0.050
398.610	86.718	900.46	900.06	0.044
398.613	70.281	846.15	845.85	0.036
398.609	52.521	764.26	764.02	0.032
398.616	36.685	645.59	645.24	0.054
398.616	36.789	646.63	646.28	0.053
398.602	20.324	391.90	391.67	0.059
		T = 470 K		
469.763	116.457	861.27	860.52	0.087
469.759	137.604	908.75	907.90	0.094
469.738	103.717	827.38	826.75	0.076
469.735	103.847	827.75	827.13	0.075
469.748	86.961	773.96	773.46	0.065
469.740	69.479	702.01	701.57	0.062
469.729	54.964	621.41	620.95	0.074
469.777	36.325	466.70	466.53	0.036
469.775	20.740	272.48	272.60	-0.042

Table B.5 Experimental (p-ρ-T) values for ethane

T/K	p/MPa	ρ_{exp} / kg·m^{-3}	ρ_{EoS} / kg·m^{-3}	$100(\rho_{exp}-\rho_{EoS})/\rho_{exp}$
		T = 304 K		
304.306	120.907	532.80	532.90	-0.019
304.303	137.643	542.63	542.77	-0.026
304.300	113.927	528.42	528.47	-0.010
304.299	103.841	521.63	521.65	-0.002
304.297	86.990	509.02	508.94	0.014
304.295	69.715	494.00	493.61	0.079
304.294	56.004	479.29	478.99	0.063
304.300	41.974	460.60	460.41	0.041
304.299	30.964	441.74	441.49	0.055
304.299	20.724	417.38	417.13	0.059
304.299	10.173	372.80	372.51	0.078
		T = 399 K		
399.011	123.093	479.22	478.86	0.077
399.014	136.122	489.14	488.78	0.073
399.025	120.965	477.50	477.13	0.078
399.005	103.351	462.05	461.62	0.094
399.002	86.735	444.78	444.25	0.119
399.002	69.356	422.40	421.74	0.156
399.001	55.861	399.66	399.28	0.096
399.004	42.071	368.25	368.08	0.046
399.006	30.973	330.57	330.51	0.018
399.000	20.736	270.05	269.92	0.048
399.004	10.202	130.49	130.47	0.019
		T = 470 K		
469.996	120.161	439.65	439.16	0.111
469.992	125.610	444.69	444.23	0.104
469.966	137.417	454.98	454.45	0.116
469.956	105.448	424.56	424.14	0.098
469.967	86.507	401.16	400.87	0.071
469.968	70.405	376.04	375.81	0.060
469.969	55.719	346.04	345.82	0.066
469.982	41.149	303.71	303.54	0.057
469.961	31.179	260.81	260.56	0.098
469.948	21.121	194.69	194.50	0.099
469.938	10.882	98.22	98.02	0.200

Table B.6 Experimental (p-ρ-T) values for 25% Methane – 75% Nitrogen Mixture

T/K	p/MPa	ρ_{exp} / kg·m^{-3}	ρ_{EoS} / kg·m^{-3}	$100(\rho_{exp}-\rho_{EoS})/\rho_{exp}$
		T = 304 K		
304.170	119.970	543.01	542.75	0.047
304.170	137.644	568.44	568.13	0.055
304.162	119.475	542.25	541.99	0.047
304.160	100.150	509.22	509.00	0.043
304.155	80.085	466.50	466.35	0.031
304.157	69.944	440.11	439.99	0.028
304.156	60.032	409.84	409.73	0.028
304.154	49.960	372.83	372.73	0.027
304.154	40.008	327.46	327.39	0.022
304.160	29.009	262.61	262.54	0.027
304.156	20.038	194.30	194.20	0.052
304.154	10.026	101.09	100.96	0.135
		T = 350 K		
350.052	119.603	503.31	503.04	0.054
349.911	137.330	530.55	530.19	0.068
350.005	120.082	504.14	503.86	0.056
350.022	99.993	467.88	467.67	0.045
350.021	80.012	423.20	423.06	0.033
350.020	69.941	395.97	395.87	0.025
350.022	60.017	364.90	364.83	0.019
350.023	49.997	327.90	327.85	0.014
350.028	39.994	283.49	283.46	0.009
350.026	29.993	229.32	229.30	0.012
350.034	20.016	163.38	163.33	0.031
350.034	10.009	85.31	85.22	0.099

Table B.6 Continued

T/K	p/MPa	ρ_{exp} / kg·m^{-3}	ρ_{EoS} / kg·m^{-3}	$100(\rho_{exp}-\rho_{EoS})/\rho_{exp}$
		T = 400 K		
399.916	120.219	467.40	467.24	0.034
399.912	137.620	494.98	494.73	0.050
399.898	120.086	467.18	467.03	0.032
399.891	100.077	429.90	429.83	0.017
399.885	80.004	384.10	384.09	0.000
399.883	69.977	356.85	356.87	-0.004
399.882	60.031	325.98	326.02	-0.013
399.885	49.831	289.34	289.39	-0.016
399.873	39.948	247.77	247.83	-0.022
399.857	30.038	198.74	198.77	-0.013
399.861	19.996	140.32	140.31	0.009
399.867	10.013	73.52	73.49	0.051
		T = 470 K		
469.864	120.802	424.87	424.82	0.013
469.865	137.596	452.08	451.96	0.026
469.903	119.671	422.86	422.84	0.004
469.886	99.985	385.63	385.65	-0.006
469.879	80.110	340.44	340.55	-0.032
469.892	69.961	313.52	313.63	-0.036
469.885	59.957	283.71	283.84	-0.045
469.883	49.999	250.17	250.30	-0.054
469.890	40.040	212.00	212.12	-0.054
469.900	30.012	168.09	168.16	-0.045
469.916	20.020	118.12	118.21	-0.078
469.909	10.004	61.80	61.84	-0.067

Table B.7 Experimental (p-ρ-T) values for 50% Methane – 50% Nitrogen Mixture

T/K	p/MPa	ρ_{exp} / kg·m^{-3}	ρ_{EoS} / kg·m^{-3}	$100(\rho_{exp}-\rho_{EoS})/\rho_{exp}$
		T = 304 K		
304.320	119.878	480.29	479.73	0.117
304.317	137.784	501.45	500.78	0.132
304.308	120.092	480.60	480.01	0.123
304.301	99.969	452.36	451.89	0.102
304.297	80.027	417.33	416.96	0.088
304.295	69.979	395.67	395.34	0.083
304.294	59.992	370.21	369.93	0.076
304.293	49.950	339.04	338.81	0.068
304.291	40.009	300.09	299.92	0.057
304.296	30.001	248.55	248.43	0.050
304.293	20.007	179.37	179.23	0.075
304.289	9.997	91.69	91.53	0.166
		T = 350 K		
349.847	120.005	446.62	446.00	0.138
349.849	137.830	469.21	468.46	0.159
349.847	120.023	446.64	446.03	0.138
349.844	99.951	416.45	415.94	0.121
349.845	79.968	378.82	378.52	0.080
349.841	70.033	356.12	355.86	0.075
349.840	59.961	329.19	328.97	0.065
349.839	50.006	297.37	297.21	0.052
349.841	40.010	258.28	258.21	0.029
349.837	29.954	209.28	209.23	0.025
349.833	20.028	149.00	148.95	0.036
349.831	9.961	76.43	76.37	0.072

Table B.7 Continued

T/K	p/MPa	ρ_{exp} / kg·m^{-3}	ρ_{EoS} / kg·m^{-3}	$100(\rho_{exp}-\rho_{EoS})/\rho_{exp}$
		T = 400 K		
399.904	120.559	414.70	414.22	0.115
399.909	137.807	437.67	437.03	0.148
399.905	120.026	413.98	413.46	0.125
399.900	100.082	382.51	382.19	0.084
399.904	79.818	343.04	342.84	0.058
399.913	69.931	319.87	319.72	0.046
399.914	59.961	292.96	292.88	0.028
399.920	49.865	261.11	261.07	0.017
399.917	39.952	224.03	224.02	0.003
399.912	29.983	179.50	179.51	-0.006
399.915	19.922	126.11	126.10	0.012
399.913	9.988	65.56	65.51	0.067
399.924	9.987	65.54	65.51	0.053
		T = 470 K		
470.004	119.844	374.90	374.59	0.084
470.019	137.925	399.92	399.47	0.112
470.021	119.963	375.09	374.76	0.089
470.063	100.025	342.70	342.57	0.038
470.010	80.022	303.46	303.42	0.014
469.998	69.917	280.09	280.08	0.004
469.994	60.016	254.20	254.21	-0.006
469.987	49.973	224.25	224.31	-0.024
469.982	40.008	190.16	190.21	-0.029
469.977	29.966	150.62	150.63	-0.007
469.973	19.923	105.29	105.27	0.018
469.973	9.992	54.93	54.91	0.031

Table B.8 Experimental (p-ρ-T) values for 75% Methane – 25% Nitrogen Mixture

T/K	p/MPa	ρ_{exp} / kg·m^{-3}	ρ_{EoS} / kg·m^{-3}	$100(\rho_{exp}-\rho_{EoS})/\rho_{exp}$
		T = 304 K		
304.114	120.278	418.82	418.39	0.102
304.115	137.680	435.25	434.73	0.118
304.103	119.811	418.39	417.92	0.112
304.100	100.110	396.33	395.91	0.106
304.097	80.054	368.16	367.83	0.091
304.096	69.976	350.71	350.42	0.081
304.096	59.950	330.09	329.83	0.079
304.096	49.895	304.63	304.41	0.071
304.094	39.907	272.08	271.92	0.062
304.092	29.972	228.08	227.94	0.063
304.089	19.971	165.17	165.04	0.082
304.097	9.981	82.59	82.45	0.178
		T = 350 K		
349.917	119.772	388.99	388.61	0.099
349.918	137.872	407.63	407.12	0.126
349.915	119.963	389.22	388.82	0.103
349.913	99.975	364.75	364.46	0.082
349.897	79.983	334.02	333.86	0.049
349.899	69.727	314.65	314.53	0.039
349.901	59.941	292.83	292.75	0.025
349.899	50.031	266.14	266.11	0.009
349.898	39.935	232.26	232.24	0.009
349.896	30.048	189.70	189.71	-0.006
349.891	20.006	134.29	134.27	0.009
349.888	10.027	68.31	68.27	0.053

Table B.8 Continued

T/K	p/MPa	ρ_{exp} / kg·m^{-3}	ρ_{EoS} / kg·m^{-3}	$100(\rho_{exp}-\rho_{EoS})/\rho_{exp}$
		T = 400 K		
399.862	118.835	359.57	359.31	0.071
399.878	137.873	380.53	380.13	0.103
399.878	119.993	361.01	360.67	0.094
399.877	100.029	335.02	334.82	0.059
399.872	79.995	302.54	302.47	0.023
399.882	70.064	283.02	282.98	0.014
399.881	59.988	260.00	259.98	0.008
399.881	50.075	233.16	233.17	-0.003
399.886	40.061	200.52	200.55	-0.013
399.868	30.067	160.90	160.92	-0.010
399.859	20.006	112.82	112.78	0.037
399.862	9.992	57.76	57.72	0.067
		T = 470 K		
469.886	119.899	326.99	326.83	0.048
469.883	137.448	347.30	346.99	0.089
469.876	120.092	327.26	327.07	0.057
469.877	99.995	299.96	299.91	0.019
469.862	80.021	266.76	266.78	-0.008
469.863	69.975	246.91	246.94	-0.011
469.854	59.945	224.29	224.35	-0.025
469.843	50.010	198.54	198.59	-0.026
469.835	39.994	168.40	168.45	-0.028
469.874	29.908	133.12	133.11	0.004
469.838	20.016	93.29	93.24	0.053
469.851	10.026	48.26	48.22	0.096

APPENDIX C

The Helmholtz energy and their derivatives can describe all thermodynamic properties. Appendix C contains mathematical expressions for first and second derivatives using a REOS based upon residual Helmholtz energies. The functional for the residual energy is:

$$\alpha^r = \frac{f(\delta,\tau)}{g(\delta,\tau)} = \frac{N_1(\tau)\delta + N_2(\tau)\delta^2 + N_3(\tau)\delta^3 + N_4(\tau)\delta^4 + N_5(\tau)\delta^5 + N_6(\tau)\delta^6}{1 + D_1(\tau)\delta + D_2(\tau)\delta^2 + D_3(\tau)\delta^3}$$

First and second derivatives in density of the residual Helmholtz energy, using numerator and denominator abbreviations are:

$$\alpha^r_\delta = \frac{f_\delta g - f g_\delta}{g^2}$$

$$\alpha^r_{\delta\delta} = \frac{f_{\delta\delta} g^2 - g g_{\delta\delta} f - 2 g_\delta (f_\delta g - g_\delta f)}{g^3}$$

First and second derivatives in temperature of the residual Helmholtz energy, using numerator and denominator abbreviations are:

$$\alpha^r_\tau = \frac{f_\tau g - f g_\tau}{g^2}$$

$$\alpha^r_{\tau\tau} = \frac{f_{\tau\tau} g^2 - g g_{\tau\tau} f - 2 g_\tau (f_\tau g - g_\tau f)}{g^3}$$

Temperature and density cross derivative terms for the residual Helmholtz energy, using numerator and denominator abbreviations are:

$$\alpha_{\delta\tau}^{r} = \frac{f_{\delta\tau}g^2 + gg_{\tau}f_{\delta} - g_{\delta\tau}gf - f_{\tau}gg_{\delta} - 2g_{\tau}\left(f_{\delta}g - g_{\delta}f\right)}{g^3}$$

Numerator and denominator expressions are polynomial functions in temperature, their first and second derivatives in temperature and density are:

$$f = \sum_{i=1}^{6} N_i \delta^i = \sum_{i=1}^{6}\sum_{j=0}^{4} c_{i,j}\,\tau^j \delta^i$$

$$g = 1 + \sum_{i=1}^{3} D_i \delta^i = 1 + \sum_{i=1}^{3}\sum_{j=0}^{4} b_{i,j}\,\tau^j \delta^i$$

$$f_{\delta} = \sum_{i=1}^{6} iN_i \delta^{i-1} = \sum_{i=1}^{6}\sum_{j=0}^{4} ic_{i,j}\,\tau^j \delta^{i-1}$$

$$g_{\delta} = \sum_{i=1}^{3} iD_i \delta^{i-1} = \sum_{i=1}^{3}\sum_{j=0}^{4} ib_{i,j}\,\tau^j \delta^{i-1}$$

$$f_{\delta\delta} = \sum_{i=1}^{6} i\left(i-1\right)N_i \delta^{i-2} = \sum_{i=1}^{6}\sum_{j=0}^{4} i\left(i-1\right)c_{i,j}\,\tau^j \delta^{i-2}$$

$$g_{\delta\delta} = \sum_{i=1}^{3} i\left(i-1\right)D_i \delta^{i-2} = \sum_{i=1}^{3}\sum_{j=0}^{4} i\left(i-1\right)b_{i,j}\,\tau^j \delta^{i-2}$$

$$f_{\delta\tau} = \sum_{i=1}^{6} iN_{i\tau} \delta^{i-1} = \sum_{i=1}^{6}\sum_{j=0}^{4} jic_{i,j}\,\tau^{j-1} \delta^{i-1}$$

$$g_{\delta\tau} = \sum_{i=1}^{3} iD_{i\tau} \delta^{i-1} = \sum_{i=1}^{3}\sum_{j=0}^{4} ijb_{i,j}\,\tau^{j-1} \delta^{i-1}$$

$$f_{\tau} = \sum_{i=1}^{6} N_{i\tau} \delta^{i} = \sum_{i=1}^{6}\sum_{j=0}^{4} jc_{i,j}\,\tau^{j-1} \delta^{i}$$

$$g_{\tau} = \sum_{i=1}^{3} D_{i\tau} \delta^{i} = \sum_{i=1}^{3}\sum_{j=0}^{4} jb_{i,j}\,\tau^{j-1} \delta^{i}$$

$$f_{\tau\tau} = \sum_{i=1}^{6} N_{i\tau\tau} \delta^{i} = \sum_{i=1}^{6}\sum_{j=0}^{4} j\left(j-1\right)c_{i,j}\,\tau^{j-2} \delta^{i}$$

$$g_{\tau\tau} = \sum_{i=1}^{3} D_{i\,\tau\tau}\delta^i = \sum_{i=1}^{3}\sum_{j=0}^{4} j\left(j-1\right)b_{i,j}\,\tau^{j-2}\delta^i$$

APPENDIX D

Appendix D shows a program code based upon c language and applied to Matlab®. This program is a least square non-linear minimization applied for pure components including vapor pressure, *p*-*ρ*-*T*, isochoric heat capacities and speed of sound data to calculate 45 coefficient parameters. The code reports parameters values, uncertainties and residual errors.

```
function Fit_lsq_from_Ar_Test1
format short e
%Critical Properties Nitrogen
rhoc=313.29996; %kg/m3
Tc=126.192;%K
Pc=3.3958; %Mpa
Mw=28.01348; % g/mol
R=8.3144621; % cm3?MPa?K?1?mol?1

Zg=[];Tg=[];Pg=[];delta=[];ww=[];

x0=[0.456973572646,-0.853394127907,-0.953626347522,0.305153203120,-
0.105507159375,-0.125756126572,1.315257162466,-
3.248502331899,3.053783442656,0.607130865840,0.089245956517,-
0.483899030770,0.611821783288,0.623334308226,-1.890070237787,-
0.006331746935,0.146238580012,-0.188824946279,-
0.341092704490,0.684653238956, -0.267886936762,1.022211537128,-
1.732746542637,-0.305501134060,0.082700215718,0.103709224974,-
0.276110260043,0.068640676190,0.847783598445,-0.077913662712,
0.003696964869, 0.051247696443,-0.055399981051,-0.105555878940,
0.013208424552, 0,-0.003940920558,-0.075349429828, 0.235204633831,-
0.206230692773, 0, 0.005653250420, 0.005041475387,-0.032543151544,
0.028756009973];

virial=importdata('virial_data.txt');
PV_data=importdata('VP_N2-density_3.txt');
CV_data=importdata('CV_data.txt');
w_data=importdata('speedofsound_data.txt');

TCv=CV_data(:,2)./Tc;
deltaCv=(CV_data(:,1)*Mw)./rhoc;
CV=CV_data(:,3);

SD=w_data(:,3);
Tw=w_data(:,2)./Tc;
deltaw=w_data(:,4)./rhoc;
Pw=w_data(:,1);
```

```
Tv=PV_data(:,1)./Tc;
Pv=PV_data(:,2);
rho_l=PV_data(:,3)./rhoc;
rho_v=PV_data(:,4)./rhoc;

rho_vp=[PV_data(:,4)]./Mw;
P_vp=[PV_data(:,2)];
T_vp=[PV_data(:,1)];
z_vp=P_vp./(R.*T_vp.*(rho_vp./1000));

for
i=[1,2,3,4,5,6,7,8,9,10,11,12,13,14,15,16,17,18,19,20,21,22,23,24,25,26
,27,28,29,30,31,32,33,34,35,36,19982,1969,2009]

D=importdata(['t' int2str(i) '.txt']);
rho=D(:,2); %Kmol/m^3
P=D(:,1); %Mpa
T=D(:,3); %Mpa

if i==19982
   rho=rho./Mw;
   ww=[ww;(1./0.002)*ones(size(T));];
elseif i==1969
   rho=rho./Mw;
   ww=[ww;(1./0.1)*ones(size(T));];
elseif i==2009
   rho=rho./Mw;
   ww=[ww;(1./0.02)*ones(size(T));];
elseif i<=22
    ww=[ww;(1./0.02)*ones(size(T));];
else
    ww=[ww;(1./0.008)*ones(size(T));];
end

z=P./(R.*T.*(rho./1000)); %dimensionless
rhored=(rho.*Mw)/(rhoc);%dimensionless
Pg=[Pg;P]; Zg=[Zg;z]; Tg=[Tg;T]; delta=[delta;rhored];
end

Pg=[Pg;P_vp];
Zg=[Zg;z_vp];
Tg=[Tg;T_vp];
delta=[delta;rho_vp.*Mw/rhoc];
ww_vp=(1./0.04)*ones(43,1);
ww=[ww;ww_vp];
Tvirial=(virial(:,1))./Tc;
B_data=(virial(:,2)./(Mw.*1000)).*rhoc;
C_data=(virial(:,3)./(Mw.*1000).^2).*rhoc.^2;
Tred=Tg./Tc;
```

```
options=optimset('TolFun',1E-20,'TolX',1E-
20,'MaxFunEvals',40000,'MaxIter',40000,'Algorithm','levenberg-
marquardt' );
[x,resnorm,residual,exitflag,output,lambda,jacobian] =
lsqnonlin(@functiongoal,x0,[],[],options,delta,Zg,Tred,ww,B_data,C_data
,Tvirial,Tv,Pv,rho_l,rho_v,SD,Tw,deltaw,TCv,deltaCv,CV);    % Invoke
optimizer

n1=x(1)+x(2)./Tred+x(3)./Tred.^2+x(4)./Tred.^3+x(5)./Tred.^4;
n2=x(6)+x(7)./Tred+x(8)./Tred.^2+x(9)./Tred.^3+x(10)./Tred.^4;
n3=x(11)+x(12)./Tred+x(13)./Tred.^2+x(14)./Tred.^3+x(15)./Tred.^4;
n4=x(16)+x(17)./Tred+x(18)./Tred.^2+x(19)./Tred.^3+x(20)./Tred.^4;
n5=x(36)+x(37)./Tred+x(38)./Tred.^2+x(39)./Tred.^3+x(40)./Tred.^4;
n6=x(41)+x(42)./Tred+x(43)./Tred.^2+x(44)./Tred.^3+x(45)./Tred.^4;
d1=x(21)+x(22)./Tred+x(23)./Tred.^2+x(24)./Tred.^3+x(25)./Tred.^4;
d2=x(26)+x(27)./Tred+x(28)./Tred.^2+x(29)./Tred.^3+x(30)./Tred.^4;
d3=x(31)+x(32)./Tred+x(33)./Tred.^2+x(34)./Tred.^3+x(35)./Tred.^4;

n1_v=x(1)+x(2)./Tvirial+x(3)./Tvirial.^2+x(4)./Tvirial.^3+x(5)./Tvirial
.^4;
d1_v=x(21)+x(22)./Tvirial+x(23)./Tvirial.^2+x(24)./Tvirial.^3+x(25)./Tv
irial.^4;
n2_v=x(6)+x(7)./Tvirial+x(8)./Tvirial.^2+x(9)./Tvirial.^3+x(10)./Tviria
l.^4;

B=n1_v;
C=2*(n2_v-n1_v.*d1_v);

f=n1.*delta+n2.*delta.^2+n3.*delta.^3+n4.*delta.^4+n5.*delta.^5+n6.*del
ta.^6;
g=1+d1.*delta+d2.*delta.^2+d3.*delta.^3;
f_delta=n1+2.*n2.*delta+3.*n3.*delta.^2+4.*n4.*delta.^3+5.*n5.*delta.^4
+6.*n6.*delta.^5;
g_delta=d1+2.*d2.*delta+3.*d3.*delta.^2;
alpha_delta=(f_delta.*g-g_delta.*f)./g.^2;

zcalc=1+delta.*(alpha_delta);
dev=((zcalc-Zg)./Zg)*100;
Pcalc=zcalc.*R.*Tg.*(delta.*rhoc)./(1000.*Mw);

hold on
plot(Tred,dev,'b*')

ci = nlparci(x,residual,'jacobian',jacobian);



function f = functiongoal(x,
delta,Zg,Tred,ww,B_data,C_data,Tvirial,Tv,Pv,rho_l,rho_v,SD,Tw,deltaw,T
Cv,deltaCv,CV)
```

```
n1=x(1)+x(2)./Tred+x(3)./Tred.^2+x(4)./Tred.^3+x(5)./Tred.^4;
n2=x(6)+x(7)./Tred+x(8)./Tred.^2+x(9)./Tred.^3+x(10)./Tred.^4;
n3=x(11)+x(12)./Tred+x(13)./Tred.^2+x(14)./Tred.^3+x(15)./Tred.^4;
n4=x(16)+x(17)./Tred+x(18)./Tred.^2+x(19)./Tred.^3+x(20)./Tred.^4;
n5=x(36)+x(37)./Tred+x(38)./Tred.^2+x(39)./Tred.^3+x(40)./Tred.^4;
n6=x(41)+x(42)./Tred+x(43)./Tred.^2+x(44)./Tred.^3+x(45)./Tred.^4;
d1=x(21)+x(22)./Tred+x(23)./Tred.^2+x(24)./Tred.^3+x(25)./Tred.^4;
d2=x(26)+x(27)./Tred+x(28)./Tred.^2+x(29)./Tred.^3+x(30)./Tred.^4;
d3=x(31)+x(32)./Tred+x(33)./Tred.^2+x(34)./Tred.^3+x(35)./Tred.^4;

f=n1.*delta+n2.*delta.^2+n3.*delta.^3+n4.*delta.^4+n5.*delta.^5+n6.*del
ta.^6;
g=1+d1.*delta+d2.*delta.^2+d3.*delta.^3;
f_delta=n1+2.*n2.*delta+3.*n3.*delta.^2+4.*n4.*delta.^3+5.*n5.*delta.^4
+6.*n6.*delta.^5;
g_delta=d1+2.*d2.*delta+3.*d3.*delta.^2;

alpha_delta=(f_delta.*g-g_delta.*f)./g.^2;

% %critical Constraint
zc=0.28938788471;
n1_c=x(1)+x(2)./1+x(3)./1.^2+x(4)./1.^3+x(5)./1.^4;
n2_c=x(6)+x(7)./1+x(8)./1.^2+x(9)./1.^3+x(10)./1.^4;
n3_c=x(11)+x(12)./1+x(13)./1.^2+x(14)./1.^3+x(15)./1.^4;
n4_c=x(16)+x(17)./1+x(18)./1.^2+x(19)./1.^3+x(20)./1.^4;
n5_c=x(36)+x(37)./1+x(38)./1.^2+x(39)./1.^3+x(40)./1.^4;
n6_c=x(41)+x(42)./1+x(43)./1.^2+x(44)./1.^3+x(45)./1.^4;
d1_c=x(21)+x(22)./1+x(23)./1.^2+x(24)./1.^3+x(25)./1.^4;
d2_c=x(26)+x(27)./1+x(28)./1.^2+x(29)./1.^3+x(30)./1.^4;
d3_c=x(31)+x(32)./1+x(33)./1.^2+x(34)./1.^3+x(35)./1.^4;

f_c=n1_c.*1+n2_c.*1.^2+n3_c.*1.^3+n4_c.*1.^4+n5_c.*1.^5+n6_c.*1.^6;
g_c=1+d1_c.*1+d2_c.*1.^2+d3_c.*1.^3;
f_delta_c=n1_c+2.*n2_c.*1+3.*n3_c.*1.^2+4.*n4_c.*1.^3+5.*n5_c.*1.^4+6.*
n6_c.*1.^5;
g_delta_c=d1_c+2.*d2_c.*1+3.*d3_c.*1.^2;

f_delta_2_c=2.*n2_c+6.*n3_c.*1+12.*n4_c.*1.^2+20.*n5_c.*1.^3+30.*n6_c.*
1.^4;
g_delta_2_c=2.*d2_c+6.*d3_c.*1;

alpha_delta_c=(f_delta_c.*g_c-g_delta_c.*f_c)./g_c.^2;
alpha_delta_2_c=(f_delta_2_c.*g_c-g_delta_2_c.*f_c-
2.*g_c.*g_delta_c.*alpha_delta_c)./g_c.^2;
alpha_delta_3_c=(120*n6_c*1^3 + 60*n5_c*1^2 + 24*n4_c*1 +
6*n3_c)/(d3_c*1^3 + d2_c*1^2 + d1_c*1 + 1) - (3*(3*d3_c*1^2 + 2*d2_c*1
+ d1_c)*(30*n6_c*1^4 + 20*n5_c*1^3 + 12*n4_c*1^2 + 6*n3_c*1 +
2*n2_c))/(d3_c*1^3 + d2_c*1^2 + d1_c*1 + 1)^2 - (3*(2*d2_c +
6*1*d3_c)*(6*n6_c*1^5 + 5*n5_c*1^4 + 4*n4_c*1^3 + 3*n3_c*1^2 + 2*n2_c*1
+ n1_c))/(d3_c*1^3 + d2_c*1^2 + d1_c*1 + 1)^2 - (6*d3_c*(n6_c*1^6 +
n5_c*1^5 + n4_c*1^4 + n3_c*1^3 + n2_c*1^2 + n1_c*1))/(d3_c*1^3 +
d2_c*1^2 + d1_c*1 + 1)^2 + (6*(3*d3_c*1^2 + 2*d2_c*1 +
```

```
d1_c)^2*(6*n6_c*1^5 + 5*n5_c*1^4 + 4*n4_c*1^3 + 3*n3_c*1^2 + 2*n2_c*1 +
n1_c))/(d3_c*1^3 + d2_c*1^2 + d1_c*1 + 1)^3 - (6*(3*d3_c*1^2 + 2*d2_c*1
+ d1_c)^3*(n6_c*1^6 + n5_c*1^5 + n4_c*1^4 + n3_c*1^3 + n2_c*1^2 +
n1_c*1))/(d3_c*1^3 + d2_c*1^2 + d1_c*1 + 1)^4 + (6*(2*d2_c +
6*1*d3_c)*(3*d3_c*1^2 + 2*d2_c*1 + d1_c)*(n6_c*1^6 + n5_c*1^5 +
n4_c*1^4 + n3_c*1^3 + n2_c*1^2 + n1_c*1))/(d3_c*1^3 + d2_c*1^2 + d1_c*1
+ 1)^3;

con1=zc-(1+alpha_delta_c);
con2=1+2.*1.*alpha_delta_c+1.^2*alpha_delta_2_c;
con3=2*alpha_delta_c+4*1*alpha_delta_2_c+1^2*alpha_delta_3_c;

%Vapor Pressure Data
R=8.3144621; % cm3?MPa?K?1?mol?1
rhoc=313.29996; %kg/m3
Tc=126.192;%K

Mw=28.01348; % g/mol
n1_PV=x(1)+x(2)./Tv+x(3)./Tv.^2+x(4)./Tv.^3+x(5)./Tv.^4;
n2_PV=x(6)+x(7)./Tv+x(8)./Tv.^2+x(9)./Tv.^3+x(10)./Tv.^4;
n3_PV=x(11)+x(12)./Tv+x(13)./Tv.^2+x(14)./Tv.^3+x(15)./Tv.^4;
n4_PV=x(16)+x(17)./Tv+x(18)./Tv.^2+x(19)./Tv.^3+x(20)./Tv.^4;
n5_PV=x(36)+x(37)./Tv+x(38)./Tv.^2+x(39)./Tv.^3+x(40)./Tv.^4;
n6_PV=x(41)+x(42)./Tv+x(43)./Tv.^2+x(44)./Tv.^3+x(45)./Tv.^4;
d1_PV=x(21)+x(22)./Tv+x(23)./Tv.^2+x(24)./Tv.^3+x(25)./Tv.^4;
d2_PV=x(26)+x(27)./Tv+x(28)./Tv.^2+x(29)./Tv.^3+x(30)./Tv.^4;
d3_PV=x(31)+x(32)./Tv+x(33)./Tv.^2+x(34)./Tv.^3+x(35)./Tv.^4;

alpha_l=(n1_PV.*rho_l+n2_PV.*rho_l.^2+n3_PV.*rho_l.^3+n4_PV.*rho_l.^4+n
5_PV.*rho_l.^5+n6_PV.*rho_l.^6)./(1+d1_PV.*rho_l+d2_PV.*rho_l.^2+d3_PV.
*rho_l.^3);
alpha_v=(n1_PV.*rho_v+n2_PV.*rho_v.^2+n3_PV.*rho_v.^3+n4_PV.*rho_v.^4+n
5_PV.*rho_v.^5+n6_PV.*rho_v.^6)./(1+d1_PV.*rho_v+d2_PV.*rho_v.^2+d3_PV.
*rho_v.^3);

q1=R.*Tv.*Tc.*((log(rho_l./rho_v))+alpha_l-alpha_v);
q2=((Pv.*Mw.*1000)./rhoc).*(1./rho_v-1./rho_l);
Q=q1-q2;

%Speed of Sound
%Nitrogen Ideal Helmholtz
tau=1./Tw;
a=[2.5, -12.76952708, -0.00784163, -1.934819*10^-4, -1.247742*10^-5,
6.678326*10^-8, 1.012941, 26.65788];
alpha_ideal_tau_2=-a(1).*tau.^(-2)+2.*a(4).*tau.^(-3)+6.*a(5).*tau.^(-
4)+12.*a(6).*tau.^(-5)-(a(7).*a(8).*exp(a(8).*tau))./(exp(a(8).*tau)-
1).^2;

%Nitrogen speed of sound
n1w=x(1)+x(2)./Tw+x(3)./Tw.^2+x(4)./Tw.^3+x(5)./Tw.^4;
n2w=x(6)+x(7)./Tw+x(8)./Tw.^2+x(9)./Tw.^3+x(10)./Tw.^4;
n3w=x(11)+x(12)./Tw+x(13)./Tw.^2+x(14)./Tw.^3+x(15)./Tw.^4;
```

```
n4w=x(16)+x(17)./Tw+x(18)./Tw.^2+x(19)./Tw.^3+x(20)./Tw.^4;
n5w=x(36)+x(37)./Tw+x(38)./Tw.^2+x(39)./Tw.^3+x(40)./Tw.^4;
n6w=x(41)+x(42)./Tw+x(43)./Tw.^2+x(44)./Tw.^3+x(45)./Tw.^4;
d1w=x(21)+x(22)./Tw+x(23)./Tw.^2+x(24)./Tw.^3+x(25)./Tw.^4;
d2w=x(26)+x(27)./Tw+x(28)./Tw.^2+x(29)./Tw.^3+x(30)./Tw.^4;
d3w=x(31)+x(32)./Tw+x(33)./Tw.^2+x(34)./Tw.^3+x(35)./Tw.^4;

fw=n1w.*deltaw+n2w.*deltaw.^2+n3w.*deltaw.^3+n4w.*deltaw.^4+n5w.*deltaw
.^5+n6w.*deltaw.^6;
gw=1+d1w.*deltaw+d2w.*deltaw.^2+d3w.*deltaw.^3;
f_deltaw=n1w+2.*n2w.*deltaw+3.*n3w.*deltaw.^2+4.*n4w.*deltaw.^3+5.*n5w.
*deltaw.^4+6.*n6w.*deltaw.^5;
g_deltaw=d1w+2.*d2w.*deltaw+3.*d3w.*deltaw.^2;
f_deltaw_2=2.*n2w+6.*n3w.*deltaw+12.*n4w.*deltaw.^2+20.*n5w.*deltaw.^3+
30.*n6w.*deltaw.^4;
g_deltaw_2=2.*d2w+6.*d3w.*deltaw;

alpha_deltaw=(f_deltaw.*gw-g_deltaw.*fw)./gw.^2;
alpha_deltaw_2=(f_deltaw_2.*gw-g_deltaw_2.*fw-
2.*gw.*g_deltaw.*alpha_deltaw)./gw.^2;
n1_tau=0;n2_tau=0;n3_tau=0;n4_tau=0;d1_tau=0;d2_tau=0;d3_tau=0;n5_tau=0
;n6_tau=0;
n1_tau2=0;n2_tau2=0;n3_tau2=0;n4_tau2=0;d1_tau2=0;d2_tau2=0;d3_tau2=0;n
5_tau2=0;n6_tau2=0;

for j=1:5
    n1_tau=n1_tau+(j-1).*x(j).*tau.^(j-2);
    n2_tau=n2_tau+(j-1).*x(5+j).*tau.^(j-2);
    n3_tau=n3_tau+(j-1).*x(10+j).*tau.^(j-2);
    n4_tau=n4_tau+(j-1).*x(15+j).*tau.^(j-2);
    d1_tau=d1_tau+(j-1).*x(20+j).*tau.^(j-2);
    d2_tau=d2_tau+(j-1).*x(25+j).*tau.^(j-2);
    d3_tau=d3_tau+(j-1).*x(30+j).*tau.^(j-2);
    n5_tau=n5_tau+(j-1).*x(35+j).*tau.^(j-2);
    n6_tau=n6_tau+(j-1).*x(40+j).*tau.^(j-2);

        n1_tau2=n1_tau2+(j-2).*(j-1).*x(j).*tau.^(j-3);
    n2_tau2=n2_tau2+(j-2).*(j-1).*x(5+j).*tau.^(j-3);
    n3_tau2=n3_tau2+(j-2).*(j-1).*x(10+j).*tau.^(j-3);
    n4_tau2=n4_tau2+(j-2).*(j-1).*x(15+j).*tau.^(j-3);
    d1_tau2=d1_tau2+(j-2).*(j-1).*x(20+j).*tau.^(j-3);
    d2_tau2=d2_tau2+(j-2).*(j-1).*x(25+j).*tau.^(j-3);
    d3_tau2=d3_tau2+(j-2).*(j-1).*x(30+j).*tau.^(j-3);
    n5_tau2=n5_tau2+(j-2).*(j-1).*x(35+j).*tau.^(j-3);
    n6_tau2=n6_tau2+(j-2).*(j-1).*x(40+j).*tau.^(j-3);
end
f_tauw=n1_tau.*deltaw+n2_tau.*deltaw.^2+n3_tau.*deltaw.^3+n4_tau.*delta
w.^4+n5_tau.*deltaw.^5+n6_tau.*deltaw.^6;
g_tauw=d1_tau.*deltaw+d2_tau.*deltaw.^2+d3_tau.*deltaw.^3;
f_tau_2w=n1_tau2.*deltaw+n2_tau2.*deltaw.^2+n3_tau2.*deltaw.^3+n4_tau2.
*deltaw.^4+n5_tau2.*deltaw.^5+n6_tau2.*deltaw.^6;
g_tau_2w=d1_tau2.*deltaw+d2_tau2.*deltaw.^2+d3_tau2.*deltaw.^3;
```

```
f_deltaw_tau=n1_tau+2.*n2_tau.*deltaw+3.*n3_tau.*deltaw.^2+4.*n4_tau.*d
eltaw.^3+5.*n5_tau.*deltaw.^4+6.*n6_tau.*deltaw.^5;
g_deltaw_tau=d1_tau+2.*d2_tau.*deltaw+3.*d3_tau.*deltaw.^2;

alpha_tauw=(f_tauw.*gw-g_tauw.*fw)./gw.^2;
alpha_tau_2w=(f_tau_2w.*gw-g_tau_2w.*fw-
2.*gw.*g_tauw.*alpha_tauw)./gw.^2;
alpha_deltaw_tau=(f_deltaw_tau.*gw.^2+gw.*g_tauw.*f_deltaw-
g_deltaw_tau.*gw.*fw-f_tauw.*gw.*g_deltaw-2.*g_tauw.*(f_deltaw.*gw-
g_deltaw.*fw))./(gw.^3);

w2MoverRT=1+2.*deltaw.*alpha_deltaw+alpha_deltaw_2.*deltaw.^2-
(1+deltaw.*alpha_deltaw-
deltaw.*tau.*alpha_deltaw_tau).^2./(tau.^2.*(alpha_ideal_tau_2+alpha_ta
u_2w));
SDcalc=((w2MoverRT).*(R.*(1./tau).*Tc.*1000)./(Mw)).^0.5;

%Nitrogen CV
%Nitrogen Ideal Helmholtz
tauCV=1./TCv;
a=[2.5, -12.76952708, -0.00784163, -1.934819*10^-4, -1.247742*10^-5,
6.678326*10^-8, 1.012941, 26.65788];
alpha_ideal_tau_2Cv=-a(1).*tauCV.^(-2)+2.*a(4).*tauCV.^(-
3)+6.*a(5).*tauCV.^(-4)+12.*a(6).*tauCV.^(-5)-
(a(7).*a(8).*exp(a(8).*tauCV))./(exp(a(8).*tauCV)-1).^2;

n1Cv=x(1)+x(2)./TCv+x(3)./TCv.^2+x(4)./TCv.^3+x(5)./TCv.^4;
n2Cv=x(6)+x(7)./TCv+x(8)./TCv.^2+x(9)./TCv.^3+x(10)./TCv.^4;
n3Cv=x(11)+x(12)./TCv+x(13)./TCv.^2+x(14)./TCv.^3+x(15)./TCv.^4;
n4Cv=x(16)+x(17)./TCv+x(18)./TCv.^2+x(19)./TCv.^3+x(20)./TCv.^4;
n5Cv=x(36)+x(37)./TCv+x(38)./TCv.^2+x(39)./TCv.^3+x(40)./TCv.^4;
n6Cv=x(41)+x(42)./TCv+x(43)./TCv.^2+x(44)./TCv.^3+x(45)./TCv.^4;
d1Cv=x(21)+x(22)./TCv+x(23)./TCv.^2+x(24)./TCv.^3+x(25)./TCv.^4;
d2Cv=x(26)+x(27)./TCv+x(28)./TCv.^2+x(29)./TCv.^3+x(30)./TCv.^4;
d3Cv=x(31)+x(32)./TCv+x(33)./TCv.^2+x(34)./TCv.^3+x(35)./TCv.^4;

fCv=n1Cv.*deltaCv+n2Cv.*deltaCv.^2+n3Cv.*deltaCv.^3+n4Cv.*deltaCv.^4+n5
Cv.*deltaCv.^5+n6Cv.*deltaCv.^6;
gCv=1+d1Cv.*deltaCv+d2Cv.*deltaCv.^2+d3Cv.*deltaCv.^3;

n1_tauCV=0;n2_tauCV=0;n3_tauCV=0;n4_tauCV=0;d1_tauCV=0;d2_tauCV=0;d3_ta
uCV=0;n5_tauCV=0;n6_tauCV=0;
n1_tauCV2=0;n2_tauCV2=0;n3_tauCV2=0;n4_tauCV2=0;d1_tauCV2=0;d2_tauCV2=0
;d3_tauCV2=0;n5_tauCV2=0;n6_tauCV2=0;
for j=1:5
    n1_tauCV=n1_tauCV+(j-1).*x(j).*tauCV.^(j-2);
    n2_tauCV=n2_tauCV+(j-1).*x(5+j).*tauCV.^(j-2);
    n3_tauCV=n3_tauCV+(j-1).*x(10+j).*tauCV.^(j-2);
    n4_tauCV=n4_tauCV+(j-1).*x(15+j).*tauCV.^(j-2);
    d1_tauCV=d1_tauCV+(j-1).*x(20+j).*tauCV.^(j-2);
    d2_tauCV=d2_tauCV+(j-1).*x(25+j).*tauCV.^(j-2);
    d3_tauCV=d3_tauCV+(j-1).*x(30+j).*tauCV.^(j-2);
```

```
    n5_tauCV=n5_tauCV+(j-1).*x(35+j).*tauCV.^(j-2);
    n6_tauCV=n6_tauCV+(j-1).*x(40+j).*tauCV.^(j-2);

    n1_tauCV2=n1_tauCV2+(j-2).*(j-1).*x(j).*tauCV.^(j-3);
    n2_tauCV2=n2_tauCV2+(j-2).*(j-1).*x(5+j).*tauCV.^(j-3);
    n3_tauCV2=n3_tauCV2+(j-2).*(j-1).*x(10+j).*tauCV.^(j-3);
    n4_tauCV2=n4_tauCV2+(j-2).*(j-1).*x(15+j).*tauCV.^(j-3);
    d1_tauCV2=d1_tauCV2+(j-2).*(j-1).*x(20+j).*tauCV.^(j-3);
    d2_tauCV2=d2_tauCV2+(j-2).*(j-1).*x(25+j).*tauCV.^(j-3);
    d3_tauCV2=d3_tauCV2+(j-2).*(j-1).*x(30+j).*tauCV.^(j-3);
    n5_tauCV2=n5_tauCV2+(j-2).*(j-1).*x(35+j).*tauCV.^(j-3);
    n6_tauCV2=n6_tauCV2+(j-2).*(j-1).*x(40+j).*tauCV.^(j-3);
end
f_tauCv=n1_tauCV.*deltaCv+n2_tauCV.*deltaCv.^2+n3_tauCV.*deltaCv.^3+n4_
tauCV.*deltaCv.^4+n5_tauCV.*deltaCv.^5+n6_tauCV.*deltaCv.^6;
g_tauCv=d1_tauCV.*deltaCv+d2_tauCV.*deltaCv.^2+d3_tauCV.*deltaCv.^3;
f_tau_2Cv=n1_tauCV2.*deltaCv+n2_tauCV2.*deltaCv.^2+n3_tauCV2.*deltaCv.^
3+n4_tauCV2.*deltaCv.^4+n5_tauCV2.*deltaCv.^5+n6_tauCV2.*deltaCv.^6;
g_tau_2Cv=d1_tauCV2.*deltaCv+d2_tauCV2.*deltaCv.^2+d3_tauCV2.*deltaCv.^
3;

alpha_tauCv=(f_tauCv.*gCv-g_tauCv.*fCv)./gCv.^2;
alpha_tau_2Cv=(f_tau_2Cv.*gCv-g_tau_2Cv.*fCv-
2.*gCv.*g_tauCv.*alpha_tauCv)./gCv.^2;
CVcalc=R.*(-tauCV.^2.*(alpha_ideal_tau_2Cv+alpha_tau_2Cv));

f = [ww.*1;zeros(43,1);0;0;0;SD.*0.5;CV.*1]-
[ww.*((1+delta.*(alpha_delta))./Zg);Q;2000.*con1;2000.*con2;2000.*con3;
SDcalc.*0.5;CVcalc.*1];
```

APPENDIX E

Appendix E shows a program code based upon C++ language. This program performs pressure calculations using rational equation of state functional and modern functional as in GERG-2008. The code calculates pressure values and computational time require for a single evaluation.

```
#include <vector>
#include <iostream>
#include <time.h>

//#include "crossplatform_shared_ptr.h"
//#include "AbstractState.h"

/* */

#include <vector>

std::vector<int> d = { 1, 1, 2, 2, 3, 3, 1, 1, 1, 3, 3, 4, 6, 6, 7, 7, 8, 8, 1, 2,
3, 4, 5, 8, 4, 5, 5, 8, 3, 5, 6, 9 };
std::vector<int> l = { 0, 0, 0, 0, 0, 0, 1, 1, 1, 1, 1, 1, 1, 1, 1, 1, 1, 1, 2, 2,
2, 2, 2, 2, 3, 3, 3, 3, 4, 4, 4, 4 };
std::vector<double> n = { 0.924803575275, -0.492448489428, 0.661883336938, -
1.92902649201, -0.0622469309629, 0.349943957581, 0.564857472498, -1.61720005987, -
0.481395031883, 0.421150636384, -0.0161962230825, 0.172100994165,
0.00735448924933, 0.0168077305479, -0.00107626664179, -0.0137318088513,
0.000635466899859, 0.00304432279419, -0.0435762336045, -0.0723174889316,
0.0389644315272, -0.021220136391, 0.00408822981509, -5.51990017984e-05, -
0.0462016716479, -0.00300311716011, 0.0368825891208, -0.0025585684622,
0.00896915264558, -0.0044151337035, 0.00133722924858, 0.000264832491957 };
std::vector<double> t = { 0.25, 0.875, 0.5, 0.875, 0.375, 0.75, 0.5, 0.75, 2,
1.25, 3.5, 1, 0.5, 3, 0, 2.75, 0.75, 2.5, 4, 6, 6, 3, 3, 6, 16, 11, 15, 12, 12, 7,
4, 16 };

std::vector<double> n_Gaussian = { 19.6688194015, -20.911560073, 0.0167788306989,
2627.67566274 };
std::vector<int> d_Gaussian = { 1, 1, 3, 2 };
std::vector<int> t_Gaussian = { 0, 1, 2, 3 };
std::vector<int> beta = { 325, 325, 300, 275 };
std::vector<int> epsilon = { 1, 1, 1, 1 };
std::vector<int> eta = { 20, 20, 15, 25 };
std::vector<double> gamma = { 1.16, 1.16, 1.13, 1.25 };

double dalphar_dDelta_conventional(const double tau, const double delta) {
	double summer = 0;
	double log_tau = log(tau), log_delta = log(delta);
	for (unsigned int k = 0; k < 6; ++k)
	{
```

```
                // pow(delta, d[k]-1)*pow(tau, t[k]) --> exp((d[k]-1)*log(delta)+
t[k]*log(tau))
                summer += d[k] * n[k] * exp((d[k] - 1)*log_delta + t[k] * log_tau);
        }
        for (unsigned int k = 6; k < 32; ++k)
        {
                double pow_delta_lk = pow(delta, l[k]);
                summer += n[k] * exp((d[k] - 1)*log_delta + t[k] * log_tau -
pow(delta, l[k]))*(d[k] - l[k] * pow_delta_lk);
        }
        for (unsigned int k = 0; k < 4; ++k)
        {
                summer += n_Gaussian[k] * pow(delta, d_Gaussian[k] - 1)*pow(tau,
t_Gaussian[k])*exp(-eta[k] * pow(delta - epsilon[k], 2) - beta[k] * pow(tau -
gamma[k], 2))*(d_Gaussian[k] - 2 * eta[k] * delta*(delta - epsilon[k]));
        }
        return summer;
}

std::vector<double> B = { 0.46131520309233526, -0.8720874696304605, -
0.920438417237658, 0.2973194609937205, -0.10935746132151714, -0.12459493381236057,
1.2875265205314776, -3.120101916214109, 2.879215543759785, 0.560846632170082,
0.08540697853924611, -0.4898861796429146, 0.6419703709564887, 0.6200371073971928,
-1.746823346140164, -0.006336150975677217, 0.14151403078990435, -
0.17779302774202227, -0.3501322270166177, 0.6132288387336707, -0.2665713537796835,
0.9923596936025292, -1.631851496234707, -0.29782839017993784, 0.08081848309792541,
0.09900729795177489, -0.3135689594673375, 0.06667284671791185, 0.8115649125754364,
-0.07630349735827587, 0.0036391861409774203, 0.05495468857874896, -
0.05400767480943274, -0.10320932846842755, 0.01373444375655594, -
0.004032870953117091, -0.07952646832002297, 0.24378025235460282, -
0.18758212744270497,0, 0.005566714251489701, 0.005049850045833784 5, -
0.034054725403794894, 0.0267280731224514,0 };

double HornerEvaluate(double x, const double * CoefficientsOfPolynomial, unsigned
int DegreeOfPolynomial)
{
        /*
        We want to evaluate the polynomial in x, of coefficients
CoefficientsOfPolynomial, using Horner's method.
        The result is stored in dbResult.
        */
        double dbResult = 0.;
        int i;
        for (i = DegreeOfPolynomial; i >= 0; i--)
        {
                dbResult = dbResult * x + CoefficientsOfPolynomial[i];
        }
        return dbResult;
}

double calc_Horner(double tau, unsigned int offset, unsigned int n1, unsigned int
nN) {
        return HornerEvaluate(tau, &(B[0]) + offset, nN);
}
```

```
double calc_pow(double tau, unsigned int offset, unsigned int n1, unsigned int nN)
{
	int i = 0;
	double summer = 0;
	for (unsigned int j = n1; j <= nN; ++j) {
		summer += B[offset + i] * pow(tau, static_cast<int>(j));
		++i;
	}
	return summer;
}

double calc(double tau, unsigned int offset, unsigned int n1, unsigned int nN)
{
	return calc_Horner(tau, offset, n1, nN);
}

double n1(double tau) { return calc(tau, 0, 0, 4); }
double n2(double tau) { return calc(tau, 5, 0, 4); }
double n3(double tau) { return calc(tau, 10, 0, 4); }
double n4(double tau) { return calc(tau, 15, 0, 4); }
double d1(double tau) { return calc(tau, 20, 0, 4); }
double d2(double tau) { return calc(tau, 25, 0, 4); }
double d3(double tau) { return calc(tau, 30, 0, 4); }
double n5(double tau) { return calc(tau, 35, 0, 4); }
double n6(double tau) { return calc(tau, 40, 0, 4); }

double dalphar_dDelta(const double tau, const double delta)
{
	double _n1 = n1(tau), _n2 = n2(tau), _n3 = n3(tau), _n4 = n4(tau), _n5 =
n5(tau), _n6 = n6(tau);
	double _d1 = d1(tau), _d2 = d2(tau), _d3 = d3(tau);

	double num = delta*(_n1 + delta*(_n2 + delta*(_n3 + delta*(_n4 + delta*(_n5
+ delta*_n6)))));
	double den = 1 + delta*(_d1 + delta*(_d2 + delta*_d3));

	double dnum_ddelta = _n1 + delta*(2 * _n2 + delta*(3 * _n3 + delta*(4 * _n4
+ delta*(5 * _n5 + 6 * _n6*delta))));
	double dden_ddelta = _d1 + delta*(2 * _d2 + 3 * _d3*delta);

	double dalphar_dDelta = (den*dnum_ddelta - num*dden_ddelta) / (den*den);

	return dalphar_dDelta;
}

double p_conventional(double tau, double delta)
{
	double R = 8.3144621, T = 126.192 / tau, rhomolar = delta*11183.9014646;
	double p_old = rhomolar*R*T*(1 + delta*dalphar_dDelta_conventional(tau,
delta));
	return p_old;
}
```

```
double p(double tau, double delta)
{
	double R = 8.3144621, T = 126.192 / tau, rhomolar = delta*11183.9014646;
	double p_new = rhomolar*R*T*(1 + delta*dalphar_dDelta(tau, delta));
	return p_new;
}

int main()
{
	double T = 300, rhomolar = 11183, tau = 126.192 / T, delta = rhomolar /
11183.9014646;
	long N = 1000000;

	{
		double t1 = clock();
		double summer = 0;
		for (unsigned int ii = N; ii > 0; --ii) {
			summer += p(tau, delta);
		}
		double t2 = clock();
		std::cout << summer / ((double)N) << " " << (t2 - t1) /
((double)CLOCKS_PER_SEC) / ((double)N)*1e6 << std::endl;
	}
	{
		double t1 = clock();
		double summer = 0;
		for (unsigned int ii = N; ii > 0; --ii) {
			summer += p_conventional(tau, delta);
		}
		double t2 = clock();
		std::cout << summer / ((double)N) << " " << (t2 - t1) /
((double)CLOCKS_PER_SEC) / ((double)N)*1e6 << std::endl;
	}
	int rr = 0;
}
```